



## AN ABSTRACT OF THE DISSERTATION OF

Morgan Brown for the degree of Doctor of Philosophy in Material Science  
presented on September 18, 2017.

Title: Graphene Biotransistors, an Exploration of Neurosensing and Biofilm-sensing Applications

Abstract approved: \_\_\_\_\_

Ethan D. Minot

Atomically-thin graphene sheets have unprecedented characteristics for biosensing applications. These characteristics include mechanical flexibility and strength, optical transparency, electrical sensitivity and biocompatibility. The primary theme of this dissertation is the characterization and application of graphene field-effect transistors (FETs) in biologically-relevant physiological environments.

Understanding the interface that forms between an electrolyte and graphene is critical to understanding biosensing mechanisms. The electronic signals measured by a graphene FET biosensor are typically the result of changes in the layer of dissolved ions near the graphene surface. The coupling between dissolved ions and a conductive surface is described by the electric double layer capacitance,  $C_{EDL}$ . This interfacial capacitance has been studied for many years using conductive liquids and bulk metal surfaces. Only recently have careful studies of  $C_{EDL}$  focused on the interface between graphene and conductive liquids. We use Hall effect measurements to determine the total capacitance at the interface and the tight-binding-model-based theory to separate the quantum capacitance,  $C_Q$ , and  $C_{EDL}$ . Based on this investigation, we find a  $C_{EDL}$  of  $\sim 0.04 \text{ F/m}^2$  for biologically relevant

fluids and  $\sim 0.11$  F/m<sup>2</sup> for ionic liquids. Both of these values are lower than the typical value of 0.2 F/m<sup>2</sup> found with metals. This finding is also significant for choosing ideal fluids for graphene-based super capacitors.

We have systematically characterized the noise and sensitivity of graphene FETs in aqueous electrolyte environments. We established the minimum attainable noise in this environment by determining the thermal noise limit. We then investigated charge carrier mobility, which is critical to device sensitivity. We performed Hall bar measurements on electrolyte-gated graphene assuming a Drude model, and find that the room temperature carrier mobility in water-gated, SiO<sub>2</sub>-supported graphene reaches 7000 cm<sup>2</sup>/Vs. This value is comparable to the best dry SiO<sub>2</sub>-supported graphene devices. Our results show that the electrical performance of graphene is robust, even in the presence of dissolved ions that introduce an additional mechanism for Coulomb scattering.

We established two novel applications of graphene field-effect transistor biosensor. The first application is in-situ monitoring of the pH inside a living biofilm with fast temporal resolution ( $\sim 1$  s) over multi-hour time periods. The atomically thin sensor is positioned between the biofilm and a supporting silicon oxide surface, providing noninvasive access to conditions at the base of the biofilm. We determine the transient changes in pH when the biofilm metabolizes substrate molecules and when it is exposed to biocide. The pH resolution is approximately 0.01 pH units when using 1 s time averaging; the sensor drift is approximately 0.01 pH units per hour. Our results demonstrate the potential of this technology to further the study of biofilm metabolism and improve monitoring of biofilm health.

The second application for GFET biosensors that we established is wearable sensor patches for single cells. Recent advances in the fields of optics, biochemistry, and nanotechnology have instigated a multidisciplinary effort to understand the neural circuitry of the human brain. The electrodes currently used for *in vivo* single neuron sensing have not significantly advanced over the past century. The industry standard remains simple, insulated, conductive shafts with

small, exposed tips. Graphene-based field-effect transistors are flexible yet strong, biocompatible, and able to locally amplify the electrogenic signals produced by neurons. This combination of material characteristics makes graphene ideal for next-generation biosensing applications.

The graphene in our experiments is etched into patterns inspired by the Japanese paper art of kirigami to enable in-plane stretching. The devices are then stretched over cells, isolating the graphene from possible substrate noise while forming a conformal coating over the cell to obtain the optimal signal-to-noise ratio. The flexibility of these devices makes them promising as “wearable” electronics for cells with applications for both *in vivo* and brain-slice electrophysiological experiments. We present characterization and initial single cell measurements from these devices.

©Copyright by Morgan Brown  
September 18, 2017  
All Rights Reserved

Graphene Biotransistors, an Exploration of Neurosensing and Biofilm-sensing  
Applications  
by  
Morgan Brown

A DISSERTATION

submitted to

Oregon State University

in partial fulfillment of  
the requirements for the  
degree of

Doctor of Philosophy

Presented September 18, 2017  
Commencement June 2018

Doctor of Philosophy dissertation of Morgan Brown presented on September 18, 2017

APPROVED:

---

Major Professor, representing Material Science

---

Head of the School of Mechanical, Industrial, and Manufacturing Engineering

---

Dean of the Graduate School

I understand that my dissertation will become part of the permanent collection of Oregon State University libraries. My signature below authorizes release of my dissertation to any reader upon request.

---

Morgan Brown, Author

## ACKNOWLEDGEMENTS

First and foremost I want to thank my wife, Sarah for her confidence and encouragement which both instigated and sustained this journey. This has been a group project, and I also want to thank my parents and my boys for their love and the passion they showed for each of the little discoveries presented in this document.

I would like to thank my advisor Ethan his guidance, and for introducing me to the fascinating world of biosensing. I am continually impressed by his ability to get to the fundamentals of a complex problem and find a practical path forward.

Much of the work in this thesis is a result of work performed with Michael Crosser, whom I would like to thank for both mentorship and camaraderie.

I would like to thank the other professors and students who form the tight knit group that is the OSU material science department. Brady Gibbons for always having sound advice when I needed it. David Cann, Julie Tucker, Bill Warrens, and Brian Bay for numerous discussions about teaching philosophy. The other students in Materials Science, who went through this with me, Austin and Jose specifically, for sharing this adventure with me.

My teaching experience was strongly influenced by KC Walsh. Thank you for the teaching practicum you kindly put together for me and sharing your vison of a modern flipped classroom.

I have a respect for biofilms, their communication, and their role in the ecosystem as a result of my work with Lewis Semprini. Thank you for the introduction to this fascinating world.

I would like to thank Patrick Chappell for all his help and education regarding the culturing and triggering of neurons. I appreciated the opportunity to attend the NW Neuroscience conference with your group and hope to see you there again in the future.

I would like to thank Matt Graham for the many insightful discussions. I also appreciate the use of your lab space and the inverted microscope we adopted.

While they often don't get the credit due them, much of the research performed at this university would come to a grinding halt without the work performed by Chris and Rick both in the clean

room and in labs across campus. Thank you for helping address fabrication issue and coming to our aid when our E-Beam exploded.

I would also like to thank my lab mates in the Minot group, Lee, Dan, Mitch and especially Tal for the training and inspiration into the world of biosensing and the game of darts.

Last but not least I want to thank our collaborators at Cornell; Paul McEuen for his guidance and support of this project over the years. Mike and Kathryn for the marathon trips to Cornell and all the science and literature discussions over the years.

## CONTRIBUTION OF AUTHORS

Michael Crosser contributed to the fabrication and Hall based measurements in Chapters 2-3. The graphene for devices in Chapter 3 was provided by Matthew Leyden. The biofilms discussed in Chapter 4 were provided by Lewis Semprini and cultured by Leila Barker. The neurons investigated in Chapter 5 were provided by Pat Chappell. Amani Alobaidi contributed to the culturing and confocal imaging of these cells in the lab of Bo Sun. Michael Reynolds, Kathryn McGill and Samantha Norris contributed to the device and graphene based measurements and images presented in Chapter 5. The cardiomyocytes investigated in Chapter 5 were cultured in the lab of Jan Lammerding by Patricia Davidson and Tyler Kirby. Ethan Minot provided insight, guidance and motivation for all aspects of the work presented in this dissertation.

## TABLE OF CONTENTS

|  | <u>Page</u> |
|--|-------------|
| CHAPTER 1 .....  | 1           |
| Introduction.....  | 1           |
| 1.1 Life and Low-Dimensional Materials .....               | 2           |
| 1.2 Graphene for biosensing applications .....             | 2           |
| 1.3 Structure to Properties .....                          | 2           |
| 1.4 Liquid gating .....                                    | 5           |
| 1.4.1 EDL theory and the Debye screening length.....       | 7           |
| 1.5 Electric Double Layer Capacitors .....                 | 8           |
| 1.6 Device performance; Sensitivity and Noise Limit .....  | 10          |
| 1.7 Effect of substrate on device performance.....         | 12          |
| 1.8 What do we actually sense from cells? .....            | 13          |
| 1.9 Graduate work not included in this thesis .....        | 15          |
| CHAPTER 2 .....  | 19          |
| 2.1 Introduction .....                                     | 20          |
| 2.2 Previous work on single-layer graphene capacitors..... | 22          |
| 2.3 Quantum capacitance .....                              | 23          |
| 2.4 Experimental Methods .....                             | 25          |
| 2.5 Results and discussion.....                            | 28          |
| 2.6 Conclusion.....  | 30          |
| References .....   | 32          |

## TABLE OF CONTENTS (Continued)

|   |    |
|---|----|
| CHAPTER 3 .....   | 34 |
| 3.1 Introduction .....  | 35 |
| 3.2 Methods.....  | 36 |
| 3.3 Results and Discussion.....   | 39 |
| 3.4 Conclusion.....   | 44 |
| 3.5 Supporting Information .....  | 45 |
| 3.6 Bibliography:.....  | 50 |
| CHAPTER 4 .....   | 52 |
| 4.1 Introduction .....  | 53 |
| 4.2 Methods.....  | 54 |
| 4.3 Results and Discussion.....   | 59 |
| 4.4 Conclusion.....   | 63 |
| 4.4 References .....  | 65 |
| 4.5 Supporting Information .....  | 67 |
| CHAPTER 5 .....   | 70 |
| 5.1 Introduction .....  | 71 |
| 5.2 Methods.....  | 72 |
| 5.2.1 Fabrication.....  | 72 |
| 5.2.2 Testing.....  | 73 |
| 5.2.3 Cell culturing and confocal Ca <sup>++</sup> activity verification..... | 74 |
| 5.3 Results and discussion.....   | 76 |
| 5.3.1 Graphene Cell interface.....  | 76 |
| 5.3.2 Time- and voltage-resolution of the sensor.....                         | 79 |

## TABLE OF CONTENTS (Continued)

|  |    |
|--|----|
| 5.3.3 Noise resolution of the sensor .....   | 80 |
| 2.3.4 Experiments with neurons .....   | 81 |
| 5.3.5 Mechanical device designs, preliminary exploration to optimize graphene neuron interface ..... | 85 |
| 5.4 Conclusion.....  | 86 |
| 5.5 Bibliography.....  | 88 |
| Concluding discussion .....  | 90 |
| CURRICULUM VITAE .....   | 93 |
| BIBLIOGRAPHY .....   | 96 |

## LIST OF FIGURES

| <u>Figures</u>   | <u>Page</u> |
|--|-------------|
| Figure 1.1 Gem-based unit cell to graphene progression.....          | 3           |
| Figure 1.2 Graphene DFT analysis.....                                | 5           |
| Figure 1.3 Fluid gated graphene device response.....                 | 6           |
| Figure 1.4 Electronic Double Layer.....                              | 8           |
| Figure 1.5 Comparison of Capacitance techniques .....                | 9           |
| Figure 1.6 Plot of gate voltage noise power spectral density.....    | 11          |
| Figure 1.7 Graphene FET device response.....                         | 14          |
| Figure 2.1 Graphene E vs k diagram.....                              | 24          |
| Figure 2.2 Hall bar device geometry.....                             | 25          |
| Figure 2.3 V <sub>xx</sub> and V <sub>h</sub> response.....          | 28          |
| Figure 2.4 Carrier density Hall data.....                            | 29          |
| Figure 2.5 Capacitance vs surface carrier density.....               | 31          |
| Figure 3.1 Hall bar geometry.....                                    | 39          |
| Figure 3.2 V <sub>h</sub> and n <sub>s</sub> device curves.....      | 41          |
| Figure 3.3 Sheet conductivity and mobility.....                      | 44          |
| Figure 4.1 Optical micrograph and cartoon of biofilm growth.....     | 57          |
| Figure 4.2 I-V <sub>g</sub> curves at various pH values.....         | 58          |
| Figure 4.3 Changing pH inside biofilm.....                           | 62          |
| Figure 4.4 Response to NH <sub>2</sub> OH.....                       | 64          |
| Figure 5.1 Graphene on and off substrate.....                        | 73          |
| Figure 5.2 Fabrication of releasable devices.....                    | 75          |
| Figure 5.3 Image of device released from the surface in fluid.....   | 76          |
| Figure 5.4 Confocal microscopy of neurons.....                       | 77          |
| Figure 5.5 Typical healthy cardiomyocyte cell.....                   | 78          |
| Figure 5.6 Stretching of a graphene device over a cardiomyocyte..... | 79          |

## LIST OF FIGURES (Continued)

| <u>Figures</u>   | <u>Page</u> |
|--|-------------|
| Figure 5.7 Cleft model.....  | 80          |
| Figure 5.8 Stimulating a cell firing event.....                          | 81          |
| Figure 5.9 Noise spectrum of a graphene FET.....                         | 82          |
| Figure 5.10 FET response and spiking.....                                | 83          |
| Figure 5.11 Optical and electrical data, neurons and cardiomyocytes..... | 84          |
| Figure 5.12 Spike data from graphene over a neuron.....                  | 85          |
| Figure 5.13 Comparing spike response of cells below and above cells..... | 86          |
| Figure 5.14 Cell and metal microelectrode.....                           | 87          |
| Figure 5.15 Kirigami device over cell.....                               | 88          |

Graphene Biotransistors, an Exploration of Neurosensing and Biofilm-sensing Applications

## CHAPTER 1

### Introduction

### ***1.1 Life and Low-Dimensional Materials***

Recent breakthroughs in diverse fields from neuroscience to microbiology have been enabled by the novel design and application of low-dimensional electronic materials. These materials provide a toolset to observe and interact with biological processes utilizing the novel properties that emerge from commonplace materials when reduced to the nanometer scale. These materials have recently been applied to answer fundamental questions about the nature of bacteria ranging from the existence of communication between bacteria,<sup>1,2</sup> to aging and attachment.<sup>3</sup>

In neuroscience a primary goal of the 21<sup>st</sup> century is to develop tools which enable study of the brain not as a series of small isolated areas, but in terms of the emergent properties based on communication between these areas. To achieve this goal requires recording from significantly more neurons via targeted high resolution measurements for significantly longer time periods than is currently viable. The first steps to address all these challenges have been taken using low dimensional materials. Higher density arrays of electrodes have recently been fabricated as injectable neural nets.<sup>4</sup> Measurements of individual neurons have been made using nanopillars and electroporation<sup>5</sup> to take internal measurements similar to those historically made with a patch clamp but which allow the cell to heal. Longer term *in vivo* measurements have been made and axon growth has been observed because of biocompatibility.<sup>6,7</sup>

### ***1.2 Graphene for biosensing applications***

Compared to traditional biosensing devices, atomically-thin graphene sheets have unprecedented characteristics, including flexibility, strength, optical transparency, and biocompatibility.<sup>8</sup> Additionally, the semiconductor properties of graphene allow signal amplification at the recording site, resulting in ‘active electrodes’ that further support the signal robustness and multiplexing required for future increases in channel count. The primary theme of this dissertation is the characterization and application of graphene field-effect transistors (FETs) in biologically-relevant physiological environments.

### ***1.3 Structure to Properties***

Graphene is a two-dimensional solid that was brought to the forefront of science in 2004 by two professors in England playing with scotch tape and graphite.<sup>8</sup> Graphite is commonly used as a lubricant because the weak bonds between the layers allow these layers of graphene to easily slide over each other. It is also the weak bonding between layers that allowed the simple process

of scotch tape exfoliation to progress down to a single layer of carbon atoms, or graphene. This carbon allotrope has a hexagonal structure of  $1.42 \text{ \AA}$  sigma bonds, formed from the  $\text{sp}^2$  hybridization of carbon atom orbitals at  $120^\circ$ . In this bonding structure, the three sigma bonds are responsible for the majority of the binding energy, and the remarkable mechanical strength of  $30 \text{ N/m}^9$ . This leaves the final of carbon's four valence electrons in the  $\text{p}_z$  orbitals free to form conduction and valance bands in pi-bonding and anti-bonding states. It is the electrons in the  $\text{p}_z$  orbital that give rise to the notable electrical characteristics of graphene.

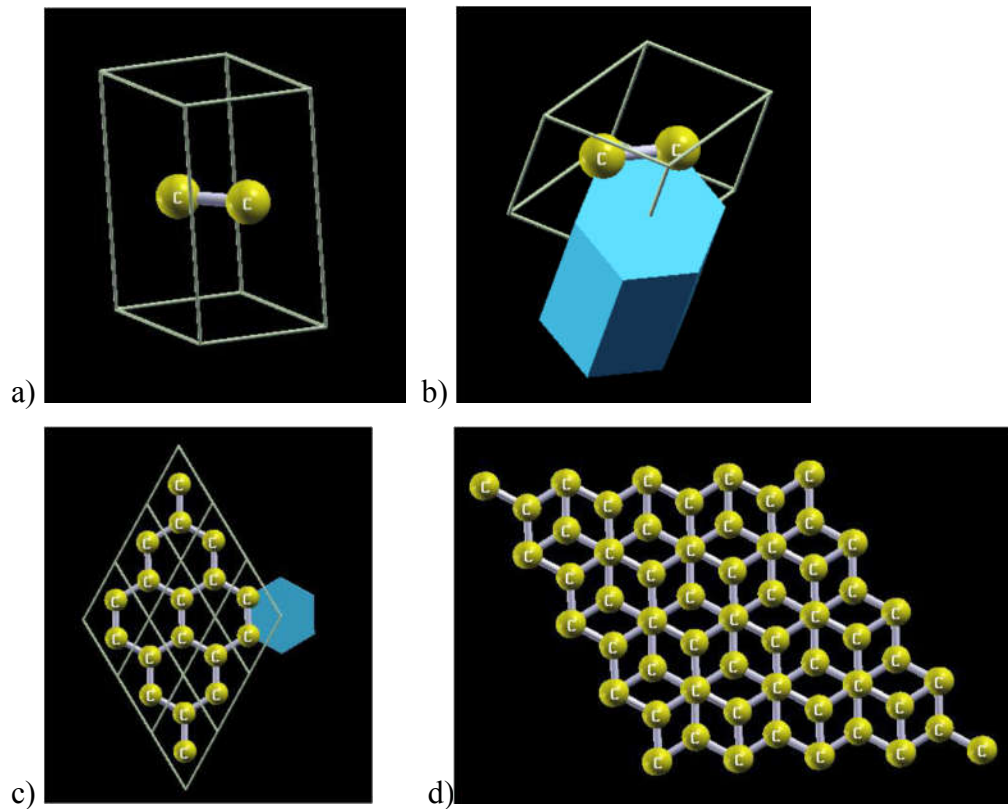


**Figure 1** Gem-based unit cell to Graphene progression showing (a) the basic unit cell and (b) the addition of the WS Cell. These structures can then be combined into the traditional hexagonal structure, (c) as shown with the WSC. Finally, (d) shows ABA-stacked graphite.

The basic graphene unit cell consists of only two carbon atoms, as shown in Figure 1a. The more familiar hexagonal Wigner-Seitz cell is shown in blue, superimposed on the unit cell. The hexagon crystal structure is evident once three cells are placed together, as shown in Figure 1b and c, respectively. This single sheet of graphene has the space group  $\text{P}6/\text{mmm}$ . In the case of few-layer

graphene, an elemental ABA stacking is common, as shown in Fig. 2d. Few-layer graphene has an inter-layer separation of  $\sim 3.35 \text{ \AA}$ , and multi-layer graphene is a P6<sub>3</sub>/mmc space group material.<sup>10,11</sup>

The unique structure of single-layer graphene generates extraordinary properties such as high charge carrier mobility, which is critical for the high sensitivity needed in bio-sensing applications. Charge carrier motilities of 200,000 cm<sup>2</sup>/Vs and a mean free path of  $\sim 1.2 \mu\text{m}$  have been determined at carrier concentrations of 10<sup>11</sup> cm<sup>-2</sup> for graphene devices at high vacuum and low temperature.<sup>12</sup> This mobility value is two orders of magnitude higher than Si, indicating the potential for unprecedented sensitivity in graphene devices. Much of the research published today focuses on this extraordinary characteristic and the search for methods to attain it in ambient conditions.

Theory predicts that free electrons present in graphene will behave as massless Dirac fermions that all travel at the Fermi velocity; a phenomenon partly responsible for the high carrier mobility that is thought to be unique to single-layer graphene. The results of density functional theory (DFT) calculations show a series of cones at the K points of the Brillouin zone. The upper and lower cones correspond to the valence and conduction bands, respectively. The point at which they meet in the middle is called the Dirac point. The Fermi energy lies in this middle point for un-doped materials. As there is no appreciable gap between these cones, graphene is considered a zero-band-gap material. As shown in Fig. 2d, the slope near the Dirac point is linear for single layer, and gains curvature with increasing layers. If analyzed using traditional band theory this would indicate that the carriers had infinite mass ( $m_{\text{effective}} = \frac{d^2 E}{dk^2}$ ). However, a correct description considers the charge carriers in terms of a quantum-relativistic Schrodinger wave equation, resulting in a dispersion relation,  $E = \hbar v_f k$ , and predicting that the charge carriers have zero effective mass and a remarkably high velocity,  $v_f = 10^6 \text{ ms}^{-1}$ . This contributes to the high mobility, and is so far unique among solids.<sup>13</sup> It is worth noting that in most applications the mobility is limited by scattering events.<sup>14</sup> In chapter 3 we address concerns that the ions in the electrolyte used for gating will significantly lower mobility.

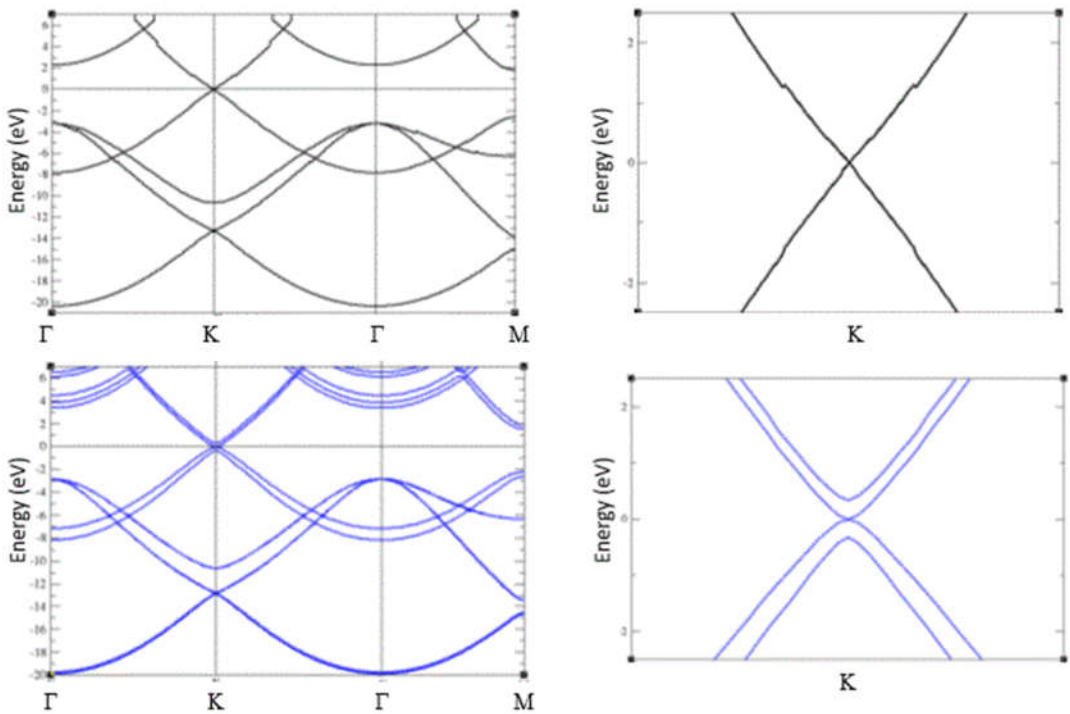


**Figure 2.** This structure was implemented in Gem, and electron densities were examined via the Flair density functional theory (DFT) program.<sup>15</sup> Flair uses a Full-Potential Linearized Augmented Plane Wave (FLAPW) method for its calculations. Differing from simple tight binding models that examine only the Pz orbitals, the FLAPW method also accounts for lower-energy sp<sub>2</sub> hybridization aspects.

#### 1.4 Liquid gating

Graphene field-effect transistors (FET) are similar to other FET devices. An applied gate voltage,  $V_g$ , induces a change in charge carrier density, thereby altering the electrical resistance of the material. Figure 3b shows the source drain current,  $I_{sd}$ , vs applied gate voltage,  $V_g$ , response for a typical graphene FET. Metal oxide gates can be used for this. However, significantly higher capacitive coupling values can be achieved using an electrolyte gating approach due to the significantly smaller charge separation distances viable with this technique. Electrolyte-gated graphene is used for supercapacitor applications,<sup>16</sup> electronic biosensing applications,<sup>17</sup> and fundamental measurements of graphene properties at high carrier concentration.<sup>18,19</sup> Understanding the interface formed between the electrolyte and the graphene is critical to understanding how devices fabricated with these materials will respond to cell activity such as spiking of neurons.<sup>20</sup> This will be important for understanding the device response to neurons and biofilms as presented in chapters 4 and 5.

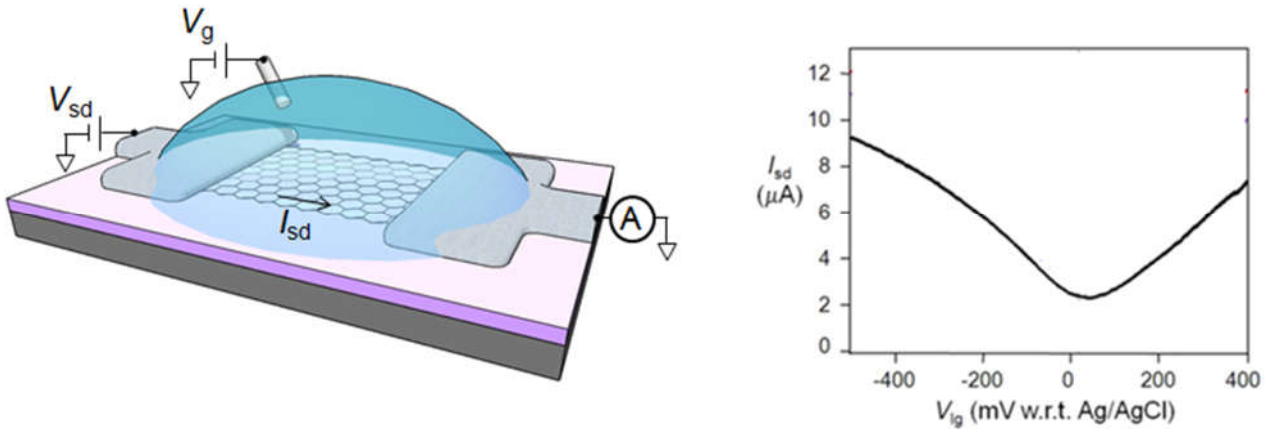


**Figure 3.** (a) Cartoon of a fluid gated graphene device showing applied source drain and gate voltages,  $V_g$  and  $V_{sd}$  respectively, as well as the resulting current,  $I_{sd}$ . (b) Gate response of a typical fluid gated graphene device.

When investigating electrolyte gating, an electrochemical cell is typically employed. This system consists of two solid electrical conductors (electrodes) separated by an ion conductor (electrolyte). In aqueous biological systems  $\text{H}^+$ ,  $\text{Na}^+$ ,  $\text{Cl}^-$ ,  $\text{Ca}^+$  are common electrolyte ions. Although bulk NaCl is non-conductive, when these ions dissociate in water they move similarly to free electrons in a metal with  $\rho \approx 1 \Omega \text{ m}$  for a concentration of  $\sim 100 \text{ mM}$  NaCl.<sup>20</sup> Modern super capacitor research continues to explore alternative non-aqueous electrolytes such as ionic liquids, ionic gels, and solid electrolytes. The potential is applied to a gate or reference electrode which is chosen from a standard set of inert materials which retain essentially constant composition. This results in the reference electrode having a fixed potential and allowing changes in the cell to be ascribed to the working electrode.

The potential which can be applied to the working electrode is limited by redox reactions. If the chemical potential for electrons in the working electrode is raised too high, or too low, electrons will transfer into (or out of) states in the electrolyte. The reduction/oxidation reactions result in the flow of a Faradaic current. In the ideal gating processes no redox reactions occur and no charge is transferred between the electrodes and the electrolyte, but current still flows to charge up the double layer as it forms on the working electrode. No electrodes exhibit this ideal behavior at for all applied voltages, however, it is a reasonable approximation for the low applied voltages applied to the devices described in subsequent chapters. The electrical contacts to the FET are also

isolated to minimize Faradaic currents. Redox reactions occur in aqueous electrolytes at around 1 volt, but other electrolytes can be brought to significantly higher potential. This is critical for increasing the power density of super capacitors which will be discussed in chapter 2.

#### 1.4.1 Electric double layer theory and the Debye screening length

When a potential is applied to the fluid gate, a layer of charged ions adheres to the surface of the working electrode; beyond this in the diffuse layer, the density of counter ions is assumed to decrease according to the Poisson-Boltzmann equation. This was first described by Helmholtz in 1853 and the layer of charges on the surface is commonly referred to as the Helmholtz layer. These layers can be approximated as two capacitors in parallel, where the thickness of the second capacitor approximately equals the Debye screening length.

As shown in Figure 4, the Helmholtz layer and diffuse layers form the electronic double layer (EDL). For metal working electrodes a total capacitance in the range of 10 to 40  $\mu\text{F}/\text{cm}^2$  is expected for aqueous electrolytes.<sup>20</sup> For a 10 mM aqueous electrolyte fluid the Debye screening length of  $\sim 3 \text{ nm}$  is approximated using Debye-Huckle theory, assuming  $\epsilon_{\text{water}} = 80$  for water. This represents the approximate distance into the electrolyte the working electrode can ‘see’, beyond which variations in electrolyte potential will not affect the working electrode. The formation of the EDL and how it interacts with cells is key to understanding the sensing mechanisms and the cell device interface described in chapter 5.

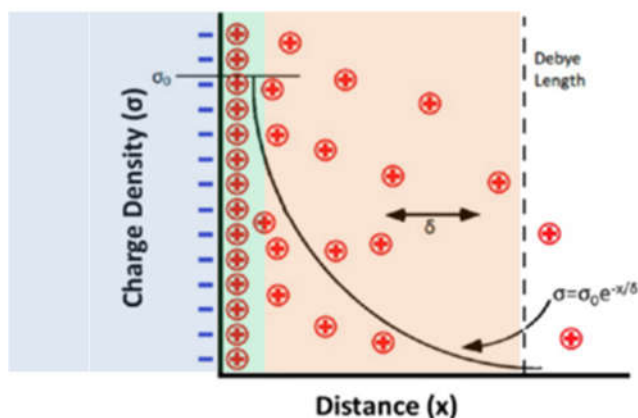


**Figure 4.** Ions in electrolyte gating from Stein et al,<sup>21</sup> where the blue area represents the solid device area, the green area the layer of ions adhered to the surface, and red area the diffuse layer.

### ***1.5 Electric Double Layer Capacitors***

Electric double layer capacitance has been experimentally investigated using both theoretical predictions and experimental methods which include cyclic voltammetry (CV), Galvanostatic charge/discharge measurements (CC), electrochemical impedance spectroscopy (EIS), and Hall effect measurements. These methods are briefly reviewed below, to give perspective on the use of Hall effect measurements in chapter 2.

CC and CV techniques are performed with a relatively simple experimental setup. However, test-to-test variability as high as 300% has been observed.<sup>22</sup> To minimize this, high capacitance values of ~0.25 F are recommended to achieve good signal to noise levels and minimize measurement errors.<sup>22</sup> This capacitance value is regularly achieved with supercapacitor designs. However, additional complexity is added by this high capacitance requirement. The high capacitance values required can be achieved by placing multiple devices in parallel, but this is not ideal due to the concern of variability between devices. Often high capacitance is typically achieved by increasing electrode surface area using rough or porous surfaces, but this makes the exact surface area hard to calculate. Reporting capacitance per mass is common for these electrode materials and avoids the need for difficult surface calculations; however this makes EDL investigations difficult.

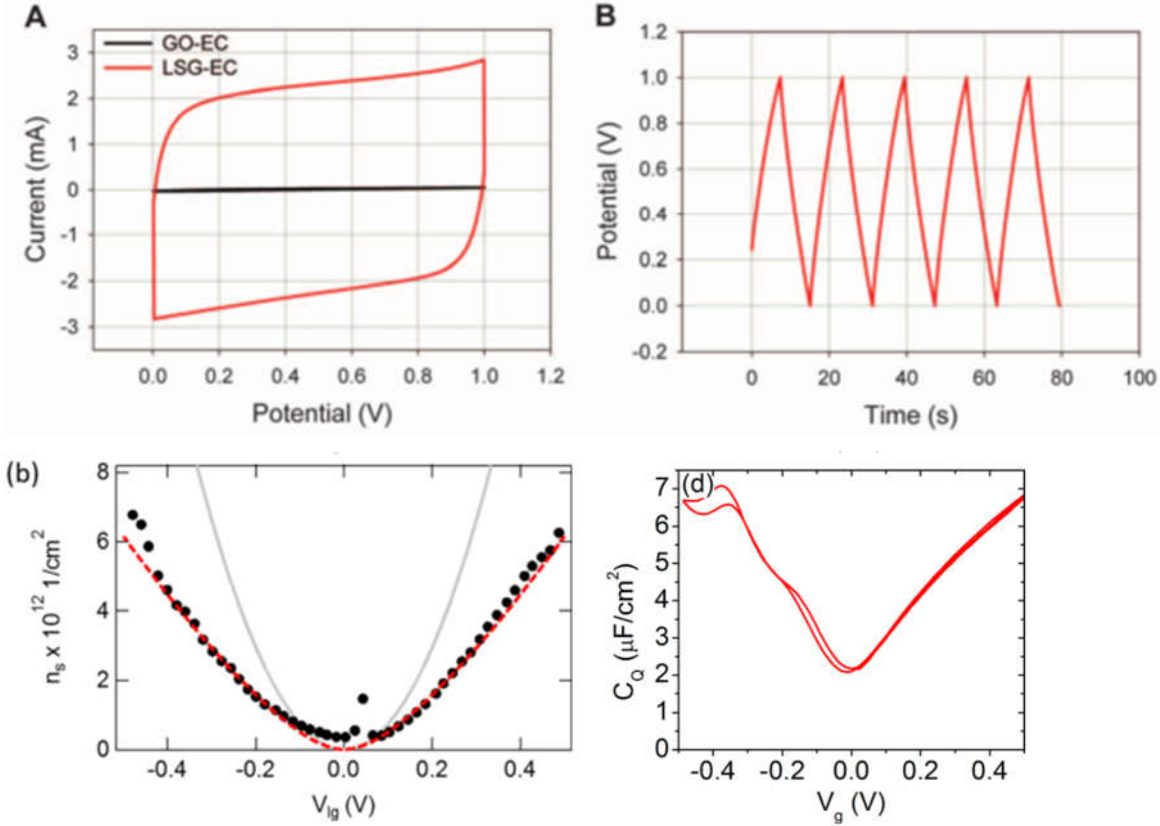


**Figure 5.** (a) Graphite CV and (b) CC response<sup>23</sup> (c) Hall based carrier density<sup>24</sup>, (d) Electrochemical impedance spectroscopy measurement<sup>25</sup>

CV measurements are performed by cycling the voltage with a constant scan rate. This rate is often in the range of 0.1 to 1 V/s. A rectangular trace in the current-voltage plane (Figure 5a) indicates efficient double layer formation. The maximum and minimum voltages are chosen to avoid the onset of Faradaic current. The region of this curve prior to the onset of Faradaic current is referred to as the capacitive potential region. A typical CV curve is shown in Fig. 5a, and the capacitance is either determined directly from the capacitive potential region, or the curve is integrated to determine the average value. Often capacitance values are averaged from a series of scan rates to reduce error. A similar process is performed for CC measurements in which a constant current of around 10 A/g is applied. The triangular traces in the voltage-time plane in Figure 5b indicate efficient double layer formation. Studies have indicated that the most repeatable capacitance values are determined by dividing current by the slope of the CC discharge curve.<sup>22</sup>

Using EIS, AC measurement techniques ameliorate the issues arising from the requirement of large capacitance and allow for the determination of capacitance at various frequencies and gate

voltages. An alternating voltage is applied to the electrode and the magnitude of the graphene-electrolyte impedance,  $Z$ , is measured using a lock-in amplifier. The total capacitance,  $C_{\text{total}}$ , is then equated to the measured quantity  $Z$ , where  $C_{\text{total}} = \frac{1}{2}\pi f|Z(f)|$ . The resulting capacitance can be determined at various frequencies and gate voltages as shown in Fig. 5d which was taken at 1000 Hz.

Hall effect measurements require the experimental complexity of introducing a magnetic field, however, the measurements allow direct determination of carrier density (Figure 5c). In addition these measurements also allow for the determination of carrier mobility in the graphene. The ability of graphene to amplify bioelectric signals is proportional to charge carrier mobility. This technique is described in detail in chapters 2 and 3.

### ***1.6 Device performance; Sensitivity and Noise Limit***

In order to assess sensor performance, both the sensitivity and noise levels must be understood. Our recent work proposes a fundamental thermal noise limit for graphene biotransistors.<sup>26</sup> We determined the Johnson noise generated at the graphene-electrolyte interface. Our results suggest that pristine, high-mobility graphene biosensor devices will approach the noise level shown in Figure 6. The noise power spectral density ( $S_V$ ) describes fluctuations in the gate voltage. The noise power spectral density,  $S_V$ , can be converted to the standard deviation of the effective gate voltage (right hand axis of Figure). These noise limits are relevant to chapters 5 and 6 influencing our choice of device geometry.

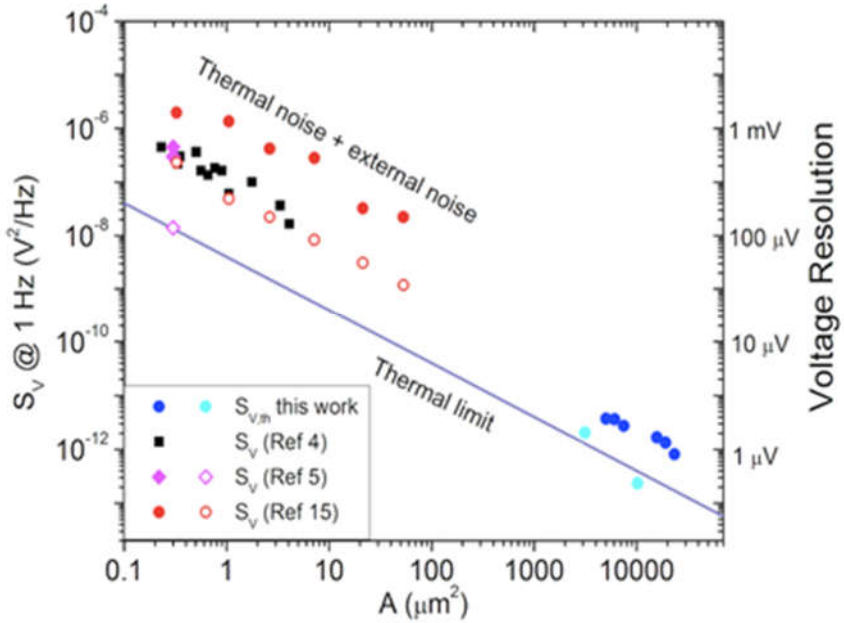


**Figure 6.** Plot of gate voltage noise power spectral density versus of liquid-gated GFETs. The solid line with slope  $A^{-1}$  shows our estimate for the thermal noise limit. Solid symbols correspond to GFET devices on oxide surfaces. Open symbols correspond to suspended GFET devices. Details can be found in Crosser et al.<sup>25</sup>

Figure 6 highlights the relationship between the surface area of a device, and the noise. There are a number of interesting trade-offs to consider when choosing the device area. Smaller devices enable higher spatial resolution, at the cost of increased noise. Another advantage of shrinking graphene dimensions is the emergence of a band gap. Narrow ribbons of graphene (width  $\sim 20$  nm) exhibit a band gap, which is sought after for logic-gates and other low power electronic applications.<sup>27</sup> However, the band gap is unnecessary for biotransistor applications. The low mobility values in graphene nanoribbons (a result of edge effects), rules out these devices for biosensor applications. Another advantage is seen by shrinking channel length. Experimental data has been presented by Venugopal et al. validating theoretical predictions that mobility increases as device length decreases below one micro meter.<sup>28</sup> They associate this with the occurrence of quasiballistic transport due to the mean free path length of  $\geq 200$  nm proposed by Tan et al.<sup>29</sup> However, this increase in mobility is overshadowed by the noise level found in devices of this size, making them unfavorable for biotransistor applications.

Prior to our work on fundamental noise limits (Fig. 6), Heller et al. experimentally observed that charge noise power scales inversely with device area.<sup>30</sup> Heller et al.'s observations fit well

with theoretical predictions from the augmented charge noise model proposed by Tersoff.<sup>31</sup> The model predicts that gate voltage fluctuations,  $S_V$ , will produce current fluctuations,  $S_I = (\frac{dI_{sd}}{dV_g})^2 S_V$ . A consequence of this relationship is that noise and sensitivity are both minimal at the Dirac point, where  $dI_{sd}/dV_g = 0$ .

The solution gate sensitivity of a graphene FET device is proportional to the transconductance,  $\frac{dI_{sd}}{dV_g}$ . Graphene FET devices exhibit superior transconductance when compared to devices based on materials such as Si, diamond, or AlGaN/ GaN.<sup>32</sup> These high transconductance values result of the high mobility of charge carriers in graphene and the graphene electrolyte interface. In chapters two and three we examine capacitance and charge carrier mobility, respectively, and set expectations for liquid gated graphene FET device performance. In chapter 5 the interface between graphene and cells is considered and the sensitivity is discussed in terms of the cleft resistance model.

### ***1.7 Effect of substrate on device performance***

Graphene biotransistors are typically fabricated on a doped Si substrate with a ~300 nm thick SiO<sub>2</sub> layer. This setup enhances the optical visibility of graphene and enables back gating. The role of the substrate in limiting mobility is well established. Mobility is lowered via phonon scattering, leading to the calculation of a theoretical mobility limit on SiO<sub>2</sub> substrates at room temperature due to phonon scattering of ~50,000 cm<sup>2</sup>V<sup>-1</sup>s<sup>-1</sup>.<sup>33</sup>

Experimental values have yet to reach this mobility limit, and Coulomb scattering from charge impurities in SiO<sub>2</sub> is believed to be the dominant driver of the observed values.<sup>34,35</sup> The surface of SiO<sub>2</sub> has a charge trap density of approximately 10<sup>12</sup> cm<sup>-2</sup>.<sup>36</sup> Charge traps can be visualized via STM.<sup>37</sup> The polarity of the charge traps has been further investigated, and it has been asserted that the asymmetry in mobility measured for hole and electron charge carriers is not due to band structure, which is symmetric, but is instead due to the predominance of negative trapped charges.<sup>38,39</sup> These issues with SiO<sub>2</sub> have lead researchers to consider other substrates. For example, Newaz et al.<sup>40</sup> explored the possibility of removing the SiO<sub>2</sub> completely, and leaving the graphene fully suspended.

In biosensing applications, the graphene is typically within close proximity to point charges in the liquid. For example, if the graphene is liquid gated (using monovalent ions) to have  $10^{12} \text{ cm}^{-2}$  charge carriers, there will be  $10^{12} \text{ cm}^2$  charged ions in the layer of liquid that contacts the graphene. Thus, liquid gating can introduce surface concentrations of point charges that are similar to the concentration of trapped charges in the silicon oxide substrate. In chapter 3, we explore the effect of these charged scattering centers that are introduced during liquid gating.

Although suspended graphene offers high mobility, it is not viable for experiments. Hexamethyldisilazane (HMDS) was initially tested as a substrate coating to minimize interaction with oxide-based charge traps, and a minimal increase in mobility was observed.<sup>41</sup> HMDS has the advantage that application is simple and it is able to cover large areas. A significant increase in mobility was observed by Dean et al. when hexagonal boron nitride (BN) was mechanically exfoliated on the  $\text{SiO}_2$  substrate.<sup>42</sup> This material is theorized to increase mobility due to the lack of dangling bonds, smooth surface, similar lattice constant, and large band gap. Dean reported mobility values of  $\sim 60,000 \text{ cm}^2\text{V}^{-1}\text{s}^{-1}$  for back-gated devices on hBN in ambient conditions. This represents an increase of approximately three times the mobility observed for similar devices on  $\text{SiO}_2$ . Although the associated increase in mobility has been experimentally validated, the significance of some of the stated mechanisms remain contested, such as the role of lattice constant.<sup>12</sup> Some debate also remains regarding the quality of chemical-vapor-deposited (CVD) BN relative to exfoliated BN. There is one report of high-mobility graphene devices on CVD BN.<sup>43</sup> The availability and viability of CVD BN would allow for the fabrication of scalable arrays of graphene devices with a variety of potential applications in biosensing. An alternative, novel process for the removal and application of graphene devices on cells is described in chapter 5.

### ***1.8 What do we actually sense from cells?***

Graphene is well suited for biosensing applications because it is a biocompatible FET and all atoms can be placed in contact with the system under test. Local shifts in potential result in shifts of the Fermi level of FET devices, allowing us to dope the graphene either n or p type and altering its resistance value without physically altering the sample. A shift in the Dirac point is associated with the addition of biological elements such as bacteria, eukaryote cells, or living tissue samples to graphene biotransistors.<sup>44,17</sup> Many cellular processes of interest also result in changes in the local potential. For instance, the substrate consumption of ammonia oxidizing bacteria, which is

critical to the nitrogen cycle, also decrease the local pH. The local increase in  $\text{H}^+$  ions associated with this pH shift can then be used to observe substrate consumption and investigate this process with impressive temporal and spatial resolution.

When a neuron fires, ion channels transport negatively charged ions out of the cell. The resulting local decrease in potential, relative to the fluid potential far from the cell, shifts the potential of a graphene device near the cell as shown in Figure 7. Graphene FET device response to biofilm substrate consumption and the electrogenic cell activity is explored in chapters 4 and 5 respectively.

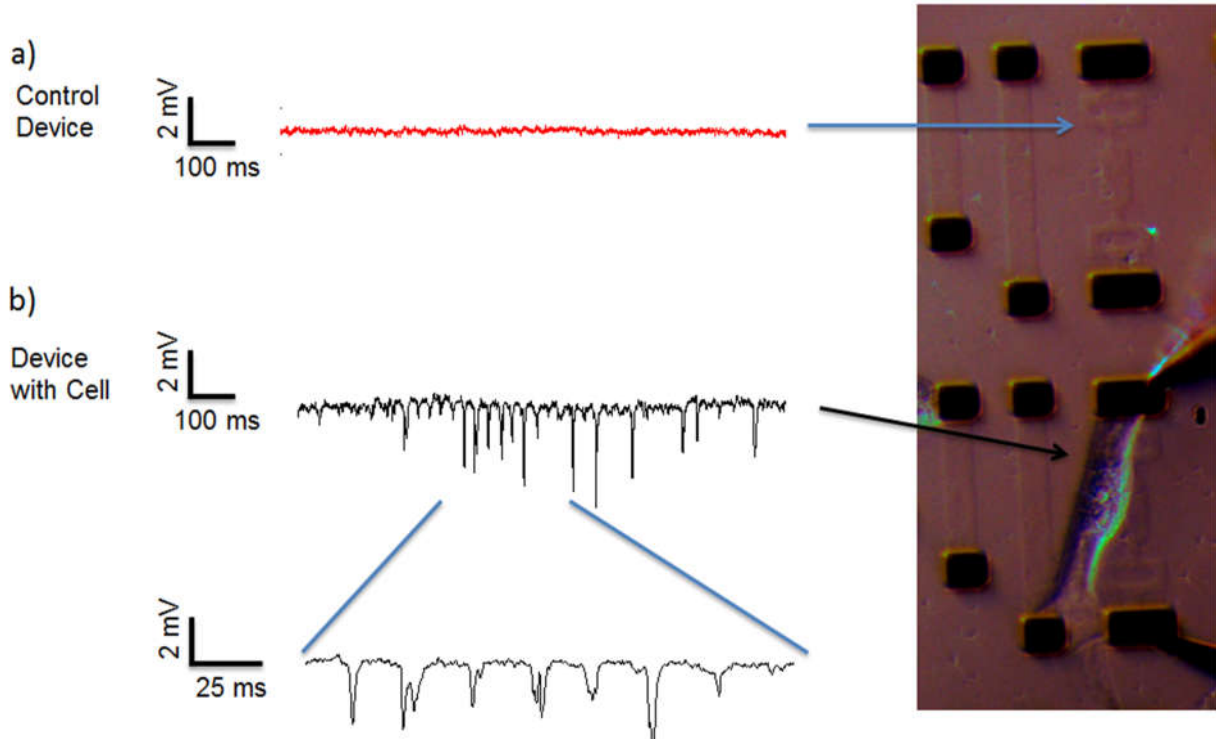


**Figure 7.** Graphene FET device response (a) to a control environment, (b) to the electrogenic activity of an immortalized hypothalamic neuron.

### 1.9 Graduate work not included in this thesis

I have been involved in several projects that lie outside the scope of this dissertation. Below are brief summaries of the peer-reviewed work to which I have contributed as a co-author, along with descriptions of my involvement in each project. The work is divided into two subsets: (1) Carbon Nanotube (2) Graphene.

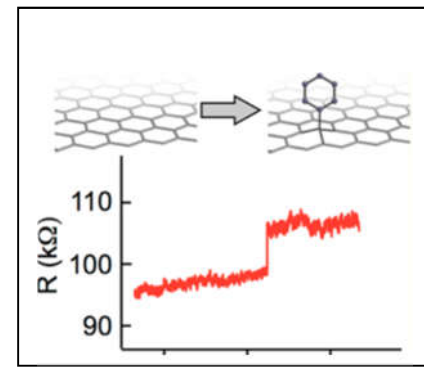
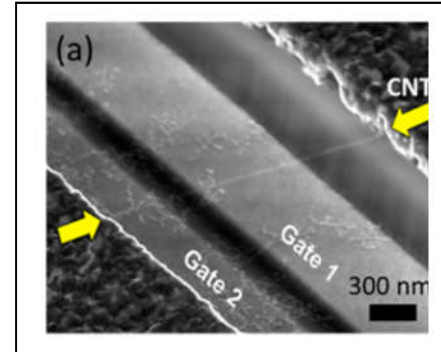
#### Carbon Nanotubes

1. L. Aspitarte, D. McCulley, E. D. Minot, 'Photocurrent Quantum Yield in Suspended Carbon Nanotube p-n Junctions', *Nano Letters*, 5589 (2016)

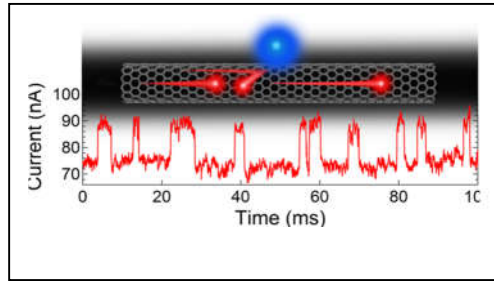
Carbon nanotubes based photovoltaics have the potential for higher efficiency than traditional Si based devices because of the possibility of reaching quantum yields above 100%. This paper advances the field by measuring the highest reported room temperature quantum yield of 30%. My contribution to this work was the scanning electron microscope imaging that was required to verify that CNTs are suspended, the suspended length, and the height above the surface.

2. H. Wilson, S. Ripp, L. Prisbrey, **M. A. Brown**, T. Sharf, D. J. Myles, K. G. Blank, E. D. Minot, 'Electrical Monitoring of  $sp^3$  Defect Formation in Individual Carbon Nanotubes,' *The Journal of Physical Chemistry C.*, 1971 (2016)

Many carbon nanotube applications require chemical functionalization. The introduction of  $sp^3$  defects is a promising way to address this need with minimal effect on the overall electrical performance of the device. This paper offers a process to accomplish this in a controlled manner. My contribution to this study was the fabrication and testing of single carbon nanotubes with a microfluidic system. I acquired and analyzed the data in Figure 1, and then created Figure 1. I also re-analyzed the data presented in Figure 2, and created Figure 2.



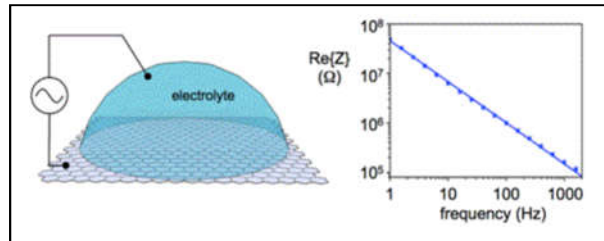
3. T. Sharf, N. Wang, J. W. Kevek, M. A. Brown, H. Wilson, S. Heinze, E. D. Minot, 'Single Electron Charge Sensitivity of Liquid-Gated Carbon Nanotube Transistors,' *ACS Nano Letters*, 4925 (2014)



Random telegraph signals corresponding to activated charge traps were investigated in single carbon nanotube based FET devices. The viability of single electron charge sensing was. My contribution to this paper was the design and fabrication of n-type contacts onto individual CNTs. I measured these devices to demonstrate that negative charge traps interact differently with electrons versus holes. I helped create Fig. 5b.

## Graphene

1. M. S. Crosser, M. A. Brown, P. L. McEuen, E. D. Minot, 'Determination of the Thermal Noise Limit of Graphene Biotransistors,' *ACS Nano Letters*, 5404 (2015)



The thermal noise limit of graphene biotransistors was determined by measuring the complex impedance between the basal plane of single-layer graphene and an aqueous electrolyte. Michael and I worked closely together on fabrication, data collection, and analysis.

- <sup>1</sup> Y. Huang, X. Dong, Y. Liu, L.-J. Li, and P. Chen, *J. Mater. Chem.* **21**, 12358 (2011).
- <sup>2</sup> A. Prindle, J. Liu, M. Asally, S. Ly, J. Garcia-Ojalvo, G.M. Suel, and G.M. Suel, *Nature* **527**, 59 (2015).
- <sup>3</sup> M. Ackermann, *Science* (80- ). **300**, 1920 (2003).
- <sup>4</sup> C. Xie, J. Liu, T.-M. Fu, X. Dai, W. Zhou, and C.M. Lieber, *Nat. Mater.* **14**, (2015).
- <sup>5</sup> Z.C. Lin, C. Xie, Y. Osakada, Y. Cui, and B. Cui, *Nat. Commun.* **5**, 3206 (2014).
- <sup>6</sup> G. Buzsáki, *Nat. Neurosci.* **7**, 446 (2004).
- <sup>7</sup> D. Khodagholy, J.N. Gelinas, T. Thesen, W. Doyle, O. Devinsky, G.G. Malliaras, and G. Buzsaki, *Nat Neurosci* **18**, 310 (2015).
- <sup>8</sup> A.K. Geim and K.S. Novoselov, *Nat. Mater.* **6**, 183 (2007).
- <sup>9</sup> G.-H. Lee, R.C. Cooper, S.J. An, S. Lee, A. van der Zande, N. Petrone, A.G. Hammerberg, C. Lee, B. Crawford, W. Oliver, J.W. Kysar, and J. Hone, *Science* **340**, 1073 (2013).
- <sup>10</sup> M. Klintenberg, S. Lebègue, C. Ortiz, B. Sanyal, J. Fransson, and O. Eriksson, *J. Phys. Condens. Matter* **21**, 335502 (2009).
- <sup>11</sup> B. Partoens and F.M. Peeters, *Phys. Rev. B - Condens. Matter Mater. Phys.* **74**, 1 (2006).
- <sup>12</sup> K.I. Bolotin, K.J. Sikes, Z. Jiang, M. Klima, G. Fudenberg, J. Hone, P. Kim, and H.L. Stormer, *Solid State Commun.* **146**, 351 (2008).
- <sup>13</sup> S. Das Sarma, S. Adam, E.H. Hwang, and E. Rossi, *Rev. Mod. Phys.* **83**, 407 (2011).
- <sup>14</sup> E. Hwang, S. Adam, and S. Sarma, *Phys. Rev. Lett.* **98**, 186806 (2007).
- <sup>15</sup> M. Weinert, G. Schneider, R. Podloucky, and J. Redinger, *J. Phys. Condens. Matter* **21**, 84201 (2009).
- <sup>16</sup> K.S. Novoselov, V.I. Fal'ko, L. Colombo, P.R. Gellert, M.G. Schwab, and K. Kim, *Nature* **490**, 192 (2012).
- <sup>17</sup> Y. Liu, X. Dong, and P. Chen, *Chem. Soc. Rev.* **41**, 2283 (2012).
- <sup>18</sup> J. Ye, M.F. Craciun, M. Koshino, S. Russo, S. Inoue, H. Yuan, H. Shimotani, A.F. Morpurgo, and Y. Iwasa, *Proc. Natl. Acad. Sci. U. S. A.* **108**, 13002 (2011).
- <sup>19</sup> R.S. Gonnelli, E. Piatti, A. Sola, M. Tortello, F. Dolcini, S. Galasso, J.R. Nair, C. Gerbaldi, E. Cappelluti, M. Bruna, and A.C. Ferrari, *2D Mater.* **4**, 35006 (2017).
- <sup>20</sup> P. Massobrio, G. Massobrio, and S. Martinoia, *Front. Neurosci.* **10**, 1 (2016).
- <sup>21</sup> R. Stine, S.P. Mulvaney, J.T. Robinson, C.R. Tamanaha, and P.E. Sheehan, *Anal. Chem.* **85**, 509 (2013).
- <sup>22</sup> M.D. Stoller and R.S. Ruoff, 1 (n.d.).
- <sup>23</sup> S. De Liberato, C. Ciuti, D. Auston, M. Nuss, S. Keiding, M. Van Exter, C. Fattinger, A.J. Taylor, C. Highstrete, M. Lee, R.D. Averitt, E. Smirnova, A. Azad, H. Chen, G. Scalari, M.I. Amanti, M. Beck, and J. Faist, *Science* (80- ). **335**, 1326 (2012).

- <sup>24</sup> M.A. Brown, M.S. Crosser, M.R. Leyden, Y. Qi, and E.D. Minot, *Appl. Phys. Lett.* **109**, 93104 (2016).
- <sup>25</sup> M.S. Crosser, M. a. Brown, P.L. McEuen, and E.D. Minot, *Nano Lett.* **15**, 5404 (2015).
- <sup>26</sup> M.S. Crosser, M. a. Brown, P.L. McEuen, and E.D. Minot, *Nano Lett.* 150720103852006 (2015).
- <sup>27</sup> M.Y. Han, B. Özyilmaz, Y. Zhang, and P. Kim, *Phys. Rev. Lett.* **98**, 1 (2007).
- <sup>28</sup> A. Venugopal, J. Chan, X. Li, C.W. Magnuson, W.P. Kirk, L. Colombo, R.S. Ruoff, and E.M. Vogel, *J. Appl. Phys.* **109**, 1 (2011).
- <sup>29</sup> Y.W. Tan, Y. Zhang, K. Bolotin, Y. Zhao, S. Adam, E.H. Hwang, S. Das Sarma, H.L. Stormer, and P. Kim, *Phys. Rev. Lett.* **99**, 10 (2007).
- <sup>30</sup> I. Heller, S. Chatoor, J. Männik, M. a G. Zevenbergen, J.B. Oostinga, A.F. Morpurgo, C. Dekker, and S.G. Lemay, *Nano Lett.* **10**, 1563 (2010).
- <sup>31</sup> J. Tersoff, *Nano Lett.* **7**, 194 (2007).
- <sup>32</sup> L.H. Hess, M. V. Hauf, M. Seifert, F. Speck, T. Seyller, M. Stutzmann, I.D. Sharp, and J.A. Garrido, *Appl. Phys. Lett.* **99**, 33503 (2011).
- <sup>33</sup> J.-H. Chen, C. Jang, S. Xiao, M. Ishigami, and M.S. Fuhrer, *Nat. Nanotechnol.* **3**, 206 (2008).
- <sup>34</sup> S. Das Sarma, S. Adam, E.H. Hwang, and E. Rossi, *Rev. Mod. Phys.* **83**, 407 (2011).
- <sup>35</sup> J. Yan and M.S. Fuhrer, *Phys. Rev. Lett.* **107**, 1 (2011).
- <sup>36</sup> S. Cho and M.S. Fuhrer, *Phys. Rev. B - Condens. Matter Mater. Phys.* **77**, 8 (2008).
- <sup>37</sup> R. Decker, Y. Wang, V.W. Brar, W. Regan, H. Tsai, Q. Wu, W. Gannett, A. Zettl, and M.F. Crommie, *Nano Lett.* 2291 (2011).
- <sup>38</sup> D.S. Novikov, *Phys. Rev. B - Condens. Matter Mater. Phys.* **76**, 1 (2007).
- <sup>39</sup> Z. Ong and M. V Fischetti, arXiv Prepr. arXiv1207.6167 4 (2012).
- <sup>40</sup> A.K.M. Newaz, Y.S. Puzyrev, B. Wang, S.T. Pantelides, and K.I. Bolotin, *Nat. Commun.* **3**, 734 (2012).
- <sup>41</sup> J. Chan, A. Venugopal, A. Pirkle, S. McDonnell, D. Hinojos, C.W. Magnuson, R.S. Ruoff, L. Colombo, R.M. Wallace, and E. Vogel, *ACS Nano* **6**, 3224 (2012).
- <sup>42</sup> C.R. Dean, a F. Young, I. Meric, C. Lee, L. Wang, S. Sorgenfrei, K. Watanabe, T. Taniguchi, P. Kim, K.L. Shepard, and J. Hone, *Nat. Nanotechnol.* **5**, 722 (2010).
- <sup>43</sup> D. a. Boyd, W.-H. Lin, C.-C. Hsu, M.L. Teague, C.-C. Chen, Y.-Y. Lo, W.-Y. Chan, W.-B. Su, T.-C. Cheng, C.-S. Chang, C.-I. Wu, and N.-C. Yeh, *Nat. Commun.* **6**, 6620 (2015).
- <sup>44</sup> Z. Cheng, J. Hou, Q. Zhou, T. Li, H. Li, L. Yang, K. Jiang, C. Wang, Y. Li, and Y. Fang, *Nano Lett.* **13**, 2902 (2013).

## CHAPTER 2

### **Electric double-layer capacitance and the performance limits of graphene based supercapacitors**

Morgan Brown, Zhenxiang Feng, Michael Crosser, Ethan Minot

Manuscript currently in preparation for submission.

## 2.1 Introduction

Electric double layer (EDL) capacitors, or super capacitors, offer significantly reduced charge times, longevity, and higher power density compared to Li-ion batteries.<sup>1</sup> However, the energy storage density of EDL capacitors is currently too low for many applications. For example, commercial EDL capacitors with activated-carbon electrodes have an energy density of ~12 Wh/kg (43 J/g), whereas commercial lithium ion batteries have an energy density ~ 180 Wh/kg (~600 J/g).<sup>2</sup> To overcome the issue of energy density, EDL capacitors are being developed with graphene-like electrodes. Optimistic authors have predicted a specific capacitance of ~550 F/g (dry weight before adding electrolyte) for such EDL capacitors. Such a capacitor would be competitive with lithium ion batteries when charged to 1 or 2 V (~600 J/g). However, this goal has yet to be reached and understanding and engineering of the EDL at graphene electrolyte interfaces is a critical step to achieving it.

Electric double layer capacitance has been studied for over a century using conductive liquids and metal surfaces. This body of knowledge can be applied to estimate the properties of the interface between graphene and a conductive liquid. To estimate the ultimate performance of a graphene-based EDL capacitor, previous authors have used the interfacial capacitance between a bulk platinum surface and an ionic liquid (~20  $\mu$ F/cm<sup>2</sup>), and the specific surface area of graphene (~2500 m<sup>2</sup>/g)<sup>3,4,5</sup> to predict a specific capacitance of 550 F/g.

The actual accessible surface area of carbon-based electrodes for EDL capacitor applications varies greatly. Activated carbon electrodes have a specific area ~100 m<sup>2</sup>/g, while carbon black can approach 1000 m<sup>2</sup>/g.<sup>5</sup> These values are approximate for two reasons. First, there is variability in the fabrication process of 3-dimensional porous electrodes. Second, there is no

exact method of determining the accessible surface area of 3-dimensional porous electrodes. The best techniques are based on nitrogen gas adsorption/desorption measurements.<sup>6</sup>

There has been recent progress towards fabricating porous carbon-based electrodes with specific surface area > 1000 m<sup>2</sup>/g. Early work in this area by Stoller et al using a graphene oxide based process claimed 705 m<sup>2</sup>/g.<sup>7</sup> El-Kady et al. recently showed significant progress, claiming 1520 m<sup>2</sup>/g using a laser scribing technique.<sup>8</sup>

Assuming that researchers can create graphene-based material with specific area close to 2500 m<sup>2</sup>/g, there are still unanswered questions about the interfacial capacitance that can be achieved. Only recently have careful studies of C<sub>EDL</sub> focused on the interface between graphene and conductive liquids.<sup>9,10,11</sup> These studies are challenging because it is difficult to accurately determine both C<sub>EDL</sub> and the accessible surface area. For large-surface-area porous electrodes, C<sub>EDL</sub> is typically measured using a 2 or 3 electrode electrochemical cell configuration using galvanostatic constant current (CC), cyclic voltammetry (CV), or AC based techniques.<sup>3,4,8,12,13</sup> Both CC and CV techniques are subject to inconsistent results which vary with changes in cycle rate, current, and accessible surface area. The techniques require devices with large capacitance values (~ 0.25 F) to overcome parasitic effects. The end result of such experiments is that both the capacitance and the surface area remain poorly quantified; making the fundamental properties of the graphene liquid interface unclear.

An alternative approach is to use small-surface-area EDL capacitors based on a single-sheet of graphene. The surface area can be precisely determined because the graphene is spread across an atomically flat surface and the area is measured using optical imaging. Equally important, the density of charge carriers in the graphene can be measured using the Hall effect,

thus circumventing the uncertainties associated with CC and CV techniques. Such Hall effect measurements in liquid environments were recently achieved by our group and others.<sup>14,15</sup> With precise measurements of both surface area and capacitance, we seek to address fundamental questions about the graphene electrolyte interface including the structure of the liquid at the interface, the dielectric behavior of the liquid, the arrangement of dissolved ions at the interface, and the effect of changing the size of the ionic species. Answers to these questions will aid in the fabrication of super capacitors with higher power density as well as enabling fundamental studies of higher carrier density in graphene and elucidate the cell/device interface to increase sensitivity in biosensor applications.

Our work illustrates that important differences may arise when comparing  $C_{EDL}$  at a bulk-metal/liquid interface to a graphene/liquid interface. In this work we determine the  $C_{EDL}$  for a set of conducting liquids common for biosensing and supercapacitor applications. We show that although ionic liquids can approach the “ideal”  $C_{EDL} = 20 \mu\text{F}/\text{cm}^2$ , aqueous electrolytes have significantly lower values.  $\text{Na}_2\text{SO}_4$ , another common super capacitor electrolyte, and 100 mM  $\text{NaCl}$ , a common biosensing medium, both have a  $C_{EDL}$  of  $\sim 4 \mu\text{F}/\text{cm}^2$ . In addition to low values for  $C_{EDL}$ , the low density of states for electrons in graphene reduces the total capacitance,  $C_{Total}$ , of the graphene-electrolyte interface even more severely.

## ***2.2 Previous work on single-layer graphene capacitors***

Pioneering work by Xia et al. confirmed that the capacitance between graphene and a conductive liquid depends on the charge carrier density in the graphene.<sup>3</sup> When more charge carriers are present, the capacitance is larger. This phenomena is explained by quantum capacitance: the electronic density of states in graphene is small and therefore affects the overall

capacitance of the liquid-graphene interface. Xia's measurements are often cited as evidence that graphene supercapacitors can reach specific capacitance of  $20 \mu\text{F}/\text{cm}^2$ . However, the maximum specific capacitance obtained in Xia's experiments was approximately  $3 \mu\text{F}/\text{cm}^2$  (an additional  $4 \mu\text{F}/\text{cm}^2$  was attributed to parasitic background capacitance). An additional complication to interpreting Xia's measurements is the use of the impedance spectroscopy method to measure capacitance (see Chapter 1, section 5). Significant work remains to demonstrate the technologically important goal of  $20 \mu\text{F}/\text{cm}^2$ .

### 2.3 Quantum capacitance

Because graphene has a low density of states, a second “effective capacitor” must be taken into account in series with the double layer. As shown in Fig. 1, for materials with low density of states such as graphene, the filling or emptying of bands must be taken into account. Assuming a tight binding model for the graphene dispersion relation, sheet carrier density,  $n_s$ , scales as  $E_F^2$ ,

$$n_s = \frac{1}{\pi} \left( \frac{E_F}{\hbar v_F} \right)^2, \quad (1)$$

where  $E_F$  is the Fermi energy measured relative to the Dirac point, the Fermi velocity is  $v_F \sim 10^6 \text{ ms}^{-1}$ , and  $\hbar$  is the reduced Plank constant. The quantum capacitance of graphene,  $C_Q = e^2(dn_s/dE_F)$ , approaches zero as  $E_F$  approaches zero. If  $C_{\text{EDL}} \gg C_Q$ ,  $C_Q$  limits  $n_s$  such that  $n_s \approx (10^{14} \text{ cm}^{-2}\text{V}^{-2}) \cdot V_{\text{lg}}^2$ .

To understand the relationship between  $n_s$  and  $V_{\text{lg}}$ , we consider both the graphene density of states and the double-layer capacitance between the electrolyte gate and carriers in the graphene,

$C_{EDL}$ .<sup>3</sup> The total capacitance of the interface between liquid and graphene then depends on both  $C_{EDL}$  and quantum capacitance,  $C_Q$ ,

$$C_{Total} = \left( \frac{1}{C_Q} + \frac{1}{C_{EDL}} \right)^{-1}. \quad (2)$$

The variation in  $C_Q$  for a typical single layer graphene device is shown in Fig. 1b. Understanding  $C_Q$  and  $C_{EDL}$  is critical to setting reasonable goals for future supercapacitors as a function of fluid choice and the associated maximum applied voltage.

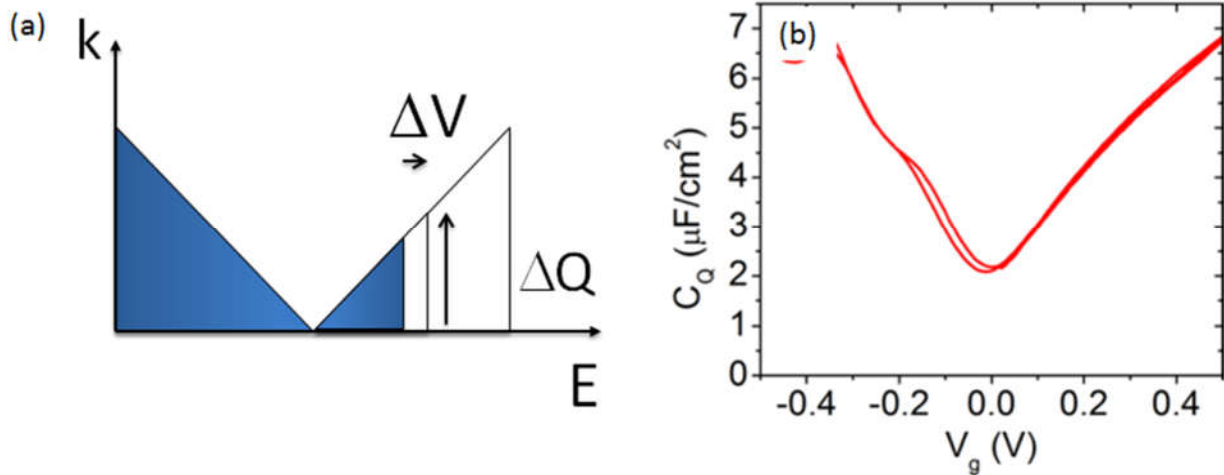


**Figure 1** (a) Graphene  $k$  vs  $E$  diagram. (b)  $C_Q$  vs. applied fluid gate voltage ( $V_g$ ) at 1000 Hz, from Crosser et al.<sup>16</sup>

The highest reported  $n_s$  in single layer graphene is  $\sim 2 \times 10^{14} \text{ cm}^{-2}$ .<sup>17,10</sup> Reaching this exceptionally high doping level requires high sample quality and an electrochemically stable fluid. Assuming this doping level is reached, we predict that  $C_Q \sim 18 \mu\text{F}/\text{cm}^2$ . Equation 2 shows that  $C_{Total}$  can be considerably less than  $C_Q$ . The exact value of  $C_{EDL}$  is a critical parameter for determining  $C_{Total}$ .

## 2.4 Experimental Methods

Graphene on copper foil was produced in our chemical vapor deposition system. Copper foil (25  $\mu\text{m}$  thickness, Alfa Aesar) was cleaned with dilute nitric acid (5%) followed by acetic acid.<sup>18</sup> The foil was annealed for 60 min in H<sub>2</sub> gas at 1070°C, before starting graphene deposition (30 min at 1070°C, 20 sccm H<sub>2</sub>, 30 sccm CH<sub>4</sub>, pressure 50 Pa).<sup>19</sup> A wet transfer process was used to place the graphene on an Si/SiO<sub>2</sub> substrate (300 nm thermally-grown oxide).<sup>20</sup> The graphene was patterned using a two-layer photolithography process (Shipley S1813 photoresist over a base layer of MicroChem LOR) and O<sub>2</sub> plasma. A second photolithography step was used to create metal electrodes encapsulated by SiO<sub>2</sub> (5 nm Cr, 30 nm Au, 70 nm SiO<sub>2</sub>). The electrode materials were deposited via e-beam evaporation. After device fabrication the graphene was characterized using microRaman spectroscopy (see supplementary material). Figure 2 shows a completed device, in which  $L = w = 40 \mu\text{m}$ .

An aqueous electrolyte, 1 M Na<sub>2</sub> SO<sub>4</sub>, and an ionic liquid, 1-Butyl-3-methylimidazolium hexafluorophosphate (BMIM-PF<sub>6</sub>), were chosen for these tests based on their common use in supercapacitor applications. Ionic liquids are commonly used because they have significantly lower ionic Debye screening layers than aqueous electrolytes, resulting in higher EDL capacitance values and because they are stable at higher potentials.<sup>2,4,21</sup> In addition ionic liquids are ideal because they are stable and chemically inert, resulting in fewer contamination concerns. A second aqueous electrolyte, 100 mM NaCl, was chosen as it is representative of those used in biosensing applications.

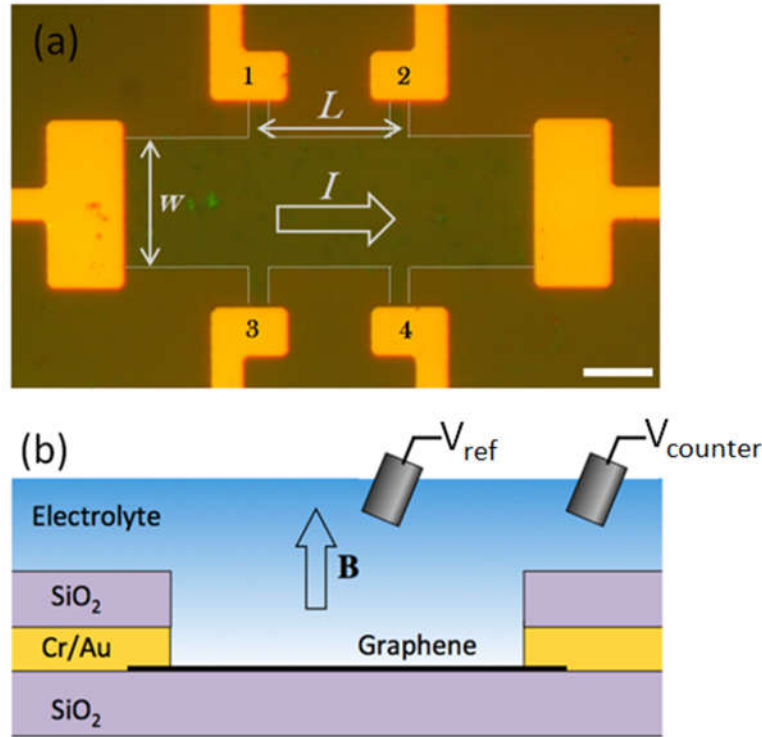


**Figure 2.** Device geometry. (a) Hall bar geometry with constant current applied as indicated. Dashed white lines show the edge of the patterned graphene. The numbered electrodes are used to measure voltage differences; for example,  $V_{13}$  is the voltage difference between electrodes 1 and 3. Scale bar 20  $\mu\text{m}$ . (b) Cross-sectional diagram of the device. The Cr/Au contacts are capped in  $\text{SiO}_2$ . The magnetic field is perpendicular to the graphene.

The electrostatic potential of the liquid,  $V_{\text{ref}}$ , was measured with a tungsten wire submerged in the liquid. The potential of the liquid was controlled by applying a voltage,  $V_{\text{counter}}$ , to a second tungsten wire immersed in the electrolyte. A relationship of  $V_{\text{ref}} = 0.8 V_{\text{counter}}$  was established and applied for subsequent single electrode experiments with identical configurations. A current source (Keithley 2400 Source meter) was used to supply and maintain a constant current,  $I = 5 \mu\text{A}$ . The magnetic field,  $B$ , was applied perpendicular to the graphene using a variable-field electromagnet ( $\pm 0.5 \text{ T}$ ). The isolating layer of  $\text{SiO}_2$  applied over the Au device contacts effectively limited parasitic currents between the gate and electrodes. Gate voltage sweeps were performed at a rate of 10 mV/s.

Figure 3 shows the Hall voltage,  $V_H$ , measured when  $B = \pm 0.5$  T. The measurement procedure is as follows. First,  $V_{13}$  is measured at  $B = 0$  to establish the gate-dependent background voltage. This background voltage (of the order 0.1 mV) is related to the spatial inhomogeneity in the electrolyte gate potential. Next,  $V_{13}$  is measured at  $B = \pm 0.5$  T. The Hall voltage is then  $V_H = V_{13}(B = \pm 0.5 \text{ T}) - V_{13}(B = 0)$ .

When  $B > 0$  (blue line),  $V_H$  is positive for hole-type transport and negative for electron transport. When  $B < 0$  (black), the sign of  $V_H$  reverses. The transition from hole transport to electron transport occurs at the Dirac point,  $V_D \sim 0.03$  V with respect to the tungsten counter electrode.

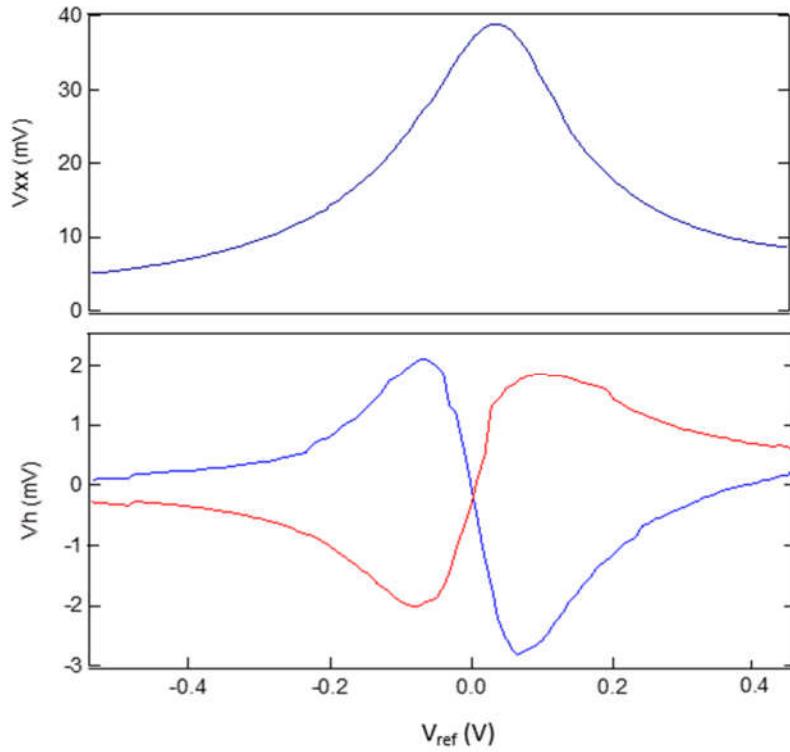


**Figure 3.** Hall-effect measurements of electrolyte-gated graphene. The aqueous electrolyte is  $\text{Na}_2\text{SO}_4$ . (a) The  $V_{xx}$  measured with constant current,  $I_{sd} = 5\mu\text{A}$ . (b) The Hall voltage,  $V_H$ , measured when  $B = \pm 0.5$  T. The raw  $V_{13}$  data (not shown) includes a gate-dependent background ( $\sim 0.1$  mV) that has been subtracted.

## 2.5 Results and discussion

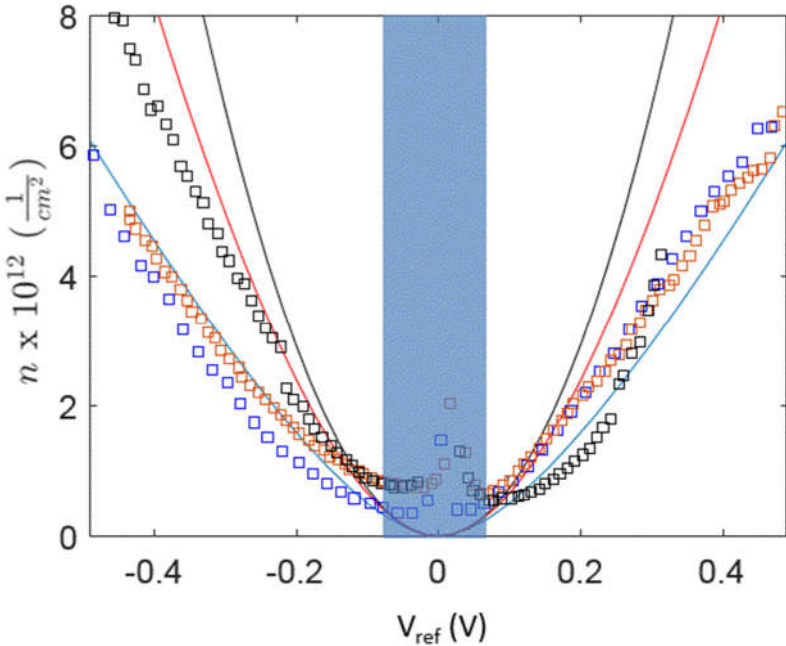


**Figure 4.** Carrier density data from hall measurements for 100 mM NaCl (blue squares), 1M Na<sub>2</sub>SO<sub>4</sub> (orange squares), and BMIM-PF<sub>6</sub> (Black squares). The black line represents the calculated density for  $C_{EDL} \gg C_Q$  (the quantum capacitance limit). The red and blue line are calculated from Eq. (3) with  $C_{EDL} = 20$  and  $4 \mu\text{F}/\text{cm}^2$  respectively. The area close to the Dirac point,  $V_{ref} = 0$ , is shaded as it is difficult to estimate the carrier density in this region.

Sheet carrier density is inversely proportional to the Hall voltage,

$$n_s = \frac{BI}{V_H e}, \quad (3)$$

where,  $n_s$ , is sheet carrier density,  $B$  is the magnetic field,  $V_H$ , is the Hall voltage and  $e = 1.6 \times 10^{-19}$  C. We calculated  $n_s$  as a function of  $V_{ref}$  using Eq. 3 for two aqueous electrolytes and an ionic

liquid. The aqueous electrolyte curve agrees with others,<sup>15</sup> confirming contrary to the predictions made with the standard Debye-Huckel (DH) model, that the total capacitance cannot simply be described by  $C_Q$ .<sup>12</sup>

The value of  $C_{EDL}$ , can then be determined for each data set by modeling the system as two capacitors in series. The sheet charge density on  $C_{EDL}$  and  $C_Q$  is equal, and the voltage across each capacitor adds to  $V_{ref}$ . The relationship between  $V_{ref}$  and  $n_s$  is described by

$$V_{ref} = \frac{\hbar v_F \sqrt{\pi n_s}}{e} + \frac{en_s}{C_{EDL}}. \quad (4)$$

By fitting Eq. 4 to our experimental data we determine that  $C_{EDL}$  is  $\sim 4 \mu\text{F}/\text{cm}^2$  for both the 100 mM NaCl and 1M Na<sub>2</sub> SO<sub>4</sub> fluids. Our  $C_{EDL}$  values agree well with those found using a model developed by Dankerl et al. for the spatial charge and electrostatic potential distributions at a graphene/electrolyte interface, who also found  $C_{EDL} = \sim 3 \mu\text{F}/\text{cm}^2$  when 100 mM NaCl.<sup>15</sup> The capacitance is higher for the ionic liquid when  $V_{ref} < 0$ , with  $C_{EDL}$  reaching  $\sim 20 \mu\text{F}/\text{cm}^2$ .

The measured  $n_s$  values deviate from eq. 4 at small  $V_{lg}$ . In this low-doping regime,  $n_s$  is dominated by electrostatic disorder in the graphene. We find a disorder-induced carrier concentration,  $n_{s,disorder} \sim 0.5 \times 10^{12} \text{ cm}^{-2}$ , for our devices which is typical for SiO<sub>2</sub>-supported graphene.<sup>22</sup>

A significant asymmetry is seen in the  $n_s (V_{lg})$  curve obtained with ionic liquid. Data from negative gate voltage suggest an EDL capacitance of  $\sim 20 \mu\text{F}/\text{cm}^2$ . However, the positive side is significantly lower. This may be due to the discrepancy in the physical size of the gating ions, which could lead to discrepancies in the geometrical capacitance of the EDL. This could also

explain the slightly higher EDL values observed with double layers formed from the smaller Na<sup>+</sup> ions.

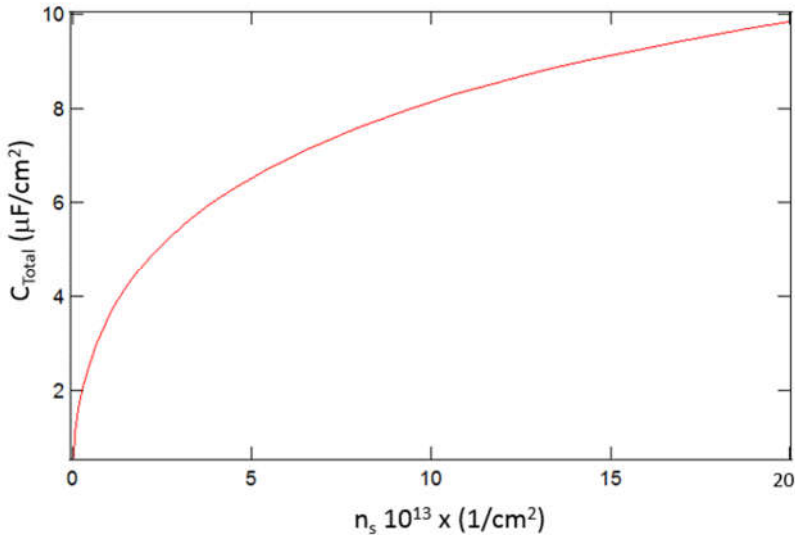


**Figure 5.** Capacitance vs surface carrier density for  $C_{\text{EDL}} = 20 \text{ } \mu\text{F}/\text{cm}^2$ .

Figure 5 shows a graph of  $C_{\text{total}}$  predicted by Eq. 4, if we assume  $C_{\text{EDL}} = 20 \text{ } \mu\text{F}/\text{cm}^2$ . At the maximum carrier density  $C_{\text{total}} \sim 10 \text{ } \mu\text{F}/\text{cm}^2$ . With this capacitance and a porous electrode with accessible surface area of 2,000 m<sup>2</sup>/g a  $C_{\text{Total}}$  of ~200 F/g would be viable. Assuming this is achieved at ~2 V, the energy density would be ~400 J/g, or ~2/3 that of commercial lithium ion batteries.

## 2.6 Conclusion

In conclusion, we have measured the capacitance per unit area of graphene devices submerged in liquid electrolytes commonly used for super capacitors and biosensing applications. This was accomplished by fabricating small graphene EDL capacitors of precisely known surface area and measuring carrier density using Hall effect measurements. The electric double layer

capacitance varies with ion size and does not reach the typically assumed  $20 \mu\text{F}/\text{cm}^2$  typically found with metallic electrodes with typical aqueous electrolytes. For an ionic liquids this value is viable, but depends on the size of the ions forming the double layer. These results suggest an exciting future for graphene super capacitors when gated with novel electrolytes.

## References

1. Winter, M. & Brodd, R. J. What are batteries, fuel cells, and supercapacitors? *Chem. Rev.* **104**, 4245–4269 (2004).
2. Simon, P. & Gogotsi, Y. Materials for electrochemical capacitors. *Nat. Mater.* **7**, 845–854 (2008).
3. Xia, J., Chen, F., Li, J. & Tao, N. Measurement of the quantum capacitance of graphene. *Nat. Nanotechnol.* **4**, 505–9 (2009).
4. Ke, Q. & Wang, J. Graphene-based Materials for Supercapacitor Electrodes - A Review. *J. Mater.* **2**, 37–54 (2016).
5. Cranford, S. W. & Buehler, M. J. Packing efficiency and accessible surface area of crumpled graphene. *Phys. Rev. B - Condens. Matter Mater. Phys.* **84**, (2011).
6. Zhang, L. *et al.* Porous 3D graphene-based bulk materials with exceptional high surface area and excellent conductivity for supercapacitors. *Sci Rep* **3**, 1408 (2013).
7. Stoller, M. D., Park, S., Yanwu, Z., An, J. & Ruoff, R. S. Graphene-Based ultracapacitors. *Nano Lett.* **8**, 3498–3502 (2008).
8. Liberato, S. De *et al.* Laser Scribing of High-Performance. *Science (80-. ).* **335**, 1326–1330 (2012).
9. Hess, L. H., Seifert, M. & Garrido, J. A. Graphene Transistors for Bioelectronics. *Proc. IEEE* **101**, 1780–1792 (2013).
10. Gonnelli, R. S. *et al.* Weak localization in electric-double-layer gated few-layer graphene. *2D Mater.* **4**, 35006 (2017).
11. Sun, S., Qi, Y. & Zhang, T. Y. Dissecting graphene capacitance in electrochemical cell. *Electrochim. Acta* **163**, 296–302 (2015).

12. Ji, H. *et al.* Capacitance of carbon-based electrical double-layer capacitors. *Nat. Commun.* **5**, 3317 (2014).
13. Stoller, M. D. & Ruoff, R. S. Review of Best Practice Methods for Determining an Electrode Material's Performance for Ultracapacitors. 1–14
14. Brown, M. A., Crosser, M. S., Leyden, M. R., Qi, Y. & Minot, E. D. Measurement of high carrier mobility in graphene in an aqueous electrolyte environment. *Appl. Phys. Lett.* **109**, 93104 (2016).
15. Dankerl, M. *et al.* Graphene solution-gated field-effect transistor array for sensing applications. *Adv. Funct. Mater.* **20**, 3117–3124 (2010).
16. Crosser, M. S., Brown, M. a., McEuen, P. L. & Minot, E. D. Determination of the Thermal Noise Limit of Graphene Biotransistors. *Nano Lett.* **15**, 5404–5407 (2015).
17. Ye, J. *et al.* Accessing the transport properties of graphene and its multilayers at high carrier density. *Proc. Natl. Acad. Sci. U. S. A.* **108**, 13002–13006 (2011).
18. Kim, S. M. *et al.* The effect of copper pre-cleaning on graphene synthesis. *Nanotechnology* **24**, 365602 (2013).
19. Zhou, H. *et al.* Chemical vapour deposition growth of large single crystals of monolayer and bilayer graphene. *Nat. Commun.* **4**, 2096 (2013).
20. Brown, M. A., Barker, L., Semprini, L. & Minot, E. D. Graphene Biotransistor Interfaced with a Nitrifying Biofilm. *Environ. Sci. Technol. Lett.* **2**, 118–122 (2015).
21. Xia, J., Chen, F., Li, J. & Tao, N. Measurement of the quantum capacitance of graphene. *Nat. Nanotechnol.* **4**, 505–9 (2009).
22. Adam, S., Hwang, E. H., Galitski, V. M. & Das Sarma, S. A self-consistent theory for graphene transport. *Proc. Natl. Acad. Sci. U. S. A.* **104**, 18392–18397 (2007).

## CHAPTER 3

### **Measurement of high carrier mobility in graphene in an aqueous electrolyte environment**

Morgan A. Brown,<sup>1</sup> Michael S. Crosser,<sup>2</sup> Matthew R. Leyden,<sup>3</sup> Yabing Qi,<sup>3</sup> and Ethan D.

Minot<sup>1,\*</sup>

<sup>1</sup>*Department of Physics, Oregon State University, Corvallis, Oregon 97331, United States*

<sup>2</sup>*Department of Physics, Linfield College, McMinnville, Oregon 97128, United States*

<sup>3</sup>*Energy Materials and Surface Sciences Unit (EMSS), Okinawa Institute of Science and Technology Graduate University (OIST), 1919-1 Tancha, Onna-son, Okinawa 904-0495, Japan*

Applied Physics Letters 109, 093104 (2016)

#### *Abstract*

Graphene is a promising material for applications in aqueous electrolyte environments. To explore the impact of such environments on graphene's electrical properties, we performed Hall bar measurements on electrolyte-gated graphene. Assuming a Drude model, we find that the room temperature carrier mobility reaches  $7,000 \text{ cm}^2/\text{Vs}$ , the highest mobility recorded for graphene in an aqueous electrolyte environment. Our results show that the electrical performance of  $\text{SiO}_2$ -

supported graphene is robust, even in the presence of dissolved ions that introduce additional mechanisms for Coulomb scattering.

Key words: Biotransistor, biosensor, field-effect transistor

### **3.1 Introduction**

Electrolyte-gated graphene is used for electronic biosensing applications,<sup>1</sup> supercapacitor applications,<sup>2</sup> and fundamental measurements of graphene properties at high carrier concentration.<sup>3</sup> The electrolyte environment likely affects the mobility of charge carriers in graphene. Of particular concern is the case of graphene biosensors (typically operated in aqueous electrolyte), for which carrier mobility is critical to device performance.

A significant effort has been made to optimize the carrier mobility in dry graphene devices that are supported by a silicon oxide substrate. Benchmark mobility values for graphene derived from chemical vapor deposition (CVD) are  $\sim 7,000 \text{ cm}^2/\text{Vs}$ ,<sup>4</sup> and slightly higher values are sometimes found with mechanically exfoliated graphene ( $\sim 10,000 \text{ cm}^2/\text{Vs}$ ).<sup>5</sup> When an  $\text{SiO}_2$ -supported graphene device is placed into an aqueous electrolyte, however, we lack clear expectations for the carrier mobility, as the presence of salt ions in the liquid introduces a new mechanism for Coulomb scattering. Previous work related to this question was performed by Newaz et al., who investigated the effect of salted, non-aqueous liquids on the carrier mobility of suspended graphene devices.<sup>6</sup> Additional insight comes from transconductance measurements of graphene field effect transistors (FETs) contacted by two probes and gated by aqueous electrolyte.<sup>7,8,9,10,11</sup> For example, Hess et al. used FET measurements of two-point conductance as a function of liquid gate voltage to estimate the relationship between sheet conductivity,  $\sigma_s$ , and sheet carrier density,  $n_s$ .<sup>11</sup> Surprisingly, there have been no direct measurements of  $\sigma_s$  as a function

of  $n_s$  for graphene gated by an aqueous electrolyte, and therefore no direct measurement of carrier mobility,  $\mu$ , in this system.

Measuring carrier mobility in electrolyte-gated graphene is more challenging than the equivalent measurement of dry, back-gated graphene. First,  $n_s$  is not simply the product of the gate voltage and a constant gate capacitance. The gate capacitance changes with gate voltage due to quantum capacitance effects.<sup>12</sup> Moreover, the double-layer capacitance between the electrolyte-graphene interface has not been well established. Second, if the electrolyte environment contacts the metal electrodes, the electrolyte gate interferes with the voltage measurements that are required to establish  $n_s$  and  $\sigma_s$ .

In this work, we overcome the challenges of measuring carrier mobility in aqueous electrolyte. Graphene electrodes are capped with an insulating layer of SiO<sub>2</sub> to minimize the interference between the electrolyte gate and the voltage measurements. The Hall effect is used to measure sheet carrier density as a function of electrolyte gate voltage. We find a peak carrier mobility greater than 7000 cm<sup>2</sup>/Vs, comparable to the benchmark values for dry graphene on SiO<sub>2</sub>.

### 3.2 Methods

Graphene on copper foil was produced in our chemical vapor deposition system. Copper foil (25  $\mu$ m thickness, Alfa Aesar) was cleaned with dilute nitric acid (5%) followed by acetic acid.<sup>13</sup> The foil was annealed for 60 min in H<sub>2</sub> gas at 1070°C, before starting graphene deposition (30 min at 1070°C, 20 sccm H<sub>2</sub>, 30 sccm CH<sub>4</sub>, pressure 50 Pa).<sup>14</sup> A wet transfer process was used to place the graphene on an Si/SiO<sub>2</sub> substrate (300 nm thermally-grown oxide).<sup>15</sup> The graphene was patterned using a two-layer photolithography process (Shipley S1813 photoresist over a base layer of MicroChem LOR) and O<sub>2</sub> plasma. A second photolithography step was used to create metal electrodes encapsulated by SiO<sub>2</sub> (5 nm Cr, 30 nm Au, 70 nm SiO<sub>2</sub>). The electrode materials

were deposited via e-beam evaporation. After device fabrication the graphene was characterized using microRaman spectroscopy (see supplementary material). Figure 1 shows a completed device, in which  $L = w = 40 \mu\text{m}$ .

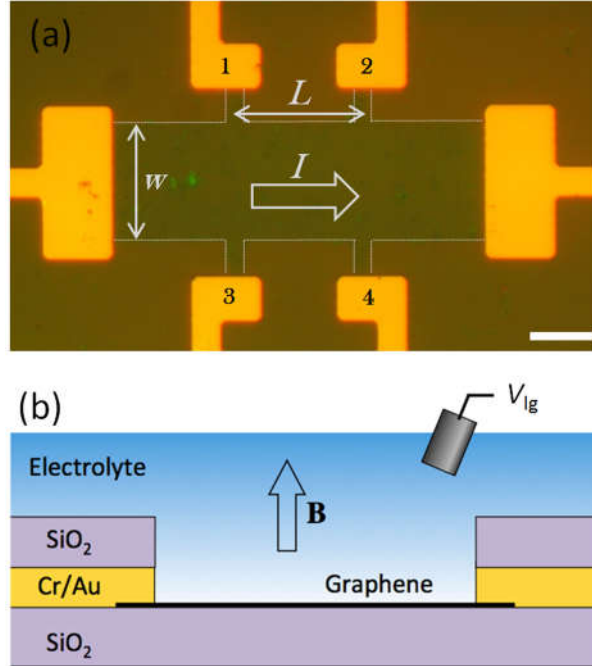


FIG. 1. Device geometry. (a) Hall bar geometry with constant current applied as indicated. Dashed white lines show the edge of the patterned graphene. The numbered electrodes are used to measure voltage differences; for example,  $V_{13}$  is the voltage difference between electrodes 1 and 3. Scale bar 20  $\mu\text{m}$ . (b) Cross-sectional diagram of the device. The  $\text{Cr}/\text{Au}$  contacts are capped in  $\text{SiO}_2$ . The magnetic field is perpendicular to the graphene.

All experiments were performed with the graphene device submerged in an NaCl aqueous solution (100 mM) with phosphate buffer (10 mM) to stabilize the pH at 7.2. The electrostatic potential of the liquid gate,  $V_{\text{lg}}$ , was controlled using a tungsten wire immersed in the electrolyte (see Fig. S2 in the Supporting Information). A current source (Keithley 2400 Source meter) was used to supply a dc current,  $I = 5 \mu\text{A}$ . The magnetic field,  $B$ , was applied perpendicular to the

graphene using a variable-field electromagnet (+/- 0.5 T). Gate voltage sweeps were performed at a rate of 10 mV/s.

Figure 2 shows the Hall voltage,  $V_H$ , measured when  $B = \pm 0.5$  T. The measurement procedure is as follows. First,  $V_{13}$  is measured at  $B = 0$  to establish the gate-dependent background voltage. This background voltage (of the order 0.1 mV) is related to the spatial inhomogeneity in the electrolyte gate potential. Next,  $V_{13}$  is measured at  $B = \pm 0.5$  T. The Hall voltage is then  $V_H = V_{13}(B = \pm 0.5 \text{ T}) - V_{13}(B = 0)$ .

When  $B > 0$  (red line),  $V_H$  is positive for hole-type transport and negative for electron transport. When  $B < 0$  (black), the sign of  $V_H$  reverses. The transition from hole transport to electron transport occurs at the Dirac point,  $V_D \sim 0.03$  V with respect to the tungsten electrode.

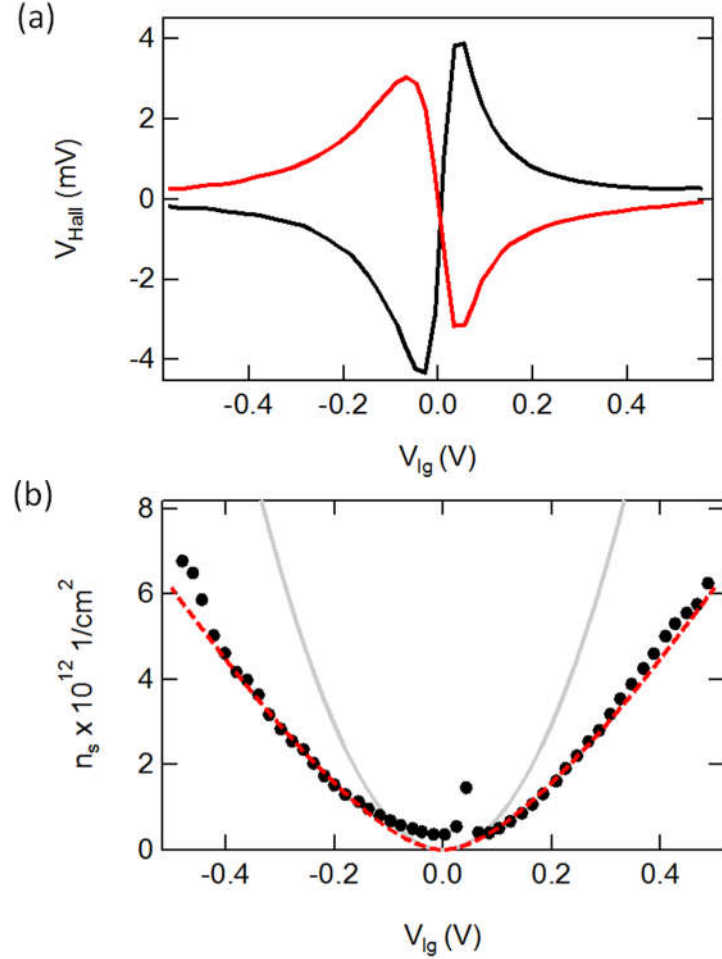


FIG. 2. Hall-effect measurements of electrolyte-gated graphene. The aqueous electrolyte is 100 mM NaCl. (a) The Hall voltage,  $V_H$ , measured when  $B = \pm 0.5$  T. The raw  $V_{13}$  data (not shown) includes a gate-dependent background ( $\sim 0.1$  mV) that has been subtracted. b) Black dots represent the sheet carrier density,  $n_s$ , determined from  $V_H$  (Eq. 1). The grey line represents the calculated density when  $C_{dl} \gg C_q$  (the quantum capacitance limit). The red dashed line is calculated from Eq. 3 with  $C_{dl} = 5 \mu\text{F/cm}^2$ .

### 3.3 Results and Discussion

The sheet carrier density is inversely proportional to the Hall voltage,

$$n_s = \frac{BI}{V_H e}. \quad (1)$$

We calculate  $n_s$  as a function of  $V_g$  using Eq. 1 (Fig 2b, black dots).

To understand the relationship between  $n_s$  and  $V_{lg}$  (Fig. 2b), we consider both the graphene density of states and the double-layer capacitance between the electrolyte gate and carriers in the graphene,  $C_{dl}$ . Assuming a tight binding model for the graphene dispersion relation,  $n_s$  scales as  $E_F^2$ , where  $E_F$  is the Fermi energy measured relative to the Dirac point.

$$n_s = \frac{1}{\pi} \left( \frac{E_F}{\hbar v_F} \right)^2, \quad (2)$$

where the Fermi velocity is  $v_F \sim 10^6 \text{ ms}^{-1}$ , and  $\hbar$  is the reduced Plank constant. The quantum capacitance of graphene,  $C_q = e^2(dn_s/dE_F)$ , approaches zero as  $E_F$  approaches zero. If  $C_{dl} \gg C_q$ ,  $C_q$  limits  $n_s$  such that  $n_s \approx (10^{14} \text{ cm}^{-2}\text{V}^{-2}) \cdot V_{lg}^2$  (grey line on Fig. 2b.).

To account for  $C_{dl}$ , we model the system as two capacitors in series. The sheet charge density on  $C_{dl}$  and  $C_q$  is equal, and the voltage across each capacitor adds to  $V_{lg}$ .  $n_s$  is found by solving

$$V_{lg} = \frac{\hbar v_F \sqrt{\pi n_s}}{e} + \frac{en_s}{C_{dl}}. \quad (3)$$

Equation 3 fits our experimental data when  $C_{dl} = 5 \mu\text{F/cm}^2$  (red dashed line). The value of  $C_{dl}$  that we determine from fitting our measurements is consistent with a model developed by Dankerl et al. for the spatial charge and electrostatic potential distributions at a graphene/electrolyte interface.<sup>16</sup> The measured  $n_s$  values deviate from eq. 3 at small  $V_{lg}$ . In this low-doping regime,  $n_s$  is dominated by electrostatic disorder in the graphene. We find a disorder-induced carrier concentration,  $n_{s,\text{disorder}} \sim 0.4 \times 10^{12} \text{ cm}^{-2}$ , which is typical for SiO<sub>2</sub>-supported graphene.<sup>17</sup>

After establishing  $n_s(V_{lg})$ , we turn to the sheet conductivity,  $\sigma_s(V_{lg})$ . Figure 3a shows the sheet conductivity,  $\sigma_s = I/V_{12}$ , which is calculated from the voltage drop  $V_{12}$  (see Fig. 1). The sheet conductivity is smallest at the Dirac point,  $V_D$ , and increases almost linearly with  $|V_{lg} - V_D|$ . The linearity of  $\sigma_s(V_{lg})$  is described well by a Boltzmann transport model (red dashed line), as discussed further below. The transconductance,  $d\sigma_s/dV_{lg}$ , is a useful figure of merit for biosensor sensitivity. We observe a peak transconductance of 4.5 mS/V. This is higher than previous reports for graphene in an aqueous environment, and is indicative of high mobility.

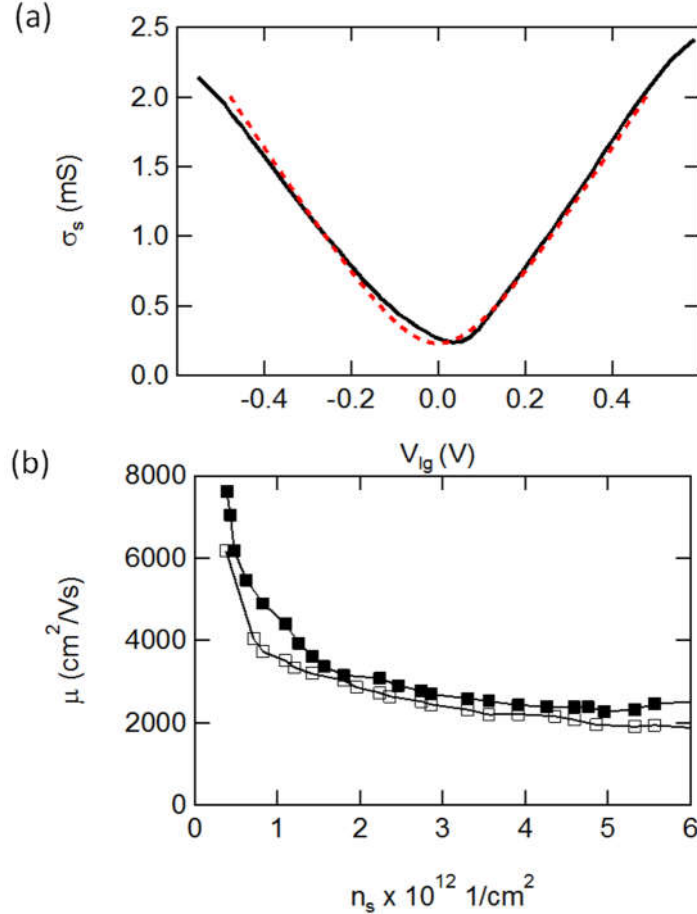


FIG. 3 Sheet conductivity and mobility measurements of electrolyte-gated graphene. The aqueous electrolyte is 100 mM NaCl. (a) The sheet conductivity as a function of  $V_{lg}$  (black line). Theoretical curve (dashed red line) based on Boltzmann transport theory with  $\tau v_F = 70$  nm. (b) The Drude carrier mobility for electrons (solid squares) and holes (open squares).

The commonly-used framework for interpreting  $\sigma_s$  is the Drude model:  $\sigma_s = \mu e n_s$ , where  $\mu$  is the Drude mobility. Figure 3b shows the calculated  $\mu$  values for electrons and holes based on the measurements of  $n_s$  and  $\sigma_s$ . The maximum mobility exceeds 7,000  $\text{cm}^2/\text{Vs}$ , matching the typical benchmark for dry GFET devices on  $\text{SiO}_2$  substrates.

Our measurements of  $\sigma_s$  and  $\mu$  (Fig. 3) give insight into the effect of aqueous electrolyte on graphene's electronic properties. The mobility-limiting factor in graphene is thought to be Coulomb scattering caused by charged impurities.<sup>18</sup> There are at least two roles that aqueous electrolyte could play in Coulomb scattering. First, dissolved ions could act as charged impurities, thereby decreasing  $\mu$ . Second, the dielectric constant of the water may screen charged impurities, thereby increasing  $\mu$ . The effectiveness of dielectric screening would depend on the location of the charged impurities. For example, dielectric liquid above the graphene cannot effectively screen charge traps located in the SiO<sub>2</sub> underneath the graphene.

We tested the possibility that dissolved ions reduce  $\mu$  by measuring  $\mu$  in a variety of salt concentrations. Figure S3 (Supporting Information) shows that  $\mu$  is unchanged by varying salt concentration from 1 mM to 100 mM. To explore the second possibility (dielectric screening increases  $\mu$ ), we compare our measurements to previous work on dry, SiO<sub>2</sub>-supported CVD graphene in which  $\mu \sim 7,000$  cm<sup>2</sup>/Vs.<sup>4</sup> Since we find a similar  $\mu$  for our water-gated, SiO<sub>2</sub>-supported graphene, we postulate that charge traps buried in the SiO<sub>2</sub> substrate are likely the limiting factor in both a dry environment and an aqueous electrolyte environment.

A recent experiment by Newaz et al.<sup>6</sup> corroborates our claim that the SiO<sub>2</sub> substrate has much greater effect on  $\mu$  than the salt ions in the aqueous electrolyte. Newaz et al. investigated the effect of submerging suspended graphene devices in a non-aqueous solution (anisole) with dissolved salt (tetrabutylammonium tetraphenylborate). In a low-salt solution, mobility was enhanced due to the dielectric screening properties of anisole. Increasing the salt concentration from 0.01 mM to 100 mM reduced  $\mu$  from 50,000 cm<sup>2</sup>/Vs to 20,000 cm<sup>2</sup>/Vs. A mobility of 20,000 cm<sup>2</sup>/Vs is significantly higher than  $\mu$  in SiO<sub>2</sub>-supported graphene. Therefore, Newaz's result

suggests that our measurement of  $\mu \sim 7,000 \text{ cm}^2/\text{Vs}$  is more likely attributable to the SiO<sub>2</sub> substrate than to dissolved salt ions.

Figure 3a includes a fitting curve based on Boltzmann transport theory. Unlike the Drude model, the Boltzmann transport model accounts for the Pauli-exclusion principle and the distribution of electrons in k-space. For a 2d material with relativistic dispersion, Boltzmann transport theory predicts,<sup>18</sup>

$$\sigma_s = \frac{2e^2}{h} \tau v_F \sqrt{\pi n_s}, \quad (4)$$

where  $\tau$  is the energy-averaged carrier scattering time. Combining equations 3 and 4 yields a good fit to the measured data when  $\tau v_F = 70 \pm 5 \text{ nm}$  (dashed line Figure 3a).

It is interesting that Boltzmann transport describes the sheet conductivity with a single fit parameter,  $\tau v_F$ , in contrast to the Drude model, which is fit by allowing  $\mu$  to change as a function of  $n_s$ . Previous reports of graphene's electronic properties have favored the Drude model over the Boltzmann transport model (eq. 4), perhaps because  $\tau$  varies with  $n_s$  for dry graphene devices.<sup>19</sup> However, it appears that  $\tau$  is insensitive to  $n_s$  when screening is provided by a dielectric fluid. In future work, it will be interesting to explore the application of the Boltzmann transport theory for electrolyte-gated graphene.

### **3.4 Conclusion**

In conclusion, we have measured the carrier mobility for graphene submerged in an aqueous electrolyte. The measured room-temperature mobility is significantly higher than traditional semiconductors such as silicon, and is comparable to benchmark values reported for dry graphene on SiO<sub>2</sub> substrates. This is the first time that the robustness of graphene's superb

electrical properties has been demonstrated in an aqueous electrolyte environment. Future experiments on suspended graphene, or graphene on hexagonal boron nitride, may demonstrate even higher mobilities in aqueous electrolyte. Graphene's high carrier mobility in aqueous electrolytes, together with mechanical strength/flexibility, chemical stability, and biocompatibility, suggests an exciting future for graphene biosensor applications.

### ***3.5 Supporting Information***

Characterization of graphene quality. Chip carrier design and the liquid-gate electrode.

Relationship between salt concentration and graphene carrier mobility.

### **Acknowledgements**

Funding for this research was provided by the National Science Foundation under award number DBI-1450967. M.R.L. and Y.B.Q. would like to thank funding from the Energy Materials and Surface Sciences Unit of the Okinawa Institute of Science and Technology Graduate University to support the synthesis of graphene samples, which was performed at OIST. We thank Michael Reynolds and Paul McEuen for valuable discussions. Device fabrication was performed at the MaSC Facility at Oregon State University.

# Supporting Information for

## Measurement of high carrier mobility in water-gated graphene

Morgan A. Brown,<sup>1</sup> Michael S. Crosser,<sup>2</sup> Matthew R. Leyden,<sup>3</sup> Yabing Qi,<sup>3</sup> and Ethan D. Minot<sup>1,\*</sup>

<sup>1</sup>*Department of Physics, Oregon State University, Corvallis, Oregon 97331, United States*

<sup>2</sup>*Department of Physics, Linfield College, McMinnville, Oregon 97128, United States*

<sup>3</sup>*Energy Materials and Surface Sciences Unit (EMSS), Okinawa Institute of Science and Technology Graduate University (OIST), 1919-1 Tancha, Onna-son, Okinawa 904-0495, Japan*

\*Corresponding author email address: [ethan.minot@oregonstate.edu](mailto:ethan.minot@oregonstate.edu)

### 1. Characterization of graphene quality

After fabrication of the graphene Hall bar device, the microRaman spectrum was obtained from multiple locations on the graphene. The laser wavelength was 532 nm and the spot size was  $\sim 1 \mu\text{m}$ . Figure S1 shows a characteristic spectrum. The ratio of the 2D peak to G peak intensity is  $\sim 3$ , confirming single layer graphene.<sup>1</sup> The D peak to G peak ratio is 0.04 indicating low defect density.<sup>1</sup>

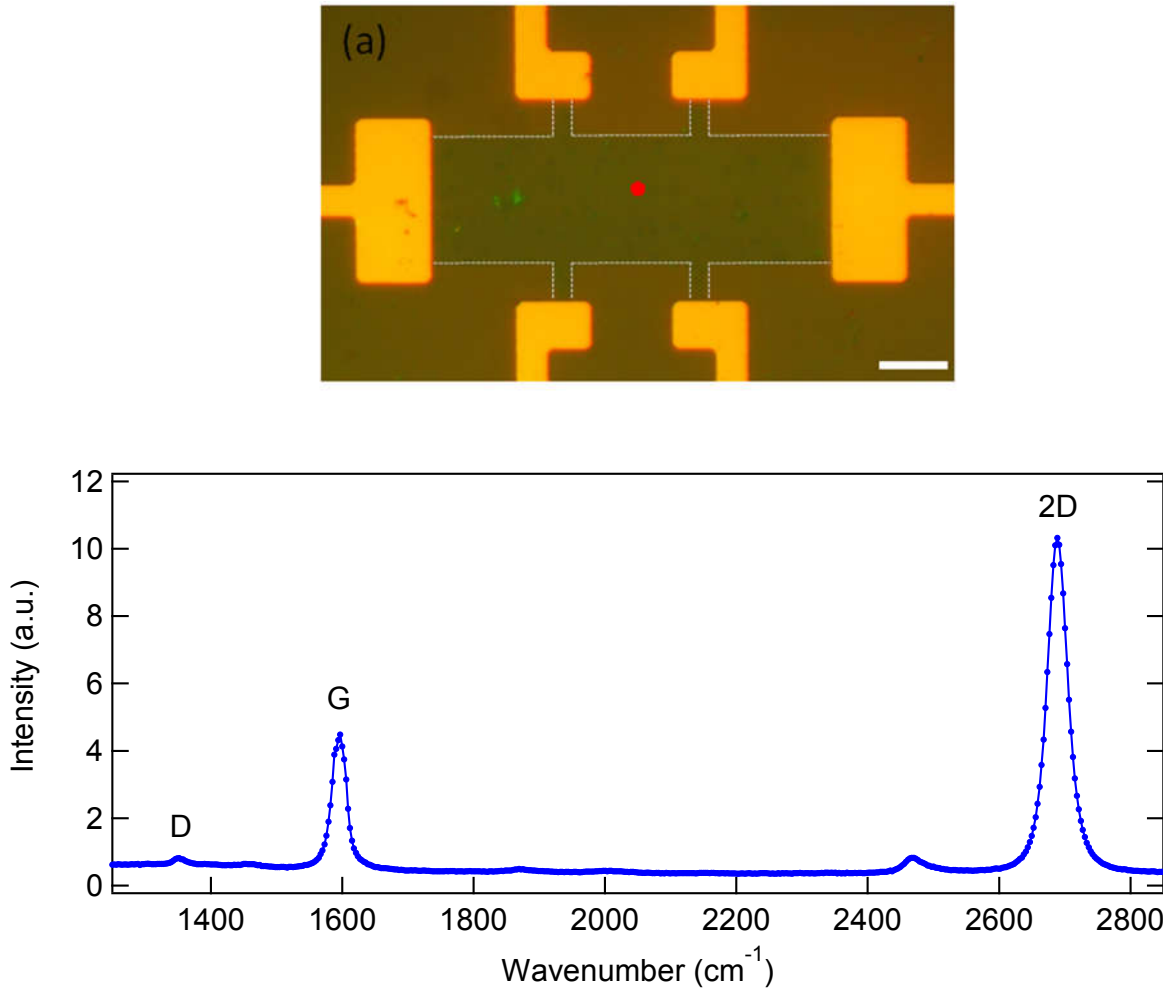


FIG. S1 (a) Microscope image of the graphene device with the position of the Raman laser spot indicated in red. Scale bar 20  $\mu\text{m}$ . (b) MicroRaman spectrum obtained from the graphene device.

Another indicator of high quality graphene is the sheet resistance directly after transfer from copper foil to an  $\text{SiO}_2$  substrate. After a standard transfer procedure, we measured the sheet resistance of the dry graphene (resistance of one square) to be 1000 – 1100  $\Omega$ . This sheet resistance drops to 500  $\Omega$  ( $\sigma_s = 2 \text{ mS}$ ) when the electrolyte gate is used to reach a sheet charge density of  $n_s = 6 \times 10^{12} \text{ cm}^{-2}$  (see Fig. 3 in the main text).

## 2. Chip carrier design and the liquid-gate electrode

The graphene Hall bar device lies on top of a Si/SiO<sub>2</sub> substrate (purple color in Fig. S2). The substrate dimensions are 2.5 cm x 2.5 cm. This Si/SiO<sub>2</sub> substrate is attached to a custom-designed printed circuit board (green color in Fig. S2) using double-sided tape. Electrical connection between the graphene device and printed circuit board is achieved by wire bonding. The printed circuit board is interfaced to electrical instrumentation via a ribbon cable. A droplet of saline water, with height approximately 5 mm and diameter approximately 10 mm is balanced on the chip, centered on the graphene Hall bar device. The liquid gate voltage,  $V_{lg}$ , is applied via a tungsten wire that is inserted into the droplet of saline water. The wire is positioned above the Hall bar device.

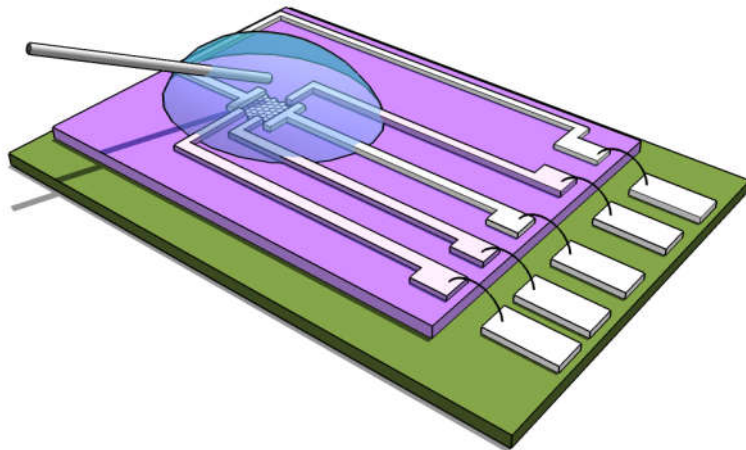


FIG. S2. Schematic drawing (not drawn to scale) showing the printed circuit board (green) that carries the Si/SiO<sub>2</sub> chip (purple). A droplet of saline water is balanced on the chip. The liquid gate voltage is applied to the saline water via a tungsten wire. The drawing shows only the tip of the tungsten wire.

### 3. Relationship between salt concentration and graphene carrier mobility

We measured Hall mobility in a second graphene device that was submerged in various salt water solutions. Figure S3 shows mobility as a function of sheet carrier density with salt concentration of 1 mM, 10 mM and 100 mM. The curves are indistinguishable within experimental uncertainty. We conclude that salt ions are not the mobility-limiting factor for SiO<sub>2</sub>-supported graphene devices submerged in aqueous electrolyte.

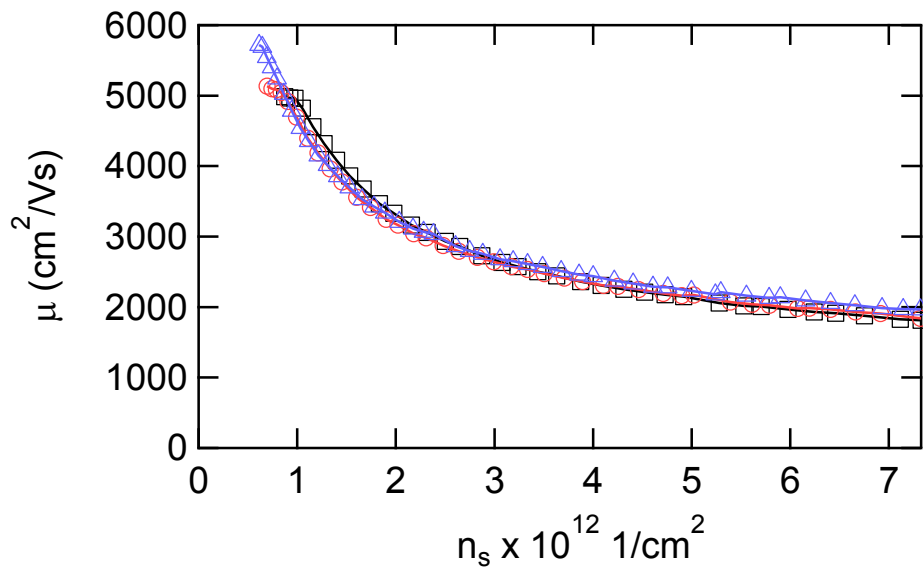


FIG. S3. Mobility as a function of sheet carrier density (n-type transport) when a graphene Hall bar device is submerged in three different solutions: 1 mM NaCl (triangle symbols), 10 mM NaCl (circle symbols) and 100 mM NaCl (square symbols).

Bibliography:

<sup>1</sup> A.C. Ferrari and D.M. Basko, Nat. Nanotechnol. **8**, 235 (2013).

**3.6 Bibliography:**

- <sup>1</sup> Y. Liu, X. Dong, and P. Chen, Chem. Soc. Rev. **41**, 2283 (2012).
- <sup>2</sup> K.S. Novoselov, V.I. Fal'ko, L. Colombo, P.R. Gellert, M.G. Schwab, and K. Kim, Nature **490**, 192 (2012).
- <sup>3</sup> J. Ye, M.F. Craciun, M. Koshino, S. Russo, S. Inoue, H. Yuan, H. Shimotani, A.F. Morpurgo, and Y. Iwasa, Proc. Natl. Acad. Sci. U. S. A. **108**, 13002 (2011).
- <sup>4</sup> J. Chan, A. Venugopal, A. Pirkle, S. McDonnell, D. Hinojos, C.W. Magnuson, R.S. Ruoff, L. Colombo, R.M. Wallace, and E. Vogel, ACS Nano **6**, 3224 (2012).
- <sup>5</sup> L.A. Ponomarenko, R. Yang, T.M. Mohiuddin, M.I. Katsnelson, K.S. Novoselov, S. V. Morozov, A.A. Zhukov, F. Schedin, E.W. Hill, and A.K. Geim, Phys. Rev. Lett. **102**, 100 (2009).
- <sup>6</sup> A.K.M. Newaz, Y.S. Puzyrev, B. Wang, S.T. Pantelides, and K.I. Bolotin, Nat. Commun. **3**, 734 (2012).
- <sup>7</sup> G. Saltzgaber, P. Wojcik, T. Sharf, M.R. Leyden, J.L. Wardini, C.A. Heist, A.A. Adenuga, V.T. Remcho, and E.D. Minot, Nanotechnology **24**, 355502 (2013).
- <sup>8</sup> Z. Cheng, Q. Li, Z. Li, Q. Zhou, and Y. Fang, Nano Lett. **10**, 1864 (2010).
- <sup>9</sup> I. Heller, S. Chattoor, J. Männik, M.A.G. Zevenbergen, C. Dekker, and S.G. Lemay, J. Am. Chem. Soc. **132**, 17149 (2010).
- <sup>10</sup> Y. Ohno, K. Maehashi, Y. Yamashiro, and K. Matsumoto, Nano Lett. **9**, 3318 (2009).
- <sup>11</sup> L.H. Hess, M. V. Hauf, M. Seifert, F. Speck, T. Seyller, M. Stutzmann, I.D. Sharp, and J.A. Garrido, Appl. Phys. Lett. **99**, 033503 (2011).

<sup>12</sup> J. Xia, F. Chen, J. Li, and N. Tao, *Nat. Nanotechnol.* **4**, 505 (2009).

<sup>13</sup> S.M. Kim, A. Hsu, Y.-H. Lee, M. Dresselhaus, T. Palacios, K.K. Kim, and J. Kong, *Nanotechnology* **24**, 365602 (2013).

<sup>14</sup> H. Zhou, W.J. Yu, L. Liu, R. Cheng, Y. Chen, X. Huang, Y. Liu, Y. Wang, Y. Huang, and X. Duan, *Nat. Commun.* **4**, 2096 (2013).

<sup>15</sup> M.A. Brown, L. Barker, L. Semprini, and E.D. Minot, *Environ. Sci. Technol. Lett.* **2**, 118 (2015).

<sup>16</sup> M. Dankerl, M. V. Hauf, A. Lippert, L.H. Hess, S. Birner, I.D. Sharp, A. Mahmood, P. Mallet, J.Y. Veuillen, M. Stutzmann, and J.A. Garrido, *Adv. Funct. Mater.* **20**, 3117 (2010).

<sup>17</sup> S. Adam, E.H. Hwang, V.M. Galitski, and S. Das Sarma, *Proc. Natl. Acad. Sci. U. S. A.* **104**, 18392 (2007).

<sup>18</sup> S. Das Sarma, S. Adam, E.H. Hwang, and E. Rossi, *Rev. Mod. Phys.* **83**, 407 (2011).

<sup>19</sup> E. Hwang, S. Adam, and S. Sarma, *Phys. Rev. Lett.* **98**, 186806 (2007).

## CHAPTER 4

### **Graphene Biotransistor Interfaced with a Nitrifying Biofilm**

Morgan Brown<sup>1</sup>, Leila Barker<sup>2</sup>, Lewis Semprini<sup>2</sup> and Ethan D. Minot<sup>1</sup>

<sup>1</sup>*Department of Physics, Oregon State University*

<sup>2</sup>*School of Chemical, Biological and Environmental Engineering, Oregon State University*

Published in : Environmental Science and Technology Letters (2015) DOI: 10.1021

#### *Abstract*

Using a graphene field-effect transistor biosensor, we monitored the pH inside a living biofilm with fast temporal resolution ( $\sim 1$  s) over multi-hour time periods. The atomically-thin sensing surface is positioned directly beneath the biofilm, providing non-invasive access to conditions deep within the biofilm. We determine the transient changes in pH at the biofilm-surface interface when the biofilm metabolizes substrate molecules and when it is exposed to biocide. Our results demonstrate the potential of this technology to monitor diffusion kinetics inside biofilms and to monitor biofilm health.

#### 4.1 Introduction

Quantitative tools to monitor living biofilms are important in fields ranging from medicine to environmental monitoring. In applications such as wastewater treatment, biofilm reactor systems are typically monitored using bulk fluid measurements.<sup>1</sup> This technique is powerful, because a range of traditional chemical assays are available and measurements are directly linked to process performance. However, it is well known that understanding the kinetics of growth and substrate utilization within a biofilm is essential for optimizing fixed-film processes.<sup>2</sup> Recent advances in microelectronic devices offer exciting new possibilities to monitor biofilm activity in real time at multiple points inside the film. The goal of this study is to explore the suitability of field-effect transistor (FET) biosensors for monitoring the metabolic activity of a biofilm.

We use graphene, an atomically-thin sheet of sp<sup>2</sup>-bonded carbon atoms, as the active material for our FET biosensor. Subtle changes in the electrostatic environment result in significant changes in graphene's sheet resistance.<sup>3</sup> Graphene is remarkably biocompatible, as shown by recent tests with *Escherichia coli*<sup>4</sup> and neural cells.<sup>5</sup> While graphene FET (GFET) biosensors are being pursued by a number of research groups, only a fraction of these studies focus on using GFETs to study bacteria. These previous studies of bacteria are limited to investigating the metabolic activity of *E. coli* during the early stages of surface attachment.<sup>3</sup> There are no previous reports of biofilms studied via graphene FET biosensors.

The biofilm used for this work is formed by an ammonia oxidizing bacterium (AOB), *Nitrosomonas europaea*. AOB play a critical role in the global nitrogen cycle and in the removal of nitrogen during wastewater treatment.<sup>6,7</sup> Since AOB are slow growing, biofilm-based processes

are particularly important. In the biofilm form, AOB exhibit higher nutrient removal rates and higher resistance to washout when compared to planktonic bacteria.<sup>8</sup> Techniques to monitor the health of AOB biofilms are desired, because AOB are considered to be some of the most sensitive microorganisms found in wastewater treatment plants.<sup>9</sup>

#### **4.2 Methods**

The GFET was fabricated using a standard process based on graphene grown via chemical vapor deposition.<sup>10,11</sup> To limit the contact between liquids and the electrical connections, the electrode traces were covered by 70 nm of SiO<sub>2</sub> and wires were sealed with silicone. These steps ensured that Faradaic currents were 3 orders of magnitude smaller than the source drain current ( $I_{sd}$ ). The electrode geometry is shown in Figure 1. The GFET was biased with a constant source-drain voltage  $V_{sd} = 25$  mV for all experiments.

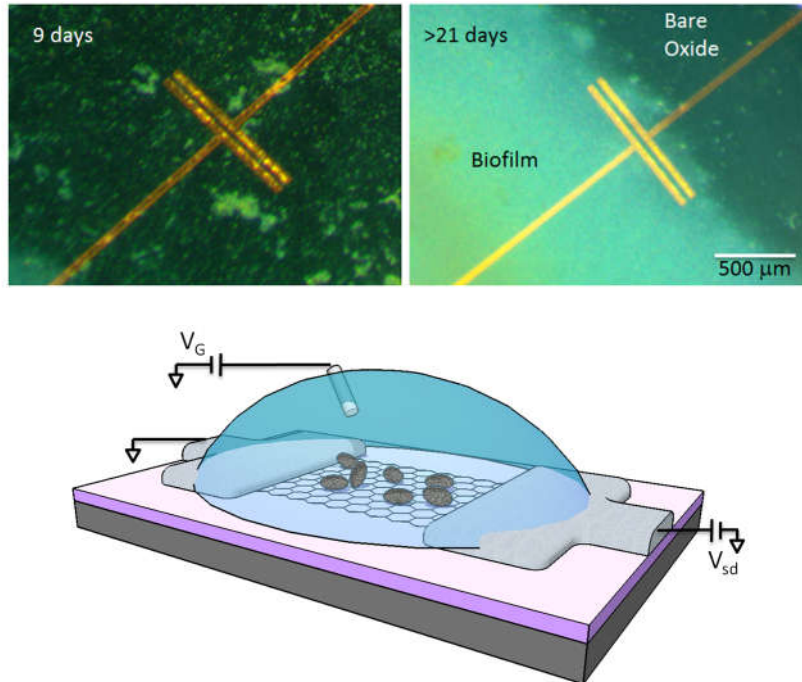


**Figure 1.** (a) Optical micrograph, 9 days growth, showing initial pillar formation. (b) Optical micrograph, >21 days growth, showing the presence of a mature biofilm covering the GFET. The graphene sheet connecting the metal electrodes has an area of 40  $\mu\text{m} \times 1 \text{ mm}$ . (c) Schematic diagram of the electrical measurement.

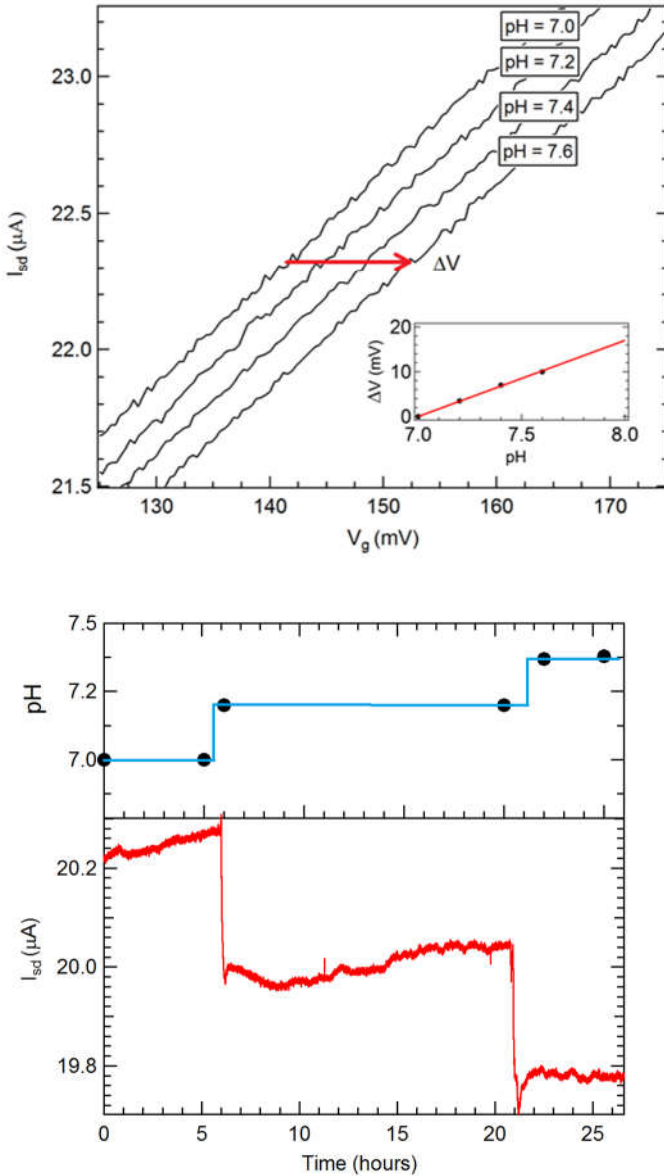


**Figure 2.** (a)  $I-V_g$  curves for various pH values without a biofilm where  $\Delta V$  quantifies the rightward shift of the  $I-V_g$  curve caused by increasing pH. (b) Following biofilm attachment, the change in  $I_{sd}$  that accompanies a change in pH was noted in order to establish the conversion factor between  $I_{sd}$  and pH at  $V_g = 150$  mV.

Prior to biofilm growth, we characterized the sensitivity of the bare GFET to pH. The device was operated with  $V_g$  in the range 100 – 250 mV where the slope  $dI_{sd}/dV_g = 39 \mu\text{A/V}$  (Fig. 2). Changing the pH by one unit was equivalent to a change in gate voltage of  $\Delta V = 17 \text{ mV}$ . Similar pH sensitivities have been observed by other authors.<sup>12</sup> For small shifts in pH, the sensor can be operated at fixed  $V_g$  and fixed  $V_{sd} = 25 \text{ mV}$ , in which case we find a sensitivity of  $0.66 \mu\text{A/pH}$ .

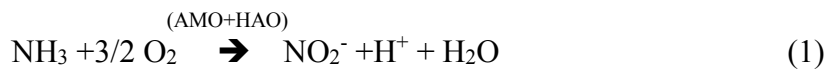
*N. europaea* biofilms were grown directly on the surface of the GFET device. The GFET was submersed in a bath of HEPES buffer (30 mM) with trace nutrients for growth, as described by Lauchnor et al.<sup>13</sup> The volume of liquid was maintained at approximately 60 mL in a standard petri dish. The GFET remained in this bath for the duration of the experiments. The *N. europaea* cells (ATCC strain 19718) used to inoculate the GFET surface were grown in batch, concentrated, and the cells and growth media, including biomolecules, were added to the petri dish.

The initial bacterial attachment phase lasted ~ 8 hours, during which bacteria, protein, and polysaccharides floating in solution gradually attached to the surface of the GFET. During this 8 hour period we observed changes in the  $I_{sd}(V_g)$  curve equivalent to  $\Delta V = 60 \text{ mV}$  (Figure S2). It is likely that  $\Delta V$  is caused by the absorption of bacteria and biomolecules on the graphene surface.<sup>14</sup>

After the initial bacterial attachment, the position of the  $I_{sd}(V_g)$  curve became stable ( $d\Delta V/dt \sim +/- 0.2 \text{ mV/hour}$ ) and the device exhibited greater pH sensitivity (Fig. 2b). Changing pH by one unit was equivalent to  $\Delta V = 32 \text{ mV}$ , or equivalently,  $1.4 \mu\text{A/pH}$ . The increased pH sensitivity of the GFET sensor is likely due to an increased density of ionizable groups on the graphene surface.<sup>15,16</sup> The presence of adsorbed molecules on the graphene surface also had a small effect (~ 10%) on the slope  $dI_{sd}/dV_g$ .

Optical micrographs were taken to determine biofilm development on the GFET. These images show pillar formation, followed by the development of mature biofilms in a timeframe of approximately 2.5 weeks (see Fig. 1a and b). Similar timescales for *N. europaea* biofilm development were observed by Lauchnor et al.<sup>13</sup> To confirm that the biofilm was indeed an AOB, rather than an unwanted bacterium, we used traditional methods to monitor the nitrite and pH levels of the bulk fluid over four days (Figure S3). We observed a continuous increase in nitrite levels and decrease in pH, consistent with the activity of an AOB and consistent with *N. europaea* batch tests at a similar buffer capacity.<sup>17</sup>

While establishing the biofilm, the medium was exchanged regularly to replace nutrients and buffer and to remove bacteria suspended in solution. After a mature biofilm was established, roughly 3 weeks, the GFET was used to monitor biofilm activity with high spatial and temporal resolution. We first studied the response of the system to ammonia ( $\text{NH}_3$ ). *N. europaea* is known to convert  $\text{NH}_3$  to  $\text{NH}_2\text{OH}$  and then  $\text{NO}_2^-$  in a two-step process. The enzyme ammonia monooxygenase (AMO) catalyzes the first step, and hydroxylamine oxidoreductase (HAO) catalyzes the second step.



The balanced reaction for  $\text{NH}_3$  oxidation to  $\text{NO}_2^-$ , (equation 1) shows that one  $\text{H}^+$  is released per  $\text{NH}_3$  molecule oxidized. The net result is a more acidic environment; therefore, the consumption of  $\text{NH}_3$  by *N. europaea* is well suited to monitoring via the pH sensitive GFET.

Prior to making a GFET measurement, the media was exchanged for one with a lower buffer capacity (6 mM HEPES).<sup>17</sup> Low buffer capacity optimized pH sensitivity and the fresh media ensured that subsequent nitrification activity was associated with the biofilm rather than

suspended bacteria. Biofilm activity was then initiated by introducing  $(\text{NH}_4)_2\text{SO}_4$  into the 60 mL volume of buffer solution to produce an  $\text{NH}_4^+$  concentration of  $\sim 1 \text{ mM}$ . The  $(\text{NH}_4)_2\text{SO}_4$  aliquot was added slowly to the bulk fluid, taking care to avoid mechanical disturbance to the biofilm. At pH 7.8, only a fraction of  $\text{NH}_4^+$  ions are present in the biologically-available  $\text{NH}_3$  form ( $\sim 30 \mu\text{M}$ ). This concentration is approximately half the saturation coefficient ( $K_s$ ) for  $\text{NH}_3$  for *N. europaea*.<sup>18</sup> Decreases in pH during the experiment will decrease the availability of  $\text{NH}_3$ .

#### 4.3 Results and Discussion

The green trace in Figure 3 shows the typical sensor response. After introduction of  $\text{NH}_3$ , the sensor reports a gradual decrease in pH, followed by a slight rise to a stable value. To check the accuracy of the pH values reported by the GFET sensor, we also measured the pH of the bulk fluid before and after adding  $\text{NH}_3$  (black crosses on Fig. 3). The curve and crosses agree within the average drift of the GFET sensor. Nitrite levels in the bulk fluid were also checked at  $t = 18$  and 80 min. Nitrite concentration increased from 3.04 to 3.46 mM. Of the 1.0 mM  $\text{NH}_4^+$  added, only 0.4 mM was converted to  $\text{NO}_2^-$ .

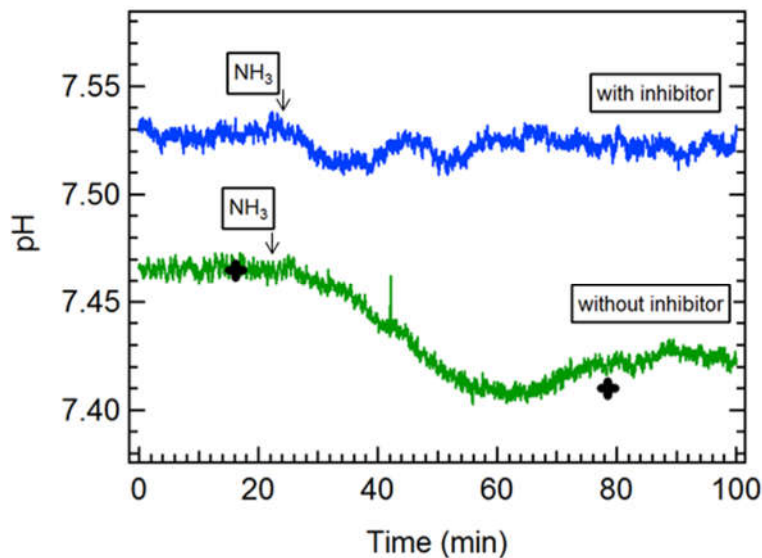


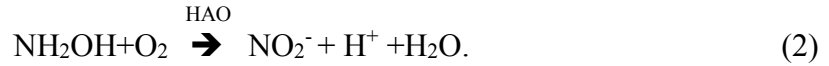
**Figure 3.** Changing pH inside the biofilm measured by the GFET sensor. A dose of NH<sub>3</sub> was added at  $t = 21$  minutes. The blue curve was measured after the AMO enzyme was inhibited by ATU. The green curve was measured with no inhibitor. The black crosses correspond to measurements of the bulk pH.

We interpret the green curve as follows: at  $t = 0$  (in the absence of NH<sub>3</sub>) we assume that dissolved oxygen (DO) is present throughout the biofilm, as observed by Lauchnor et al.<sup>17</sup> After the addition of NH<sub>3</sub> there is lag time while NH<sub>3</sub> mixes/diffuses throughout the liquid. NH<sub>3</sub> consumption in the biofilm starts at  $t \sim 25$  minutes as H<sup>+</sup> ions are generated and the local pH decreases. At  $t = 60$  minutes, the supply of DO is diminished and the biofilm generates H<sup>+</sup> ions at a slower rate. As H<sup>+</sup> ions diffuse towards the bulk liquid and buffer diffuses into the biofilm, the pH inside the biofilm begins to rise. At  $t = 90$  minutes, NH<sub>3</sub> utilization becomes oxygen limited and the pH inside the biofilm approaches the pH of the bulk fluid. The overall rate of NO<sub>2</sub><sup>-</sup> formation is consistent with the observations of Lauchnor and Semprini for biofilms of *N. europaea* under conditions of oxygen limitation.<sup>19</sup>

Our interpretation of Fig. 3 assumes that the equilibration of the biofilm with the bulk fluid occurs on times scale of tens of minutes. We estimated the relevant equilibration times using methods described by Stewart<sup>20</sup> (see Supporting Information). For an assumed biofilm thickness of 0.1 cm we estimate  $t_{90} = 8$  minutes for NH<sub>3</sub> and 2 minutes for H<sup>+</sup>, where  $t_{90}$  is the time to reach 90 % of the bulk fluid concentration. The equilibration times will be further lengthened by the boundary layer between the biofilm and the bulk fluid. We conclude that the time scales shown in Figure 3 are reasonable.

To check that the pH change shown in Fig. 3 is due to biofilm activity, we inhibited the biofilm's ability to consume NH<sub>3</sub>. Allylthiourea (ATU) is known to completely inhibit nitrification of *N. europaea* biofilms by inhibiting the activity of the AMO enzyme.<sup>17,21</sup> The blue curve in Fig. 3 shows the response of the system after exposing the biofilm to ATU. The change in pH following the addition of NH<sub>3</sub> was not significantly different from the detector noise, confirming that the GFET is indeed sensitive to the nitrification activity of the biofilm. Additional control tests measured the response of the GFET sensor before biofilm growth. The bare sensor shows no response to NH<sub>3</sub>, ATU, NH<sub>2</sub>OH, and NaN<sub>3</sub> (Figure S1).

Next, we studied the second step in NH<sub>3</sub> consumption, the utilization of NH<sub>2</sub>OH via HAO activity,



When *N. europaea* is supplied with NH<sub>2</sub>OH, it produces one H<sup>+</sup> per oxidized NH<sub>2</sub>OH molecule. Therefore, this sub-step in the NH<sub>3</sub> consumption pathway is also well suited to investigation using the GFET sensor.

The biofilm was inhibited by ATU (which inhibits AMO, but not HAO activity) and then dosed with 75 μmol of NH<sub>2</sub>OH (resulting concentration ~ 1 mM). Immediately after introducing NH<sub>2</sub>OH, we observed a sharp downward spike in pH to 5.8, then a sharp increase (Fig. 4). Over the next 30 minutes, the pH inside the biofilm oscillates and finally stabilizes below the starting pH.

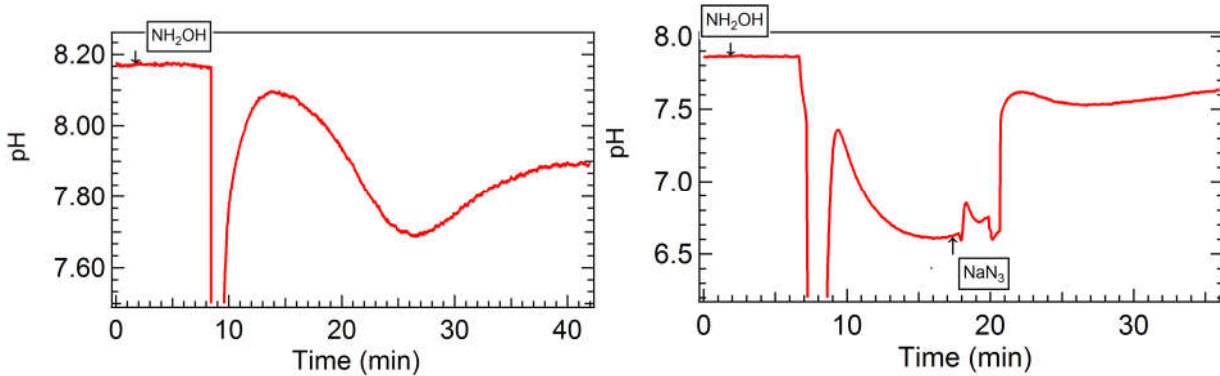


**Figure 4.** a) Response to NH<sub>2</sub>OH. b) Response to NH<sub>2</sub>OH followed by the biocide NaN<sub>3</sub>.

The dramatic decrease in pH (Fig. 4) is strikingly different from that observed when adding a similar amount of NH<sub>4</sub><sup>+</sup> (Fig. 3). Several factors may contribute to this variance. First, and most important, there is a 30-fold difference in the concentration of available substrate. On a concentration basis, only 3 % of the NH<sub>4</sub><sup>+</sup> is present in the NH<sub>3</sub> form, while almost 100 % of NH<sub>2</sub>OH is available. The higher concentration of NH<sub>2</sub>OH would potentially create a steeper gradient for the initial diffusion into the biofilm and a more rapid initial release of H<sup>+</sup>.

The rapid changes in pH detected by the GFET (Fig. 4) highlight the advantage of real-time sensing inside the biofilm. A moderate dose of NH<sub>2</sub>OH causes rapid swings in local pH that are not observable in the bulk fluid. It appears that the initial rate of NH<sub>2</sub>OH consumption is too fast to be sustained, leading to inhibitory pH levels. Subsequent oscillations in pH suggest that the biofilm adapts to this situation by lowering its rate of NH<sub>2</sub>OH consumption. The ability to continuously monitor such temporal changes within a biofilm holds much promise.

The biofilm was dosed with NH<sub>2</sub>OH two more times (11 hours later and 38 hours later). In both cases, the GFET recording of pH exhibited similar oscillatory behavior. Shortly after the final dose of NH<sub>2</sub>OH, the biofilm was poisoned by the introduction of sodium azide (NaN<sub>3</sub>) (Fig 4b).

The pH inferred from the GFET biosensor indicates a sudden upward jump in pH 6 minutes after the addition of NaN<sub>3</sub>.

We interpret the NaN<sub>3</sub> response as follows: for the first 6 minutes after the addition of NaN<sub>3</sub>, the pH does not change dramatically, but the signal appears unstable. The biofilm microorganisms may still be alive, but increasingly vulnerable to perturbations due to a loss of resilience.<sup>22</sup> After 6 minutes, we interpret the jump in pH as a catastrophic collapse of the population as the local concentration of NaN<sub>3</sub> became lethal. The upward swing in pH is likely caused by a sudden halt to H<sup>+</sup> production in the biofilm and a subsequent equilibration with the bulk fluid. While this interpretation is speculative, it suggests interesting directions for future research. It is particularly exciting to consider the possibility of detecting early warning signs of an impending population collapse. It also provides a potential *in-situ* method of monitoring processes used to control the growth of nitrifying biofilms in drinking water distribution systems.<sup>23</sup>

#### 4.4 Conclusion

In conclusion, the GFET sensor was found to be a promising means of monitoring dynamic changes of pH inside a biofilm in response to changes in nitrification activity. Future work will include the development of GFET sensor arrays, similar to CCD imaging arrays, for spatially-resolved measurements of biofilm activity.

Additional information as noted in the text.

### Acknowledgments

Support for the study of *N. Europaea* in biofilms was provided by a grant from the National Science Foundation's Division of Chemical, Bioengineering, Environmental and Transport Systems Environmental Health and Safety of Nanotechnology program (No. 1067572). Development of the GFET biosensor was supported by the National Science Foundation under grant no. 1450967. We thank Dustin Swanson for his help maintaining the biofilm.

#### 4.4 References

- (1) Syron, E.; Casey, E. Critical Review Membrane-Aerated Biofilms for High Rate Biotreatment: Performance Appraisal , Engineering Principles , Scale-up , and Development Requirements. *Environ. Sci. Technol.* **2008**, *42*, 1833–1844.
- (2) Suidan, M. T. Performance of Deep Biofilm Reactors. *J. Environ. Eng.* **1986**, *112*, 78–93.
- (3) Liu, Y.; Dong, X.; Chen, P. Biological and chemical sensors based on graphene materials. *Chem. Soc. Rev.* **2012**, *41*, 2283–2307.
- (4) Li, J.; Wang, G.; Zhu, H.; Zhang, M.; Zheng, X.; Di, Z.; Liu, X.; Wang, X. Antibacterial activity of large-area monolayer graphene film manipulated by charge transfer. *Sci. Rep.* **2014**, *4*, 4359.
- (5) Bendali, A.; Hess, L. H.; Seifert, M.; Forster, V.; Stephan, A.-F.; Garrido, J. a; Picaud, S. Purified neurons can survive on peptide-free graphene layers. *Adv. Healthc. Mater.* **2013**, *2*, 929–933.
- (6) Arp, D. J. et al. *The Nitrogen Cycle In Prokaryotic Nitrogen Fixation*; Triplett, E., Ed.; Horizon Scientific Press: Norfolk, U.K., 2000.
- (7) Prosser, J. I. Autotrophic Nitrification in Bacteria. *Adv. Microb. Physiol.* **1989**, 125–181.
- (8) Byers, J. D.; Lazarova, V.; Manem, I. *BiofilmsII*; Wiley: New York, 2000; pp. 159–206.
- (9) EPA. U. S. Process Design Manual: Nitrogen Control. In; U.S. Environmental Protection Agency: Washington, D.C., 1993; p. 625/R – 93/010.
- (10) Li, X.; Cai, W.; An, J.; Kim, S.; Nah, J.; Yang, D.; Piner, R.; Velamakanni, A.; Jung, I.; Tutuc, E.; et al. Large-area synthesis of high-quality and uniform graphene films on copper foils. *Science* **2009**, *324*, 1312–1314.
- (11) Saltzgaber, G.; Wojcik, P.; Sharf, T.; Leyden, M. R.; Wardini, J. L.; Heist, C. A.; Adenuga, A. A.; Remcho, V. T.; Minot, E. D. Scalable graphene field-effect sensors for specific protein detection. *Nanotechnology* **2013**, *24*, 355502.
- (12) Cheng, Z.; Li, Q.; Li, Z.; Zhou, Q.; Fang, Y. Suspended graphene sensors with improved signal and reduced noise. *Nano Lett.* **2010**, *10*, 1864–1868.
- (13) Lauchnor, E. G.; Radniecki, T. S.; Semprini, L. Inhibition and gene expression of *Nitrosomonas europaea* biofilms exposed to phenol and toluene. *Biotechnol. Bioeng.* **2011**, *108*, 750–757.
- (14) Stine, R.; Mulvaney, S. P.; Robinson, J. T.; Tamanaha, C. R.; Sheehan, P. E. Fabrication, optimization, and use of graphene field effect sensors. *Anal. Chem.* **2013**, *85*, 509–521.

- (15) Cui, Y.; Wei, Q.; Park, H.; Lieber, C. M. Nanowire nanosensors for highly sensitive and selective detection of biological and chemical species. *Science* **2001**, *293*, 1289–1292.
- (16) Sharf, T.; Kevek, J. W.; Deborde, T.; Wardini, J. L.; Minot, E. D. Origins of charge noise in carbon nanotube field-effect transistor biosensors. *Nano Lett.* **2012**, *12*, 6380–6384.
- (17) Lauchnor, E. G.; Semprini, L.; Wood, B. D. Kinetic parameter estimation in *N. europaea* biofilms using a 2-D reactive transport model. *Biotechnol. Bioeng.* **2015**. DOI 10.1002/bit.25517.
- (18) Suzuki, I.; Dular, U. Ammonia or Ammonium Ion Ammonia or Ammonium Ion as Substrate for Oxidation by *Nitrosomonas europaea* Cells and Extracts. *J. Bacteriol.* **1974**, *120*, 556–558.
- (19) Lauchnor, E. G.; Semprini, L. Inhibition of phenol on the rates of ammonia oxidation by *Nitrosomonas europaea* grown under batch, continuous fed, and biofilm conditions. *Water Res.* **2013**, *47*, 4692–4700.
- (20) Stewart, P. S. Guest Commentaries: Diffusion in Biofilms, Why is Diffusion an Important Process. *2003*, *185*, 1485–1491.
- (21) Juliette, L. Y.; Hyman, M. R.; Arp, D. J. Mechanism-Based Inactivation of Ammonia Monooxygenase in *Nitrosomonas europaea* by Allylsulfide Mechanism-Based Inactivation of Ammonia Monooxygenase in *Nitrosomonas europaea* by Allylsulfide. *Appl. Environ. Microbiol.* **1993**, *59*.
- (22) Dai, L.; Vorselen, D.; Korolev, K. S.; Gore, J. Generic indicators for loss of resilience before a tipping point leading to population collapse. *Science* **2012**, *336*, 1175–1177.
- (23) Berry, D.; Xi, C.; Raskin, L. Microbial ecology of drinking water distribution systems. *Curr. Opin. Biotechnol.* **2006**, *17*, 297–302.

#### 4.5 Supporting Information

#### “Graphene Biotransistor Interfaced with a Nitrifying Biofilm”

Morgan Brown<sup>1</sup>, Leila Barker<sup>2</sup>, Lewis Semprini<sup>2</sup> and Ethan D. Minot<sup>1</sup>

<sup>1</sup>*Department of Physics, Oregon State University*

<sup>2</sup>*School of Chemical, Biological and Environmental Engineering, Oregon State University*

#### 1. Control experiments with no biofilm on the sensor

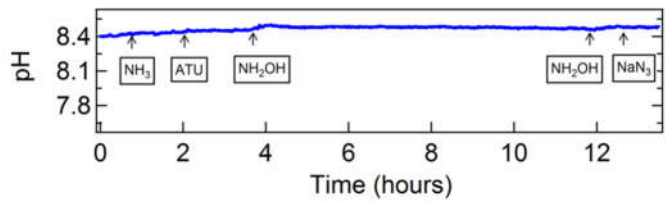


Figure S1. The response of the bare GFET sensor (no biofilm present) to aliquots of NH<sub>3</sub>, ATU, NH<sub>2</sub>OH, and NaN<sub>3</sub>. Figures in the main text show the GFET sensor response when the same aliquots were added in the presence of a biofilm.

#### 2. Establishing the biofilm on the sensor

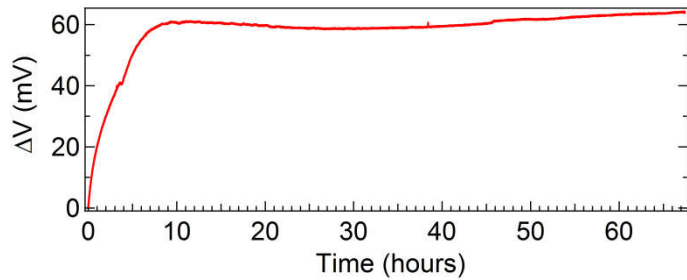


Figure S2. The shift in transistor curve,  $\Delta V$ , measured after inoculating the GFET sensor with a liquid suspension of *N. Europea* at  $t = 0$ .

### 3. Verifying metabolic activity

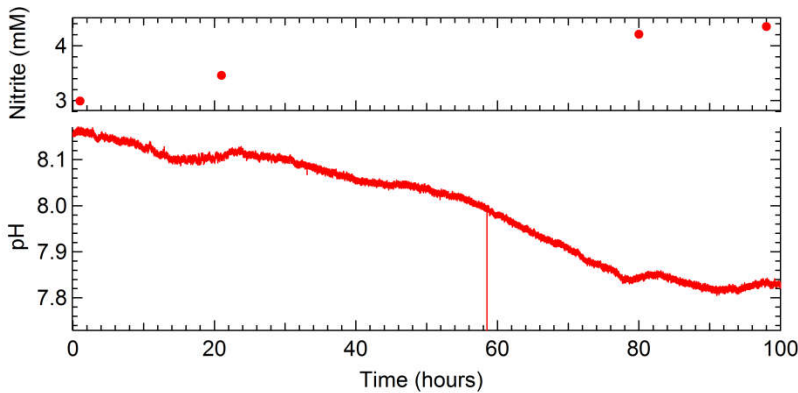


Figure S3. Metabolic activity of the biofilm monitored by measuring the nitrite ( $\text{NO}_2^-$ ) concentration (upper panel) and the GFET-based pH sensor (lower panel). At the start of the test, the biofilm was dosed with  $31 \mu\text{mol}$  of  $(\text{NH}_4)_2\text{SO}_4$ , which yielded an initial  $\text{NH}_4^+$  concentration of approximately 1 mM. The metabolic activity of the biofilm produces  $\text{NO}_2^-$  and a decrease in pH.

### 4. Estimating diffusion time scales

The time scale for diffusion can be estimated from the experimental geometry and the diffusion constant for  $\text{NH}_3$  and  $\text{H}^+$ . Stewart et al.<sup>20</sup> calculated the time to 90 % equilibrium for a flat biofilm slab at  $t_{90} = 1.03L^2/D_e$ , where  $L$  is the biofilm thickness and  $D_e$  is the effective diffusion coefficient. Diffusion coefficients are typically reduced inside the biofilm compared to the bulk. For small molecules,  $D_e \sim 0.8D_{\text{bulk}}$ .<sup>20</sup> For  $\text{NH}_3$ , we estimate  $D_e \sim 1.6 \times 10^{-5} \text{ cm}^2/\text{s}$ , and for  $\text{H}^+$  we estimate  $D_e \sim 7 \times 10^{-5} \text{ cm}^2/\text{s}$ . For an assumed biofilm thickness of 0.1 cm, we estimate  $t_{90} = 8 \text{ minutes}$  for  $\text{NH}_3$  and 2 minutes for  $\text{H}^+$ . The equilibration times would be further lengthened by the boundary layer between the biofilm and the bulk fluid.

### 5. Comparison with microprobe measurements

Lanchnor et al.<sup>17</sup> report the results of microprobe measurements and numerical modeling of dissolved oxygen (DO) and pH within a biofilm of *N. europaea*. The studies were done using a

buffer strength of 1 mM HEPES (similar to the 6 mM buffer used for experiments reported here) and with a biofilm thickness of 300  $\mu\text{M}$ . The measured DO profiles indicate that when 5 mM of  $\text{NH}_4^+$  is present in the bulk solution, DO is completely depleted inside the biofilm (at a depth of 300  $\mu\text{m}$ ). Dissolved oxygen is also depleted and limits the rate of metabolism inside the biofilm when using 1.5 mM and 0.5 mM of  $\text{NH}_4^+$  (similar to the 1 mM concentration used for the experiments reported here). They observed a decrease in pH within the biofilm from 7.8 to 6.6 when 1.5 mM of  $\text{NH}_4^+$  was added.

## CHAPTER 5

### **An atomically-thin sensor patch for recording from single electrogenic cells**

Morgan Brown, Michael Reynolds, Kathryn McGill, Jesse Goldberg, Patrick Chappell, Paul McEuen, Ethan Minot

This manuscript is in preparation for publication.

### 5.1 Introduction

A major obstacle in creating brain-machine interfaces is the discrepancy in mechanical stiffness between living cells and traditional electrical probes. Glass micropipettes (filled with conductive fluid), sharp metal probes and silicon-based probes are unable to conform to the 3-D structure of a living cell.

Recently, progress has been made using softer materials to build brain-machine interfaces. Syringe-injectable macroporous mesh electronics developed by Liu et al. enable conformation of electronics to non-planar surfaces while simultaneously enabling deep brain delivery.<sup>1</sup> The NeuroGrid, developed by Khodagholy et al., offers a flexible array of 256 neuron size electrodes to record action potentials from the surface of the brain.<sup>2</sup> A similar device with significantly fewer electrodes was fabricated by Blaschke et al. utilizing graphene field effect transistors (FET) in place of passive electrodes.<sup>3</sup> Here graphene was chosen because it is mechanically strong, has transistor properties which enable local amplification of neuron activity, and is optically transparent to allow for simultaneous electrical and optical investigations.

A common feature of this previous work is the use of a thin plastic film to support the electrode array. Liu et al. reduced the thicknesses of their plastic film to 300 nm to reach a bending stiffness  $\sim 10^{-10}$  N·m. However, this bending stiffness is still far too large to create a sensor that can wrap around a single cell.

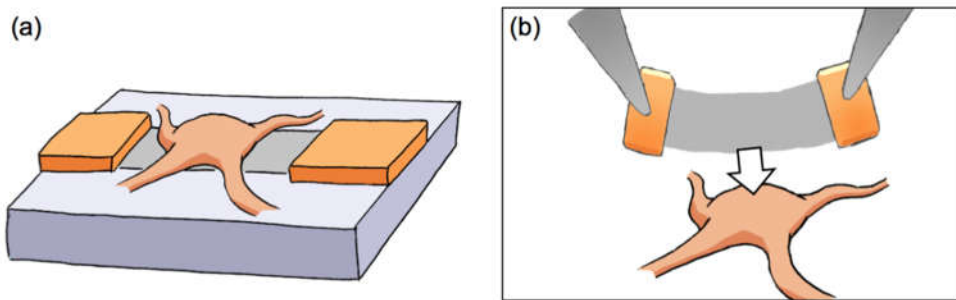


**Figure 1.** (a) Graphene membrane supported by an insulating substrate and interfaced with a single neuron. (b) Free-floating graphene membrane approaching a single neuron. (Change diagram so that graphene is transparent).

In this work we show that a free-floating graphene membrane can be interfaced with a single cell (see Figure 1b). By foregoing any support layer behind the graphene, the bending stiffness of the sensor is reduced from  $> 10^{-10}$  N·m to  $\sim 10^{-15}$  N·m. We demonstrate that the free-floating graphene can form a tight seal with the cells surface, without causing it perceptible damage. The tight seal facilitates high-fidelity measurements of electrogenic signals. Previous work has already demonstrated that graphene-based sensors can amplify extracellular neuronal voltages with excellent signal-to-noise ratio.<sup>4,5,6</sup> Here we demonstrate even larger signal strength when the neuron is wrapped with the graphene sensor.

## 5.2 Methods

### 5.2.1 Fabrication

Fabrication of releasable graphene devices utilizes standard graphene processing methods, with the addition of an alumina release layer.<sup>7</sup> We use atomic layer deposition (ALD) to deposit 10 nm of alumina on 170- $\mu$ m double-side-polished fused silica wafers (Mark Optics). Large-area graphene sheets derived from a chemical vapor deposition process (ACS Materials)<sup>8</sup> are transferred onto the alumina-coated surface, see Fig 2. Photolithography is used to pattern gold contact pads (thickness 50 nm). A second photolithography step is used to pattern the graphene strips. Unwanted graphene is removed with a 50 W 60-second oxygen plasma. We soak the chip in a mild (10:1) deionized water/HCl solution to dissolve the alumina release layer. Finally, the chip is transferred to a deionized water bath and the device can be lifted off the fused silica. Surfactants can be added to encourage release, but cannot be added in the presence of cells as it will rupture their membranes.

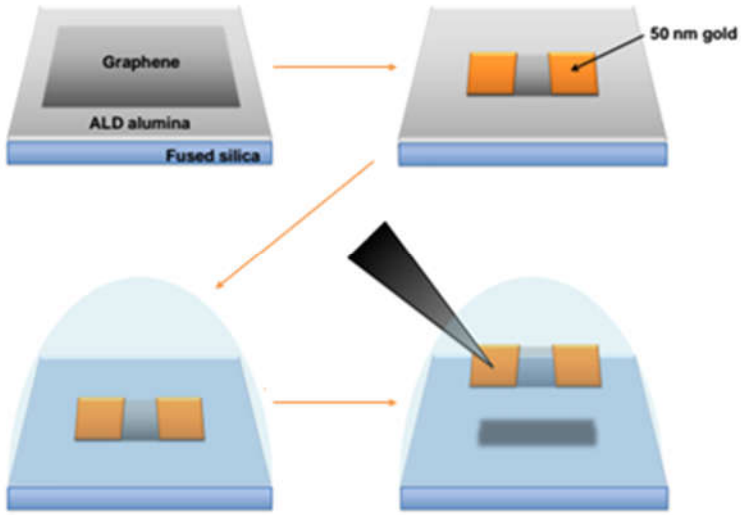


**Figure 2.** Fabrication of releasable graphene devices.

### 5.2.2 Testing

Once the graphene devices have been fabricated they are electrically characterized and a successful release is verified. The devices are placed on an adjustable stage over an inverted microscope (Olympus IN300T) with a 20 X objective. An aqueous electrolyte fluid is applied on top, as shown in Figure 3b. The device is contacted electrically using a pair of  $1\text{-M}\Omega$  parylene-C coated metal microelectrode probes (MicroProbes for Life Sciences). The microelectrode probes also facilitate mechanical manipulation of the device. Figure 3a shows a released graphene device with the Au contact pads visible as rectangles on each side and a probe visible contacting the left pad. The parylene-C coating electrically insulates the probes from the liquid environment, except for a small area ( $\sim 50 \mu\text{m}^2$ ) at the tip of the probe. The probes are held by customized 3-axis micromanipulators (Siskiyou design), Figure 3b. For all sensing experiments, the FET are biased with a source-drain voltage,  $V_{sd} = 100 \text{ mV}$ . The electric potential of the liquid was controlled with an Ag/AgCl reference electrode attached to a voltage source (see Figure 3b).

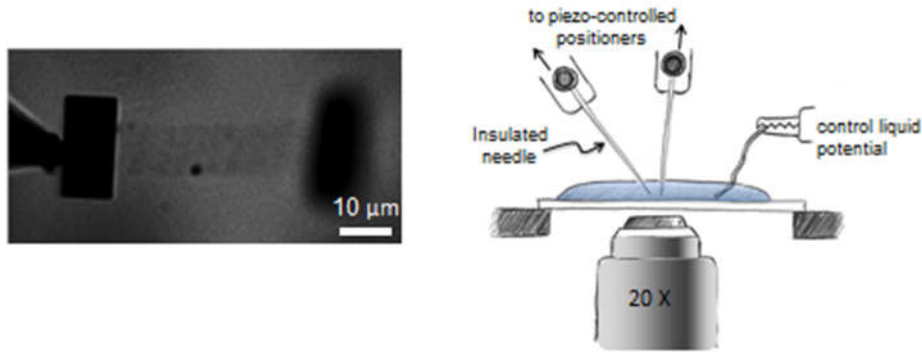


**Figure 3.** (a) Image of device released from the surface in fluid (b) cartoon of setup

### 5.2.3 Cell culturing and confocal Ca<sup>++</sup> activity verification

Immortalized mouse hypothalamic neurons were obtained from Dr. Patrick Chappell (College of Veterinary Medicine, OSU). KTaR-1 and KTaV-3 are robust electrogenic cells that can grow on glass slides in 1 - 2 days. Variation in spiking activity can be elicited by varying hormone concentration in the cell media.<sup>9</sup> These cells were cultured to the required density using an incubator (NUAIRE, NU-5100E/G) and growth medium consisting of 500 ml Dulbecco's modified eagle medium (DMEM), 50 ml fetal bovine serum (FBS), and 10 ml penicillin streptomycin (AB).

To verify cell activity, we performed calcium fluorescent imaging. The electrogenic activity of many cells, including most neurons and cardiomyocytes, involves cellular intake of Ca<sup>2+</sup> through selective ion channels.<sup>10</sup> As a result, the electrogenic activity of individual cells can then be monitored by introducing fluorescent dyes that are sensitive to Ca<sup>2+</sup> concentration into cells. The cells are then probed with an excitation wavelength and the longer fluorescent wavelength associated with the dye of choice is monitored for electrogenic driven variations in intensity. The neuron cells were soaked in Cal-520 (15 uM) fluorescent dye for one hour to allow time for the dye to permeate the cell membrane, and then rinsed prior to imaging. Confocal microscopy (DMI 4000B, Lecia) was performed at various scan rates using an excitation wave length of 488 nm and a 10 X oil immersion lens. The brightness of the fluorescent signal is modulated by Ca<sup>2+</sup> concentration.

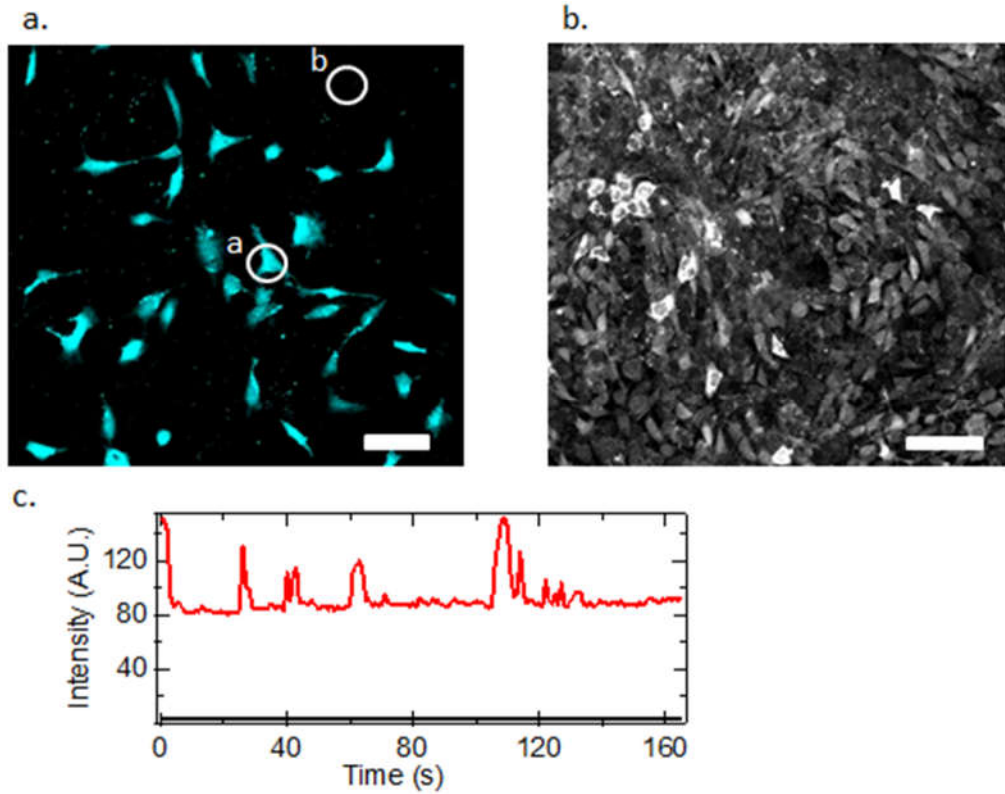


**Figure 4.** (a) Confocal microscopy images of Cal-520 fluorescence. Higher signal strength corresponds to higher  $\text{Ca}^{2+}$  concentration. A low density of neuron cells was chosen to verify electrogenic activity, 40  $\mu\text{m}$  scale bar. (b) Same imaging technique as panel a, however, the cells have multiplied and formed a confluent layer, 80  $\mu\text{m}$  scale bar. (c) Time dependence of the fluorescence intensity from the neuron circled in panel a. The spikes in intensity indicate neuron activity (red) from position a. Control intensity (black) taken from position b.

Additional experiments were performed with cardiomyocytes derived from induced pluripotent stem cells were obtained and cultured in the lab of Dr. Jan Lammerding (Cornell University). These cells exhibit spontaneous beating. An active cardiomyocyte undergoes mechanical contractions, like a beating heart. The frequency of these contractions is approximately 0.1 Hz. The contractions are easily observed in our optical microscope, and provide a useful assay of cell health.

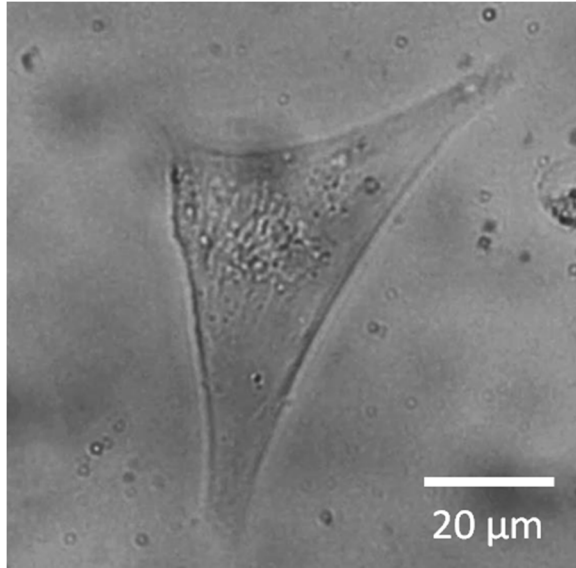


**Figure 5.** Typical healthy cardiomyocyte cell, imaged with inverted optical microscope.

### 5.3 Results and discussion

#### 5.3.1 Graphene Cell interface

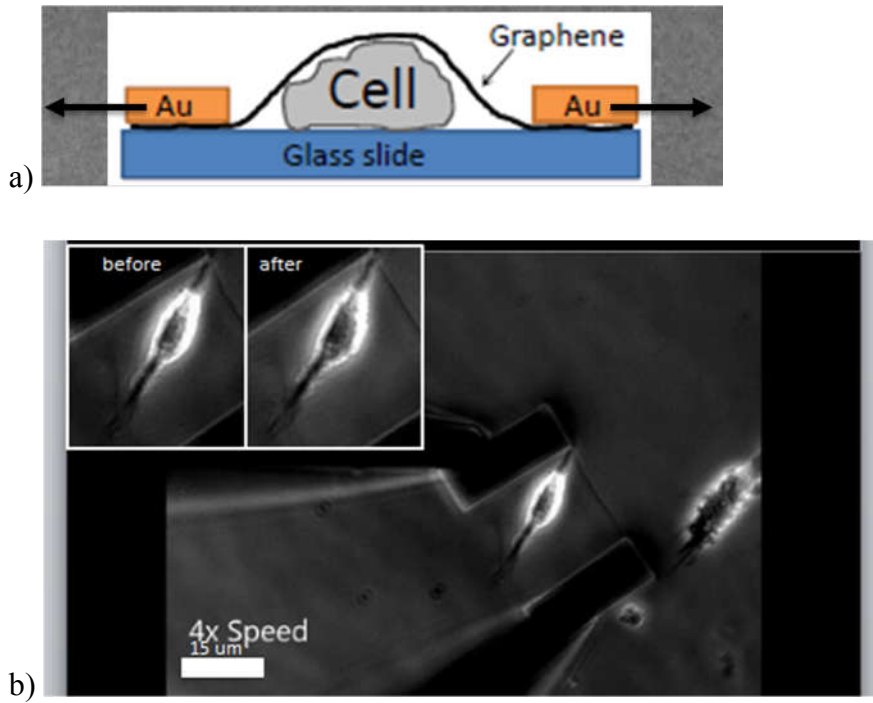


**Figure 6.** (a) Cartoon depicting the process of stretching of graphene device over a cell. (b) Stretching a graphene sensor over a beating cardiomyocyte.

Experiments were performed with beating cardiomyocytes to demonstrate that the cell contractions are not perturbed by wrapping the cell with graphene. Figure 6a shows the process by which a graphene device is placed over a beating cardiomyocyte. Pressure is applied to the cell by stretching the graphene device with the attached probes. A subtle difference in cell shape can be observed in the insert of figure 6b, showing a cardiomyocyte which remains beating after the graphene device is stretched over it. In the image on the right the cell is slightly larger, indicating that a gentle mechanical pressure is flattening the cell. The large area of the graphene device ensures the applied pressure is below the critical pressure required to rupture a cell membrane. Previous authors have estimated that this critical pressure is  $\sim 100$  kPa<sup>11</sup>. The gentle pressure is desirable for electrical measurements because a tight seal (high resistance cleft) is expected to increase the fidelity of electrical measurements.

We expect that mechanical control over the neuron/graphene interface will facilitate improvements in signal strength. To estimate signal strength we use a circuit model for the interface between a neuron and a planar device.<sup>12</sup> Figure 7 shows the cleft formed between an impermeable graphene electrode and a neuron membrane. When the neuron fires, ion channels in the membrane open and the membrane resistance reaches a value  $R_{\text{mem}}$ . For a  $10 \mu\text{m} \times 10 \mu\text{m}$  patch of membrane, typical  $R_{\text{mem}} \sim 1 \text{ G}\Omega$ . Current is driven through the membrane by the voltage difference  $V_{\text{in}} - V_{\text{cleft}}$ . The ions flow through the cleft and escape into the grounded electrolyte bath ( $V_{\text{bath}} = 0$ ). The restricted path for ions to move through the cleft is modeled as a resistance,  $R_{\text{escape}}$ . At the start of a neuron firing event, we assume the membrane capacitance,  $C_{\text{mem}}$ , is charged to a voltage  $\sim 70 \text{ mV}$ .

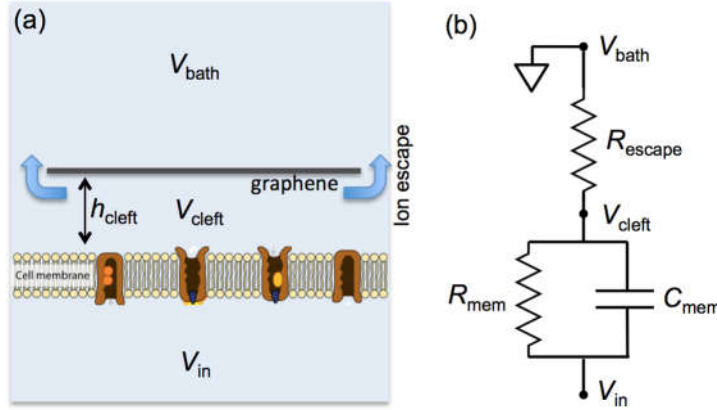


**Fig 7.** (a) The cleft formed between a flexible graphene electrode and a cell membrane. Blue arrows indicate the path of ionic current. (b) A simplified circuit model to estimate the magnitude of  $V_{\text{cleft}}$ .

As shown in Fig 7a, the graphene electrode is in contact with both  $V_{\text{cleft}}$  and  $V_{\text{bath}}$ . Assuming  $V_{\text{bath}} = 0$ , the graphene will record a signal  $V_{\text{cleft}}/2$ . To boost  $V_{\text{cleft}}$ , the resistance  $R_{\text{escape}}$  should be maximized.

To estimate  $R_{\text{escape}}$ , consider the bulk resistivity of a physiological electrolyte ( $\sim 0.5 \Omega \cdot \text{m}$ ) and the height of the cleft. If  $h_{\text{cleft}} = 50 \text{ nm}$ , we expect the sheet resistance of the cleft to be  $10 \text{ M}\Omega/\text{sq}$ . Indeed, Braun et al. have measured the cleft sheet resistance for rat brain nerve cells on  $\text{SiO}_2$  ( $h_{\text{cleft}} = 50 \text{ nm}$ ) and found  $10 \text{ M}\Omega/\text{sq}$ <sup>13</sup>. A first approximation for  $R_{\text{escape}}$  is therefore

$$R_{\text{escape}} \approx \frac{500 \text{ M}\Omega \cdot \text{nm}}{h_{\text{cleft}}}$$

The escape resistance forms a voltage divider with the time-dependent resistance  $R_{\text{mem}}$ . During an action potential, the membrane potential  $R_{\text{mem}}$  drops to  $1 \text{ G}\Omega$ . For  $h_{\text{cleft}} = 50 \text{ nm}$ , and  $V_{\text{in}} = 70 \text{ mV}$ , we would then expect  $V_{\text{cleft}}$  to reach  $\sim 1 \text{ mV}$  and the signal detected by the graphene device  $\sim 0.5 \text{ mV}$ . This simplified model of the sensing mechanism highlights the importance of minimizing  $h_{\text{cleft}}$ . Reducing  $h_{\text{cleft}}$  to  $5 \text{ nm}$  would increase the signal detected by the graphene device to  $\sim 5 \text{ mV}$ .

### 5.3.2 Time- and voltage-resolution of the sensor.

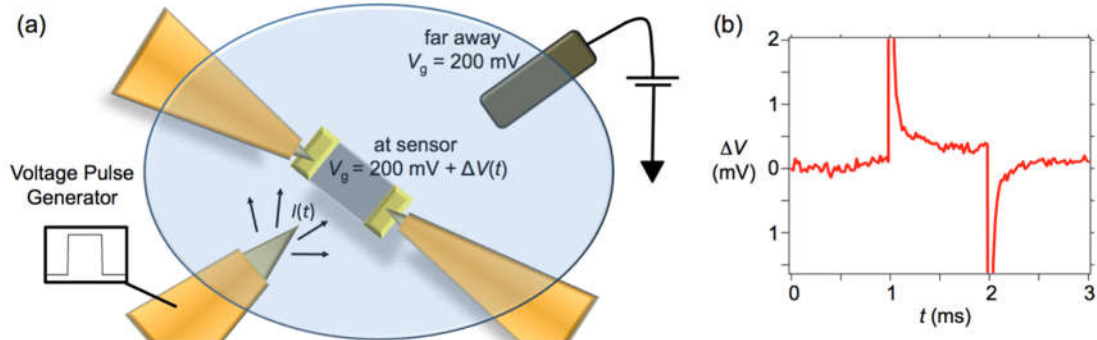


**Figure 8.** (a) Simulating a cell firing event by generating a spreading current near a flexible graphene device. (b) Recording from the flexible graphene device.

To test the temporal resolution and voltage resolution of a flexible and moveable graphene electrode, we used a non-biological system to emulate the extracellular voltage signal produced by a neuron. A graphene electrode was moved through electrolyte solution and positioned within  $\sim 50 \text{ nm}$  of a stimulating microelectrode (Fig 8a). A square-wave voltage pulse was applied to the stimulating electrode, causing a spreading current to move through the fluid. The rising step of the voltage pulse causes a positive spike in current as ions charge the double-layer capacitance of the microelectrode. The falling step of the voltage pulse causes a negative spike in current. The graphene device detects the voltages associated with these ionic currents. The change in local electrostatic potential (a few mV) is then amplified by the graphene device. The raw signal (a change in graphene resistance), is converted into voltage using the pre-measured calibration curve for the device (not shown). The recording (Fig. 8b) has  $\sim 0.1 \text{ mV}$  voltage resolution, and  $\sim 0.1 \text{ ms}$  time resolution.

### 5.3.3 Noise resolution of the sensor

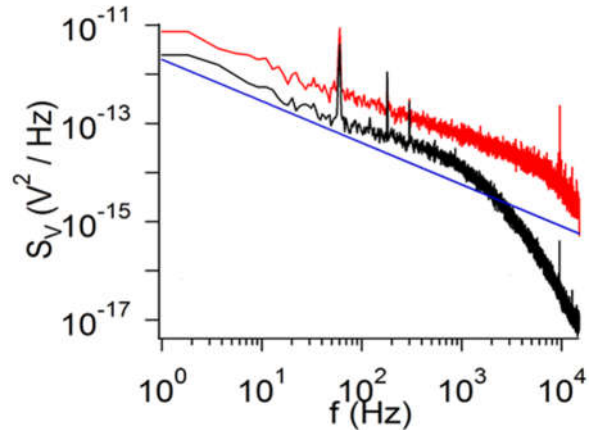


**Figure 9.** Noise spectrum of a graphene FET with (red) and without (black) High pass filtering. The thermal noise limit is shown in blue for comparison.

As shown in Figure 9, our graphene devices approach the theoretical noise limit proposed by Crosser et al.<sup>14</sup> The method for measuring  $S_v$  is discussed in chapter 1 section 6. The noise characteristics of the device are affected by the sensitivity of the current pre-amplifier. If low sensitivity is used, the signal suffers from discretization caused by digitization (red curve, Fig. 9). Optimizing the sensitivity of the current pre-amplifier (by subtracting the baseline DC current prior to amplification) we find a noise level that is close to the theoretical noise limit. We find a voltage resolution of  $\sim 10 \mu\text{V}$  rms for a fluid gated  $10 \times 10 \mu\text{m}$  sheet, which is similar to the noise level expected for traditional passive metal microelectrodes of a similar size. A similar noise level can be achieved with a traditional metal microelectrode of the same surface area, however, graphene offers multiple advantages. First, traditional microelectrodes make poor contact with the cell membrane – the observed signal strength is typically less than 0.5 mV. Second, traditional microelectrodes are passive – the signal is not amplified at the source. Third, graphene offers improved biocompatibility.

### 2.3.4 Experiments with neurons

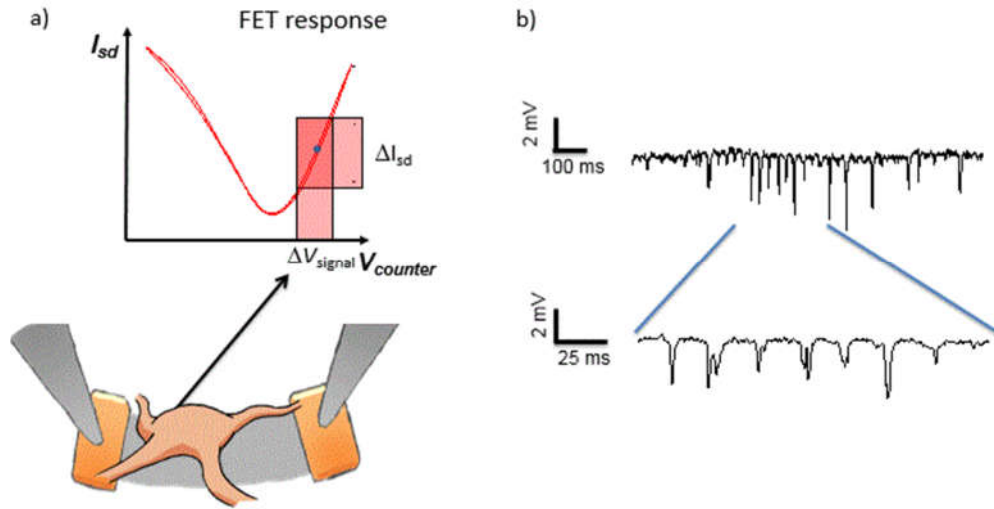


**Figure 10.** (a) The  $I_{sd}$  vs  $V_{counter}$  FET response is determined, to maximize DI resulting from small  $dV_{signal}$ . (b) Estimated  $V_{signal}$  of Immortalized mouse hypothalamic neurons on graphene.

The graphene device works as a FET to locally amplify the signal from the cell. The device is first characterized by applying a small bias across it and measuring the transfer curve (Fig. 10a). The counter electrode voltage (which controls the average liquid potential across the whole sample) is then set to maximize  $\Delta I$  for a small change in  $V_{counter}$ . Neuron spiking produces a local change  $\Delta V_{signal}$ . The resulting change in current,  $\Delta I$ . The magnitude of  $\Delta I$  can be used to estimate  $\Delta V_{signal}$ , as discussed below.

There is not a one-to-one correspondence between  $V_{counter}$  and the liquid potential,  $V_{liquid}$  (see discussion in chapter 2, section 4). To accurately measure  $dI/dV_{liquid}$  for a graphene FET, it is important to measure  $V_{liquid}$  by placing a reference electrode to the liquid and using a high impedance voltage amplifier to monitor  $V_{liquid}$ . From such experiments we find that  $dI/dV_{liquid} \sim 0.8 * dI/dV_{counter}$ . Therefore, we estimate that  $\Delta V_{signal} = 0.8 * \Delta I / (dI/dV_{counter})$

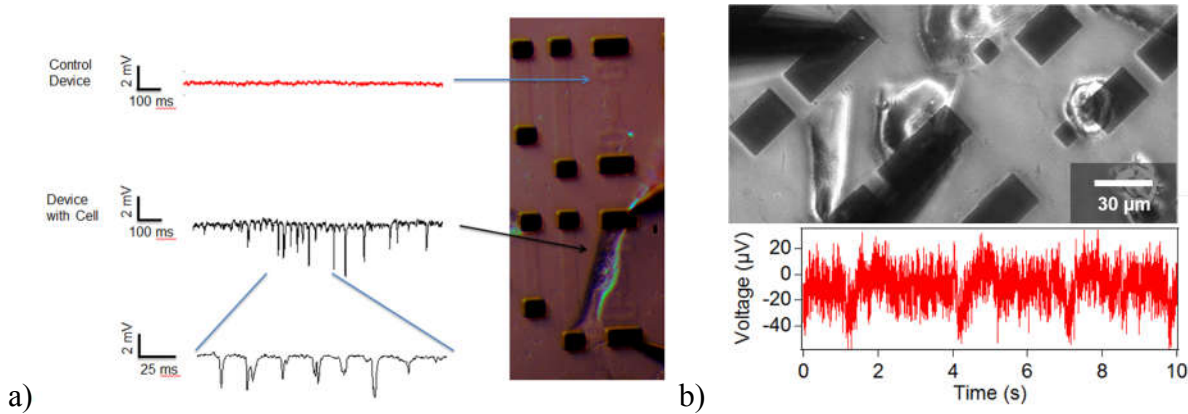


**Figure 11.** Optical and electrical data from cells grown on GFET devices. Graphene (optically transparent) is between gold pads (black rectangles). (a) Neurons grown on graphene and control. (b) Beating cardiomyocytes, where mechanical beating was confirmed to coincide with electrical device response.

Immortalized neurons were grown on top of graphene devices and a rapid spiking rate was observed after chemical triggering, as shown in Figure 11a. The control device (no neuron present) shows low RMS noise levels of  $\sim 27 \mu\text{V}$  and no evidence of spiking. Devices with neurons show bursts of spikes with an amplitude of  $\Delta V_{\text{signal}} \sim 3 \text{ mV}$ . This signal-to-noise ratio is similar to that observed by other groups.<sup>6</sup> The electrical signal recorded from the cardiomyocyte is significantly smaller than that recorded from the neuron cells, Figure 11b. This is expected because of the comparatively long duration of their action potential. Others have reported similar length action potential.<sup>15,16</sup>

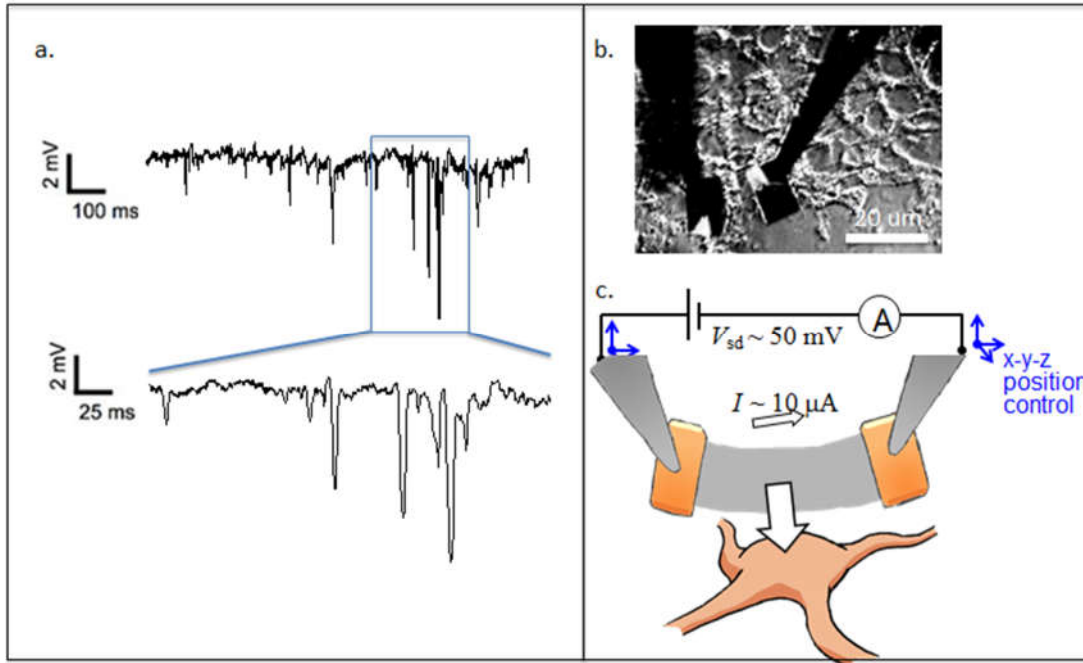


**Figure 12** (a) Spike data from a graphene device placed over a confluent layer of immortalized mouse neurons excited by altering the chemical environment (b) image of graphene device on neurons (c) cartoon of graphene device shown in b.

Initial data has been taken with a device over a confluent layer of neurons as shown in Fig. 12a. For this device,  $dI/dV_{\text{counter}} \approx 125 \mu\text{S}$ . The maximum amplitude recorded  $\Delta I \sim 1 \mu\text{A}$  and we estimate  $\Delta V_{\text{signal}} \sim 8 \text{ mV}$ . Due to the high density of neurons on the sample, it is hard to separate sensor noise from the environment noise resulting from the other neurons. In order to address, we compare these responses to those obtained from isolated the sensors with neurons and cardiomyocytes cultured directly on them.

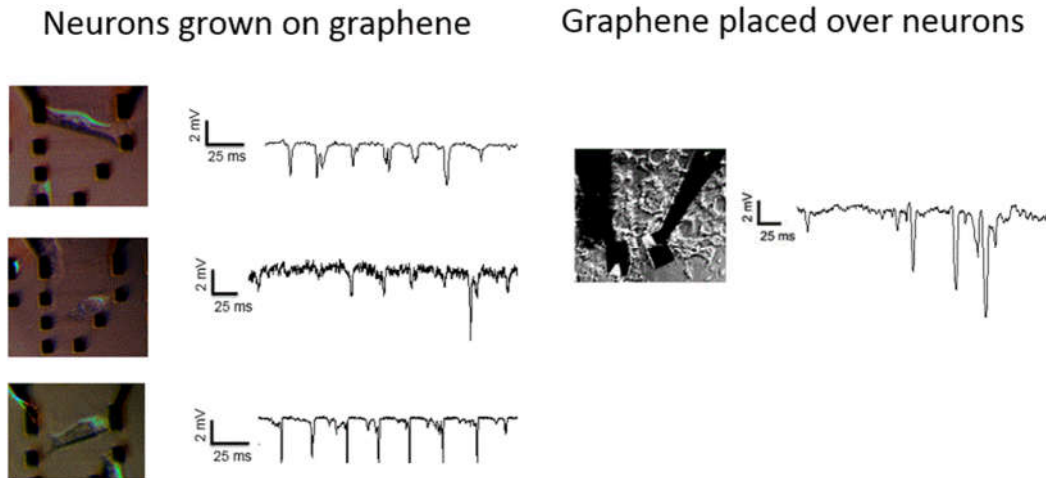
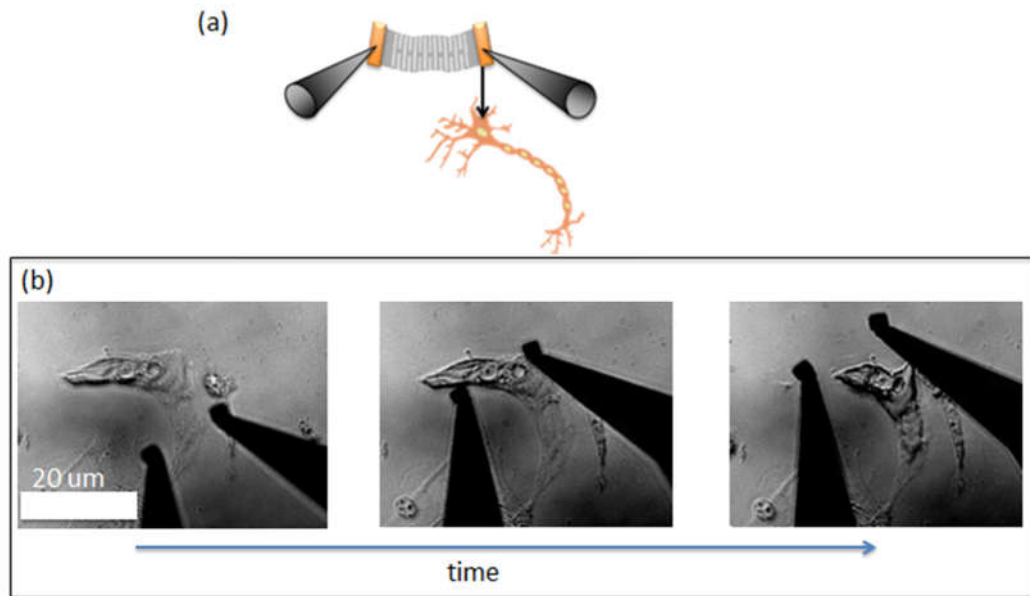


Figure 13. Neuron response compared (a) for neurons grown on graphene, note consistency observed for multiple devices, (b) and for graphene place over neurons.

Extracellular measurements of neurons are typically a compromise between the non-invasiveness and signal strength. Figure 13 shows promising data that indicates increases in signal strength are possible with substrate removal. We observe a repeatable max spike amplitude of  $\sim 3$  mV when cells are grown over devices and a  $\sim 2$ -fold increase of  $\sim 6$  mV max spike amplitude with the device placed over cells.

A possible explanation for the increase in  $\Delta V_{\text{signal}}$  is the conformal coating of the cell by the graphene device. Using the model shown in Fig. 6 for cleft resistance, the  $\sim 3$  mV spike response recorded using a surface device from a cell with  $\sim 70$  mV cell depolarization would require a resistivity of  $\sim 150$  M $\Omega$ /sq and  $h_{\text{cleft}} \sim 4$  nm. When the graphene is placed over the cell a resistivity  $\sim 250$  M $\Omega$ /sq and  $h_{\text{cleft}} \sim 2$  nm would be implied to observe a 6 mV spike.

### 5.3.5 Mechanical device designs, preliminary exploration to optimize graphene neuron interface



**Figure 14.** (a) cartoon and (b) optical images of a beating cardiomyocyte being ruptured by a metal microelectrode.

Cells are fragile. Cell walls easily rupture with environmental changes, such as variations in ionic concentrations in the fluid which result in osmotic pressure, excess surfactant, or with direct mechanical pressure from microelectrodes as shown in Figure 14. This highlights the need for careful device design. It was recently shown that the ratio of the in-plane to out-of-plane bending stiffness, or Foppl-von Karman number is similar for graphene and paper ( $\sim 10^6$ ), making paper arts such as kirigami a unique prospective for our graphene devices. Because the overall device strain simply results in bending of the graphene, the transistor response does not change significantly in this application.<sup>7</sup>

We tested a series of device designs, using kiragami for strain relief. Fig. 15a shows one type of device pulled over the cell membrane as you would with a cheese slicer. Although the cell membrane was observed to flex, the graphene spring ruptured first. We estimate that this device applied  $\sim 1$  Pa of pressure to the cell. This is well below the  $\sim 100$  kPa pressure required to rupture the lipid bilayer that makes up the cell membrane.<sup>11</sup> Through testing subsequent device designs we found there was no rupture with cantilever devices that were bendable but not stretchable. This

makes sense due to the increased area over which the force was applied to the cells. This led us to focus on optimizing on the electrical connection with the optimal seal using a solid device.

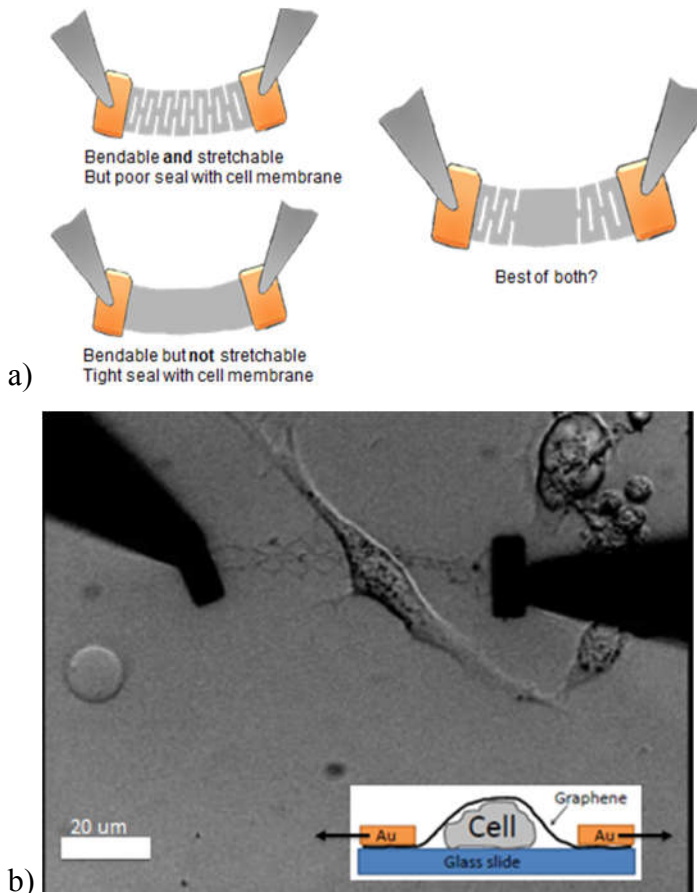


**Figure 15.** (a) Device designs (b) kirigami graphene device vs cell.

#### 5.4 Conclusion

Releasable graphene devices represent novel wearable electronics for cells with many possible applications. The biocompatibility could address the current lack of implantable flexible electronics for long term implantation.<sup>18</sup> The ability to target a single cell of interest could be used with current brain slices or cells grown on multi electrode array (MEA) devices to investigate pathways or cells not addressable with the MEA. In addition, the optical transparency allows

single cells to be measured electrically while simultaneously measuring spiking via fluorescent techniques or stimulated via optogenetic triggers.

### 5.5 Bibliography

1. Liu, J. *et al.* Syringe-injectable electronics. *Nat. Nanotechnol.* **10**, 629–636 (2015).
2. Khodagholy, D. *et al.* NeuroGrid: recording action potentials from the surface of the brain. *Nat Neurosci* **18**, 310–315 (2015).
3. Blaschke, B. M. *et al.* Flexible graphene transistors for recording cell action potentials. *2D Mater.* **3**, 0 (2016).
4. Cheng, Z. *et al.* Sensitivity limits and scaling of bioelectronic graphene transducers. *Nano Lett.* **13**, 2902–7 (2013).
5. Cohen-Karni, T., Qing, Q., Li, Q., Fang, Y. & Lieber, C. M. Graphene and nanowire transistors for cellular interfaces and electrical recording. *Nano Lett.* **10**, 1098–1102 (2010).
6. Hess, L. H. *et al.* Graphene Transistor Arrays for Recording Action Potentials from Electrogenic Cells. 5045–5049 (2011). doi:10.1002/adma.201102990
7. Blees, M. K. *et al.* Graphene kirigami. *Nature* **524**, 204–207 (2015).
8. Li, X. *et al.* Large-area synthesis of high-quality and uniform graphene films on copper foils. *Science (80-. ).* **324**, 1312–1314 (2009).
9. Jacobs, D. C., Veitch, R. E. & Chappell, P. E. Evaluation of immortalized AVPV- And Arcuate- Specific neuronal kisspeptin cell lines to elucidate potential mechanisms of estrogen responsiveness and temporal gene expression in females. *Endocrinology* **157**, 3410–3419 (2016).
10. Tada, M., Takeuchi, A., Hashizume, M., Kitamura, K. & Kano, M. A highly sensitive fluorescent indicator dye for calcium imaging of neural activity in vitro and in vivo. *Eur. J. Neurosci.* **39**, 1720–1728 (2014).
11. Rotsch, C., Jacobson, K. & Radmacher, M. Dimensional and mechanical dynamics of active and stable edges in motile fibroblasts investigated by using atomic force microscopy. *Proc. Natl. Acad. Sci. U. S. A.* **96**, 921–926 (1999).

12. Fromherz, P. Extracellular recording with transistors and the distribution of ionic conductances in a cell membrane. *Eur. Biophys. J.* **28**, 254–258 (1999).
13. Braun, D. *et al.* Imaging neuronal seal resistance on silicon chip using fluorescent voltage-sensitive dye. *Biophys. J.* **87**, 1351–9 (2004).
14. Crosser, M. S., Brown, M. a., McEuen, P. L. & Minot, E. D. Determination of the Thermal Noise Limit of Graphene Biotransistors. *Nano Lett.* 150720103852006 (2015). doi:10.1021/acs.nanolett.5b01788
15. Du, D. T. M., Hellen, N., Kane, C. & Terracciano, C. M. N. Action potential morphology of human induced pluripotent stem cell-derived cardiomyocytes does not predict cardiac chamber specificity and is dependent on cell density. *Biophys. J.* **108**, 1–4 (2015).
16. Zhang, J. *et al.* Functional cardiomyocytes derived from human induced pluripotent stem cells. *Circ. Res.* **104**, (2009).
17. Newaz, A. K. M., Puzyrev, Y. S., Wang, B., Pantelides, S. T. & Bolotin, K. I. Probing charge scattering mechanisms in suspended graphene by varying its dielectric environment. *Nat. Commun.* **3**, 734 (2012).
18. Chen, R., Canales, A. & Anikeeva, P. Neural recording and modulation technologies. *Nat. Rev. Mater.* **2**, 16093 (2017).

## CHAPTER 6

Concluding discussion

Understanding the interface that forms between an electrolyte and graphene is critical to understanding biosensing mechanisms. The electronic signals measured by a graphene FET biosensor are typically the result of changes in the layer of dissolved ions near the graphene surface. The coupling between dissolved ions and a conductive surface is described by the electric double layer capacitance,  $C_{EDL}$ . This interfacial capacitance has been studied for many years using conductive liquids and bulk metal surfaces. Only recently have careful studies of  $C_{EDL}$  focused on the interface between graphene and conductive liquids. We use Hall effect measurements to determine the total capacitance at the interface and the tight-binding-model-based theory to separate  $C_Q$  and  $C_{EDL}$ . Based on this investigation, we find a  $C_{EDL}$  of  $\sim 0.04 \text{ F/m}^2$  for biologically relevant fluids and  $\sim 0.11 \text{ F/m}^2$  for ionic liquids. Both of these values are lower than the typical value of  $0.2 \text{ F/m}^2$  found with metals. This finding is also significant for choosing ideal fluids for graphene-based super capacitors.

We have systematically characterized the noise and sensitivity of graphene FETs in aqueous electrolyte environments. We established the minimum attainable noise in this environment by determining the thermal noise limit. We then investigated charge carrier mobility, which is critical to device sensitivity. We performed Hall bar measurements on electrolyte-gated graphene assuming a Drude model, and find that the room temperature carrier mobility in water-gated,  $\text{SiO}_2$ -supported graphene reaches  $7000 \text{ cm}^2/\text{Vs}$ . This value is comparable to the best dry  $\text{SiO}_2$ -supported graphene devices. Our results show that the electrical performance of graphene is robust, even in the presence of dissolved ions that introduce an additional mechanism for Coulomb scattering.

We established two novel applications of graphene field-effect transistor biosensor. The first application is in-situ monitoring of the pH inside a living biofilm with fast temporal resolution ( $\sim 1 \text{ s}$ ) over multi-hour time periods. The atomically thin sensor is positioned between the biofilm and a supporting silicon oxide surface, providing noninvasive access to conditions at the base of the biofilm. We determine the transient changes in pH when the biofilm metabolizes substrate molecules and when it is exposed to biocide. The pH resolution is approximately 0.01 pH units when using 1 s time averaging; the sensor drift is approximately 0.01 pH units per hour. Our results demonstrate the potential of this technology to further the study of biofilm metabolism and improve monitoring of biofilm health.

The second application for GFET biosensors that we established is wearable sensor patches for single cells. Recent advances in the fields of optics, biochemistry, and nanotechnology have instigated a multidisciplinary effort to understand the neural circuitry of the human brain. The electrodes currently used for *in vivo* single neuron sensing have not significantly advanced over the past century. The industry standard remains simple, insulated, conductive shafts with small, exposed tips. Graphene-based field-effect transistors are flexible yet strong, biocompatible, and able to locally amplify the electrogenic signals produced by neurons. This combination of material characteristics makes graphene ideal for next-generation biosensing applications.

The graphene in our experiments is etched into patterns inspired by the Japanese paper art of kirigami to enable in-plane stretching. The devices are then stretched over cells, isolating the graphene from possible substrate noise while forming a conformal coating over the cell to obtain the optimal signal-to-noise ratio. The flexibility of these devices makes them promising as “wearable” electronics for cells with applications for both *in vivo* and brain-slice electrophysiological experiments. We present characterization and initial single cell measurements from these devices. First, we investigated thermal noise limits, and addressed concerns that the aqueous electrolyte environments would significantly lower carrier mobility. In addition, we present early results from electrical interaction with cardiomyocytes and immortalized mouse neuronal cells.

## CURRICULUM VITAE

Morgan Allen Brown

### **Technical Work Experience**

#### **Carbon Based Nanotechnology:** Oregon State University

- Developed a next generation nanotechnology based device to measure the firing of individual neurons. Currently funded by the BRAIN initiative in a collaborative effort with Cornell University to long timescale biocompatible *in vivo* neural recordings.
- My role encompasses fabrication, preparation of neurons, and measurement of the electrophysiological response of neurons and cardiomyocytes with Kiragami (Japanese art of paper cutting) patterned graphene transistors.
- Characterized the fundamental thermal noise limit of graphene biotransistors in aqueous electrolyte environments.
- Researched substrate consumption by *N. europaea* biofilms via a high temporal resolution pH sensing graphene biotransistor for environmental engineering applications in waste water treatment plants.
- Developed n-type nanotube device fabrication techniques and performed single electron charge trap experiments.
- Characterized graphene based capacitance response in various fluids for supercapacitor applications

#### **Thin Film Deposition and Material Characterization:** Tektronix

- Researched and tested various Hall device geometries, associated mask options and deposition alignment fixturing to tune thin film electro/magnetic properties with a focus on electron mobility.
- Characterized and defined required limits to Hall device grain size and associated post dendrite anneal processes.
- Qualified μ metal shielding vendor through rigors permeability and inductive heating tests.
- Designed in automation to cryogenic vacuum system.

#### **Mechanical Design:** Tektronix

- Designed new probe body plastics and metals in ProE and collaborated with electrical design on associated circuit board.
- Designed deposition masks and associated fixtures.
- Trained and collaborated with mechanical engineers on fixture design in China using ProE.

#### **Finite Element Analysis:** Sandia National Labs and Tektronix

- Material Model Design/Development of ferroelectric dipole rotation material model for PZT. Implemented into Sandia NL's ALEGRA FE code using C++ base, FORTRAN computationally intensive sections and Python for base bulk geometry.
- Performed numerical tests to determine impact of induced porosity in PZT using representative volume elements and bulk.
- Tested current sensing probe body failure modes under cyclical loading ProE's Mechanica.

### **Technical Skills**

|                          |  |
|--------------------------|--|
| Solid Modeling Software: | Creo Elements/ProE, AutoCAD, SolidWorks  |
| Experience operating:    | Vacuum systems for CVD, E-Beam, and Thermal deposition,<br>Scanning Electron Microscope, Atomic Force Microscope |
| Wafer Processing:        | Photolithography and mask development  |
| Computer Languages:      | Python, FORTRAN  |
| Windows:                 | Word, Excel, PowerPoint, Project, Visio  |
| Security Clearance       | For duration of work at Sandia National Labs   |

## **Global Experience**

International team leadership between USA design and China facilities  
as member of China Launch Team withTektronix

Ensured launch of new product design and R&D builds both in US and China.

Coordinated materials selection, trained fixture design team on ProE and qualified machine shop in China.

Responsible for design stabilization and final production launch in China.

School for International Training, 2000

Semester in Indonesia, independent study project: *Pencak Silat*.

American International School, Singapore, 1991-1992

## **Employment History**

Oregon State University *Research Assistant, Minot Lab*

*Summer2013-Present*

Designed fabricated and implemented carbon nanotube and Graphene based field effect transistors for biosensing applications, and to advance fundamental understanding.

Oregon State University *Instructor, Recitation and Lab*

*Fall2012-Present*

Instructor of record for Mechanics of Materials and Intro to Material Science classes, Recitation TA for calc. based physics

Tektronix, Inc. *Mechanical Design and Electro Magnetic Thin Film Deposition Technologist*

*Summer2009-Spring2012*

Mechanical design of new current sensing probes, with focus on Hall device thin film deposition and transformer development.

Tektronix, Inc. *New Product Development Manager for China Launch Team*

*Spring2008-Summer2009*

New product development and launch to schedule, SCOS, and design parameters.

Tektronix, Inc. *Vacuum System Thin Film Deposition Process Development Lead*

*Winter 2005 – Winter 2007*

Interdisciplinary role for Oscilloscopes and Probes, with focus on transformer and hall device deposition systems.

Sandia National Laboratories *Computational Physics R&D Intern/Independent Contractor*

*Summer 2003–Spring2005*

Investigation of material characteristics using numerical techniques through implementation and testing of material model.

Washington State University *Teaching Assistant/Lab Operator*

*2002-2004*

Prepared, lectured, graded, and physically applied mechanics of material concepts.

Linfield College *Group Physics Tutor, Individual Calculus Tutor, Research Assistant*

*1998-2002*

Performed and documented experimentation on Sonoluminescence, ran group tutoring sessions for physics and individual for math.

## **Publications**

- (1) Brown, M. A.; Ding, J. L.; Robbins, J. R. A Numerical Investigation of the Effect of Induced Porosity on the Electromechanical Switching of Ferroelectric Ceramics. *Ferroelectr. Lett. Sect.* **2007**, 34, 1–21.
- (2) Sharf, T.; Wang, N.-P.; Kevek, J. W.; Brown, M. A.; Wilson, H.; Heinze, S.; Minot, E. D. Single Electron Charge Sensitivity of Liquid-Gated Carbon Nanotube Transistors. *Nano Lett.* **2014**.
- (3) Brown, M. A.; Barker, L.; Semprini, L.; Minot, E. D. Graphene Biotransistor Interfaced with a Nitrifying Biofilm. *Environ. Sci. Technol. Lett.* **2015**, 150303111921006.
- (4) Crosser, M. S.; Brown, M. A.; McEuen, P. L.; Minot, E. D. Determination of the Thermal Noise Limit of Graphene Biotransistors. *Nano Lett.* **2015**, 150720103852006.
- (5) Wilson, H.; Ripp, S.; Prisbrey, L.; Brown, M. A.; Sharf, T.; Myles, D. J. T.; Blank, K. G.; Minot, E. D. Electrical Monitoring of sp<sup>3</sup> Defect Formation in Individual Carbon Nanotubes. *J. Phys. Chem. C* **2016**, acs.jpcc.5b11272.

- (6) Brown, M. A., Crosser, M.S., Leyden, M. R., Qi, Y., Minot, E. D., Measurement of High Carrier Mobility in Graphene in an Aqueous Electrolyte Environment. *Applied Physics Letters*, **2016**, 093104

(7) Brown, M. A., Michael Reynolds, Kathryn McGill, Jesse Goldberg, Patrick Chappell, Paul McEuen, Ethan Minot. An atomically-thin sensor patch for recording from single electrogenic cells. *In preparation.*

(8) Brown M. A., Crosser, M.S., Feng, Z., Minot, E. D., Establishing Accurate Capacitance Value Expectations for Graphene Supercapacitors Via Hall Measurements. *In preparation.*

## Education

PhD Oregon State University  
*date Fall 2017*

### *Expected*

Major: Material Science

Thesis: *Graphene Biotransistors, an Exploration into Neurosensing and Biofilm-sensing Applications*

M.S. Washington State University  
*Fall 2005*

## Major: Mechanical Engineering

Thesis: A Numerical Investigation of the Effect of Induced Porosity on the Electromechanical switching in PZT

B.A. Linfield College  
*May 2002*

Majors: Applied Physics and Math, Minor: Music

School for International Training: *Semester Abroad Indonesia*

## Hobbies

**Hood to Coast** Ran logistics and participated on Tektronix's Megahertz corporate men's relay team

**Principal Violist** Washington State University and Linfield College Symphony Orchestras

## BIBLIOGRAPHY

CH1

- 1 Y. Huang, X. Dong, Y. Liu, L.-J. Li, and P. Chen, *J. Mater. Chem.* 21, 12358 (2011).
- 2 A. Prindle, J. Liu, M. Asally, S. Ly, J. Garcia-Ojalvo, G.M. Suel, and G.M. Süel, *Nature* 527, 59 (2015).
- 3 M. Ackermann, *Science* (80- ). 300, 1920 (2003).
- 4 C. Xie, J. Liu, T.-M. Fu, X. Dai, W. Zhou, and C.M. Lieber, *Nat. Mater.* 14, (2015).
- 5 Z.C. Lin, C. Xie, Y. Osakada, Y. Cui, and B. Cui, *Nat. Commun.* 5, 3206 (2014).
- 6 G. Buzsáki, *Nat. Neurosci.* 7, 446 (2004).
- 7 D. Khodagholy, J.N. Gelinas, T. Thesen, W. Doyle, O. Devinsky, G.G. Malliaras, and G. Buzsaki, *Nat Neurosci* 18, 310 (2015).
- 8 A.K. Geim and K.S. Novoselov, *Nat. Mater.* 6, 183 (2007).
- 9 G.-H. Lee, R.C. Cooper, S.J. An, S. Lee, A. van der Zande, N. Petrone, A.G. Hammerberg, C. Lee, B. Crawford, W. Oliver, J.W. Kysar, and J. Hone, *Science* 340, 1073 (2013).
- 10 M. Klintenberg, S. Lebègue, C. Ortiz, B. Sanyal, J. Fransson, and O. Eriksson, *J. Phys. Condens. Matter* 21, 335502 (2009).
- 11 B. Partoens and F.M. Peeters, *Phys. Rev. B - Condens. Matter Mater. Phys.* 74, 1 (2006).
- 12 K.I. Bolotin, K.J. Sikes, Z. Jiang, M. Klima, G. Fudenberg, J. Hone, P. Kim, and H.L. Stormer, *Solid State Commun.* 146, 351 (2008).
- 13 S. Das Sarma, S. Adam, E.H. Hwang, and E. Rossi, *Rev. Mod. Phys.* 83, 407 (2011).
- 14 E. Hwang, S. Adam, and S. Sarma, *Phys. Rev. Lett.* 98, 186806 (2007).
- 15 M. Weinert, G. Schneider, R. Podloucky, and J. Redinger, *J. Phys. Condens. Matter* 21, 84201 (2009).

- 16 K.S. Novoselov, V.I. Fal'ko, L. Colombo, P.R. Gellert, M.G. Schwab, and K. Kim, *Nature* 490, 192 (2012).
- 17 Y. Liu, X. Dong, and P. Chen, *Chem. Soc. Rev.* 41, 2283 (2012).
- 18 J. Ye, M.F. Craciun, M. Koshino, S. Russo, S. Inoue, H. Yuan, H. Shimotani, A.F. Morpurgo, and Y. Iwasa, *Proc. Natl. Acad. Sci. U. S. A.* 108, 13002 (2011).
- 19 R.S. Gonnelli, E. Piatti, A. Sola, M. Tortello, F. Dolcini, S. Galasso, J.R. Nair, C. Gerbaldi, E. Cappelluti, M. Bruna, and A.C. Ferrari, *2D Mater.* 4, 35006 (2017).
- 20 P. Massobrio, G. Massobrio, and S. Martinoia, *Front. Neurosci.* 10, 1 (2016).
- 21 R. Stine, S.P. Mulvaney, J.T. Robinson, C.R. Tamanaha, and P.E. Sheehan, *Anal. Chem.* 85, 509 (2013).
- 22 M.D. Stoller and R.S. Ruoff, 1 (n.d.).
- 23 S. De Liberato, C. Ciuti, D. Auston, M. Nuss, S. Keiding, M. Van Exter, C. Fattinger, A.J. Taylor, C. Highstrete, M. Lee, R.D. Averitt, E. Smirnova, A. Azad, H. Chen, G. Scalari, M.I. Amanti, M. Beck, and J. Faist, *Science* (80-. ). 335, 1326 (2012).
- 24 M.A. Brown, M.S. Crosser, M.R. Leyden, Y. Qi, and E.D. Minot, *Appl. Phys. Lett.* 109, 93104 (2016).
- 25 M.S. Crosser, M. a. Brown, P.L. McEuen, and E.D. Minot, *Nano Lett.* 15, 5404 (2015).
- 26 M.S. Crosser, M. a. Brown, P.L. McEuen, and E.D. Minot, *Nano Lett.* 150720103852006 (2015).
- 27 M.Y. Han, B. Özyilmaz, Y. Zhang, and P. Kim, *Phys. Rev. Lett.* 98, 1 (2007).
- 28 A. Venugopal, J. Chan, X. Li, C.W. Magnuson, W.P. Kirk, L. Colombo, R.S. Ruoff, and E.M. Vogel, *J. Appl. Phys.* 109, 1 (2011).
- 29 Y.W. Tan, Y. Zhang, K. Bolotin, Y. Zhao, S. Adam, E.H. Hwang, S. Das Sarma, H.L. Stormer, and P. Kim, *Phys. Rev. Lett.* 99, 10 (2007).

- 30 I. Heller, S. Chatoor, J. Männik, M. a G. Zevenbergen, J.B. Oostinga, A.F. Morpurgo, C. Dekker, and S.G. Lemay, *Nano Lett.* 10, 1563 (2010).
- 31 J. Tersoff, *Nano Lett.* 7, 194 (2007).
- 32 L.H. Hess, M. V. Hauf, M. Seifert, F. Speck, T. Seyller, M. Stutzmann, I.D. Sharp, and J.A. Garrido, *Appl. Phys. Lett.* 99, 33503 (2011).
- 33 J.-H. Chen, C. Jang, S. Xiao, M. Ishigami, and M.S. Fuhrer, *Nat. Nanotechnol.* 3, 206 (2008).
- 34 S. Das Sarma, S. Adam, E.H. Hwang, and E. Rossi, *Rev. Mod. Phys.* 83, 407 (2011).
- 35 J. Yan and M.S. Fuhrer, *Phys. Rev. Lett.* 107, 1 (2011).
- 36 S. Cho and M.S. Fuhrer, *Phys. Rev. B - Condens. Matter Mater. Phys.* 77, 8 (2008).
- 37 R. Decker, Y. Wang, V.W. Brar, W. Regan, H. Tsai, Q. Wu, W. Gannett, A. Zettl, and M.F. Crommie, *Nano Lett.* 2291 (2011).
- 38 D.S. Novikov, *Phys. Rev. B - Condens. Matter Mater. Phys.* 76, 1 (2007).
- 39 Z. Ong and M. V Fischetti, *arXiv Prepr. arXiv1207.6167* 4 (2012).
- 40 A.K.M. Newaz, Y.S. Puzyrev, B. Wang, S.T. Pantelides, and K.I. Bolotin, *Nat. Commun.* 3, 734 (2012).
- 41 J. Chan, A. Venugopal, A. Pirkle, S. McDonnell, D. Hinojos, C.W. Magnuson, R.S. Ruoff, L. Colombo, R.M. Wallace, and E. Vogel, *ACS Nano* 6, 3224 (2012).
- 42 C.R. Dean, a F. Young, I. Meric, C. Lee, L. Wang, S. Sorgenfrei, K. Watanabe, T. Taniguchi, P. Kim, K.L. Shepard, and J. Hone, *Nat. Nanotechnol.* 5, 722 (2010).
- 43 D. a. Boyd, W.-H. Lin, C.-C. Hsu, M.L. Teague, C.-C. Chen, Y.-Y. Lo, W.-Y. Chan, W.-B. Su, T.-C. Cheng, C.-S. Chang, C.-I. Wu, and N.-C. Yeh, *Nat. Commun.* 6, 6620 (2015).
- 44 Z. Cheng, J. Hou, Q. Zhou, T. Li, H. Li, L. Yang, K. Jiang, C. Wang, Y. Li, and Y. Fang, *Nano Lett.* 13, 2902 (2013).

1. Winter, M. & Brodd, R. J. What are batteries, fuel cells, and supercapacitors? *Chem. Rev.* 104, 4245–4269 (2004).
2. Simon, P. & Gogotsi, Y. Materials for electrochemical capacitors. *Nat. Mater.* 7, 845–854 (2008).
3. Xia, J., Chen, F., Li, J. & Tao, N. Measurement of the quantum capacitance of graphene. *Nat. Nanotechnol.* 4, 505–9 (2009).
4. Ke, Q. & Wang, J. Graphene-based Materials for Supercapacitor Electrodes - A Review. *J. Mater.* 2, 37–54 (2016).
5. Cranford, S. W. & Buehler, M. J. Packing efficiency and accessible surface area of crumpled graphene. *Phys. Rev. B - Condens. Matter Mater. Phys.* 84, (2011).
6. Zhang, L. et al. Porous 3D graphene-based bulk materials with exceptional high surface area and excellent conductivity for supercapacitors. *Sci Rep* 3, 1408 (2013).
7. Stoller, M. D., Park, S., Yanwu, Z., An, J. & Ruoff, R. S. Graphene-Based ultracapacitors. *Nano Lett.* 8, 3498–3502 (2008).
8. Liberato, S. De et al. Laser Scribing of High-Performance. *Science (80-. ).* 335, 1326–1330 (2012).
9. Hess, L. H., Seifert, M. & Garrido, J. A. Graphene Transistors for Bioelectronics. *Proc. IEEE* 101, 1780–1792 (2013).
10. Gonnelli, R. S. et al. Weak localization in electric-double-layer gated few-layer graphene. *2D Mater.* 4, 35006 (2017).
11. Sun, S., Qi, Y. & Zhang, T. Y. Dissecting graphene capacitance in electrochemical cell. *Electrochim. Acta* 163, 296–302 (2015).
12. Ji, H. et al. Capacitance of carbon-based electrical double-layer capacitors. *Nat. Commun.* 5, 3317 (2014).

13. Stoller, M. D. & Ruoff, R. S. Review of Best Practice Methods for Determining an Electrode Material â€TM s Performance for Ultracapacitors. 1–14
14. Brown, M. A., Crosser, M. S., Leyden, M. R., Qi, Y. & Minot, E. D. Measurement of high carrier mobility in graphene in an aqueous electrolyte environment. *Appl. Phys. Lett.* 109, 93104 (2016).
15. Dankerl, M. et al. Graphene solution-gated field-effect transistor array for sensing applications. *Adv. Funct. Mater.* 20, 3117–3124 (2010).
16. Crosser, M. S., Brown, M. a., McEuen, P. L. & Minot, E. D. Determination of the Thermal Noise Limit of Graphene Biotransistors. *Nano Lett.* 15, 5404–5407 (2015).
17. Ye, J. et al. Accessing the transport properties of graphene and its multilayers at high carrier density. *Proc. Natl. Acad. Sci. U. S. A.* 108, 13002–13006 (2011).
18. Kim, S. M. et al. The effect of copper pre-cleaning on graphene synthesis. *Nanotechnology* 24, 365602 (2013).
19. Zhou, H. et al. Chemical vapour deposition growth of large single crystals of monolayer and bilayer graphene. *Nat. Commun.* 4, 2096 (2013).
20. Brown, M. A., Barker, L., Semprini, L. & Minot, E. D. Graphene Biotransistor Interfaced with a Nitrifying Biofilm. *Environ. Sci. Technol. Lett.* 2, 118–122 (2015).
21. Xia, J., Chen, F., Li, J. & Tao, N. Measurement of the quantum capacitance of graphene. *Nat. Nanotechnol.* 4, 505–9 (2009).
22. Adam, S., Hwang, E. H., Galitski, V. M. & Das Sarma, S. A self-consistent theory for graphene transport. *Proc. Natl. Acad. Sci. U. S. A.* 104, 18392–18397 (2007).

CH3

1. Liu, Y., Dong, X. & Chen, P. Biological and chemical sensors based on graphene materials. *Chem. Soc. Rev.* 41, 2283–307 (2012).
2. Novoselov, K. S. et al. A roadmap for graphene. *Nature* 490, 192–200 (2012).

3. Ye, J. et al. Accessing the transport properties of graphene and its multilayers at high carrier density. *Proc. Natl. Acad. Sci. U. S. A.* 108, 13002–13006 (2011).
4. Chan, J. et al. Reducing Extrinsic Performance Limiting Factors in Graphene Grown by Chemical Vapor Deposition. *ACS Nano* 6, 3224–3229 (2012).
5. Ponomarenko, L. A. et al. Effect of a high-kappa environment on charge carrier mobility in graphene. *Phys. Rev. Lett.* 102, 206603 (2009).
6. Newaz, A. K. M., Puzyrev, Y. S., Wang, B., Pantelides, S. T. & Bolotin, K. I. Probing charge scattering mechanisms in suspended graphene by varying its dielectric environment. *Nat. Commun.* 3, 734 (2012).
7. Saltzgaber, G. et al. Scalable graphene field-effect sensors for specific protein detection. *Nanotechnology* 24, 355502 (2013).
8. Cheng, Z., Li, Q., Li, Z., Zhou, Q. & Fang, Y. Suspended graphene sensors with improved signal and reduced noise. *Nano Lett.* 10, 1864–8 (2010).
9. Heller, I. et al. Influence of electrolyte composition on liquid-gated carbon nanotube and graphene transistors. *J. Am. Chem. Soc.* 132, 17149–56 (2010).
10. Ohno, Y., Maehashi, K., Yamashiro, Y. & Matsumoto, K. Electrolyte-Gated Graphene Field-Effect Transistors for Detecting pH and Protein Adsorption. *Nano Lett.* 9, 3318–3322 (2009).
11. Hess, L. H. et al. High-transconductance graphene solution-gated field effect transistors. *Appl. Phys. Lett.* 99, 33503 (2011).
12. Xia, J., Chen, F., Li, J. & Tao, N. Measurement of the quantum capacitance of graphene. *Nat. Nanotechnol.* 4, 505–9 (2009).
13. Kim, S. M. et al. The effect of copper pre-cleaning on graphene synthesis. *Nanotechnology* 24, 365602 (2013).
14. Zhou, H. et al. Chemical vapour deposition growth of large single crystals of monolayer and bilayer graphene. *Nat. Commun.* 4, 2096 (2013).

15. Brown, M. A., Barker, L., Semprini, L. & Minot, E. D. Graphene Biotransistor Interfaced with a Nitrifying Biofilm. *Environ. Sci. Technol. Lett.* 2, 118–122 (2015).
16. Dankerl, M. et al. Graphene solution-gated field-effect transistor array for sensing applications. *Adv. Funct. Mater.* 20, 3117–3124 (2010).
17. Adam, S., Hwang, E. H., Galitski, V. M. & Das Sarma, S. A self-consistent theory for graphene transport. *Proc. Natl. Acad. Sci. U. S. A.* 104, 18392–18397 (2007).
18. Das Sarma, S., Adam, S., Hwang, E. H. & Rossi, E. Electronic transport in two-dimensional graphene. *Rev. Mod. Phys.* 83, 407–470 (2011).
19. Hwang, E., Adam, S. & Sarma, S. Carrier Transport in Two-Dimensional Graphene Layers. *Phys. Rev. Lett.* 98, 186806 (2007).
20. Ferrari, A. C. & Basko, D. M. Raman spectroscopy as a versatile tool for studying the properties of graphene. *Nat. Nanotechnol.* 8, 235–46 (2013).

#### Bibliography:

1. Liu, Y., Dong, X. & Chen, P. Biological and chemical sensors based on graphene materials. *Chem. Soc. Rev.* 41, 2283–307 (2012).
2. Novoselov, K. S. et al. A roadmap for graphene. *Nature* 490, 192–200 (2012).
3. Ye, J. et al. Accessing the transport properties of graphene and its multilayers at high carrier density. *Proc. Natl. Acad. Sci. U. S. A.* 108, 13002–13006 (2011).
4. Chan, J. et al. Reducing Extrinsic Performance Limiting Factors in Graphene Grown by Chemical Vapor Deposition. *ACS Nano* 6, 3224–3229 (2012).

5. Ponomarenko, L. A. et al. Effect of a high-kappa environment on charge carrier mobility in graphene. *Phys. Rev. Lett.* 102, 206603 (2009).
6. Newaz, A. K. M., Puzyrev, Y. S., Wang, B., Pantelides, S. T. & Bolotin, K. I. Probing charge scattering mechanisms in suspended graphene by varying its dielectric environment. *Nat. Commun.* 3, 734 (2012).
7. Saltzgaber, G. et al. Scalable graphene field-effect sensors for specific protein detection. *Nanotechnology* 24, 355502 (2013).
8. Cheng, Z., Li, Q., Li, Z., Zhou, Q. & Fang, Y. Suspended graphene sensors with improved signal and reduced noise. *Nano Lett.* 10, 1864–8 (2010).
9. Heller, I. et al. Influence of electrolyte composition on liquid-gated carbon nanotube and graphene transistors. *J. Am. Chem. Soc.* 132, 17149–56 (2010).
10. Ohno, Y., Maehashi, K., Yamashiro, Y. & Matsumoto, K. Electrolyte-Gated Graphene Field-Effect Transistors for Detecting pH and Protein Adsorption. *Nano Lett.* 9, 3318–3322 (2009).
11. Hess, L. H. et al. High-transconductance graphene solution-gated field effect transistors. *Appl. Phys. Lett.* 99, 33503 (2011).
12. Xia, J., Chen, F., Li, J. & Tao, N. Measurement of the quantum capacitance of graphene. *Nat. Nanotechnol.* 4, 505–9 (2009).
13. Kim, S. M. et al. The effect of copper pre-cleaning on graphene synthesis. *Nanotechnology* 24, 365602 (2013).
14. Zhou, H. et al. Chemical vapour deposition growth of large single crystals of monolayer and bilayer graphene. *Nat. Commun.* 4, 2096 (2013).
15. Brown, M. A., Barker, L., Semprini, L. & Minot, E. D. Graphene Biotransistor Interfaced with a Nitrifying Biofilm. *Environ. Sci. Technol. Lett.* 2, 118–122 (2015).
16. Dankerl, M. et al. Graphene solution-gated field-effect transistor array for sensing applications. *Adv. Funct. Mater.* 20, 3117–3124 (2010).

17. Adam, S., Hwang, E. H., Galitski, V. M. & Das Sarma, S. A self-consistent theory for graphene transport. *Proc. Natl. Acad. Sci. U. S. A.* 104, 18392–18397 (2007).
18. Das Sarma, S., Adam, S., Hwang, E. H. & Rossi, E. Electronic transport in two-dimensional graphene. *Rev. Mod. Phys.* 83, 407–470 (2011).
19. Hwang, E., Adam, S. & Sarma, S. Carrier Transport in Two-Dimensional Graphene Layers. *Phys. Rev. Lett.* 98, 186806 (2007).
20. Ferrari, A. C. & Basko, D. M. Raman spectroscopy as a versatile tool for studying the properties of graphene. *Nat. Nanotechnol.* 8, 235–46 (2013).

#### CH4

1. Syron, E. & Casey, E. Critical Review Membrane-Aerated Biofilms for High Rate Biotreatment : Performance Appraisal , Engineering Principles , Scale-up , and Development Requirements. *Environ. Sci. Technol.* 42, 1833–1844 (2008).
2. Suidan, M. T. Performance of Deep Biofilm Reactors. *J. Environ. Eng.* 112, 78–93 (1986).
3. Liu, Y., Dong, X. & Chen, P. Biological and chemical sensors based on graphene materials. *Chem. Soc. Rev.* 41, 2283–307 (2012).
4. Li, J. et al. Antibacterial activity of large-area monolayer graphene film manipulated by charge transfer. *Sci. Rep.* 4, 4359 (2014).
5. Bendali, A. et al. Purified neurons can survive on peptide-free graphene layers. *Adv. Healthc. Mater.* 2, 929–33 (2013).
6. Arp, D. J. et al. The Nitrogen Cycle In Prokaryotic Nitrogen Fixation. (Horizon Scientific Press, 2000).
7. Prosser, J. I. Autotrophic Nitrification in Bacteria. *Adv. Microb. Physiol.* 125–181 (1989).
8. Byers, J. D., Lazarova, V. & Manem, I. *BiofilmsII. Biofilms II* (Wiley, 2000).
9. EPA. in 625/R-93/010 (U.S. Environmental Protection Agency:, 1993).  
doi:10.2523/29731-MS

10. Li, X. et al. Large-area synthesis of high-quality and uniform graphene films on copper foils. *Science* 324, 1312–4 (2009).
11. Saltzgaber, G. et al. Scalable graphene field-effect sensors for specific protein detection. *Nanotechnology* 24, 355502 (2013).
12. Cheng, Z., Li, Q., Li, Z., Zhou, Q. & Fang, Y. Suspended graphene sensors with improved signal and reduced noise. *Nano Lett.* 10, 1864–8 (2010).
13. Lauchnor, E. G., Radniecki, T. S. & Semprini, L. Inhibition and gene expression of *Nitrosomonas europaea* biofilms exposed to phenol and toluene. *Biotechnol. Bioeng.* 108, 750–7 (2011).
14. Stine, R., Mulvaney, S. P., Robinson, J. T., Tamanaha, C. R. & Sheehan, P. E. Fabrication, optimization, and use of graphene field effect sensors. *Anal. Chem.* 85, 509–21 (2013).
15. Cui, Y., Wei, Q., Park, H. & Lieber, C. M. Nanowire nanosensors for highly sensitive and selective detection of biological and chemical species. *Science* 293, 1289–92 (2001).
16. Sharf, T., Kevek, J. W., Deborde, T., Wardini, J. L. & Minot, E. D. Origins of charge noise in carbon nanotube field-effect transistor biosensors. *Nano Lett.* 12, 6380–4 (2012).
17. Lauchnor, E. G., Semprini, L. & Wood, B. D. Kinetic parameter estimation in *N. europaea* biofilms using a 2-D reactive transport model. *Biotechnol. Bioeng.* -in Press
18. Suzuki, I. & Dular, U. Ammonia or Ammonium Ion Ammonia or Ammonium Ion as Substrate for Oxidation by *Nitrosomonas europaea* Cells and Extracts. *J. Bacteriol.* 120, 556–558 (1974).
19. Lauchnor, E. G. & Semprini, L. Inhibition of phenol on the rates of ammonia oxidation by *Nitrosomonas europaea* grown under batch, continuous fed, and biofilm conditions. *Water Res.* 47, 4692–700 (2013).
20. Stewart, P. S. Guest Commentaries: Diffusion in Biofilms, Why is Diffusion an Important Process. 185, 1485–1491 (2003).

21. Juliette, L. Y., Hyman, M. R. & Arp, D. J. Mechanism-Based Inactivation of Ammonia Monooxygenase in *Nitrosomonas europaea* by Allylsulfide Mechanism-Based Inactivation of Ammonia Monooxygenase in *Nitrosomonas europaea* by Allylsulfide. *Appl. Environ. Microbiol.* 59, (1993).
22. Dai, L., Vorselen, D., Korolev, K. S. & Gore, J. Generic indicators for loss of resilience before a tipping point leading to population collapse. *Science* 336, 1175–7 (2012).
23. Berry, D., Xi, C. & Raskin, L. Microbial ecology of drinking water distribution systems. *Curr. Opin. Biotechnol.* 17, 297–302 (2006).

## CH5

1. Liu, J. et al. Syringe-injectable electronics. *Nat. Nanotechnol.* 10, 629–636 (2015).
2. Khodagholy, D. et al. NeuroGrid: recording action potentials from the surface of the brain. *Nat Neurosci* 18, 310–315 (2015).
3. Blaschke, B. M. et al. Flexible graphene transistors for recording cell action potentials. *2D Mater.* 3, 0 (2016).
4. Cheng, Z. et al. Sensitivity limits and scaling of bioelectronic graphene transducers. *Nano Lett.* 13, 2902–7 (2013).
5. Cohen-Karni, T., Qing, Q., Li, Q., Fang, Y. & Lieber, C. M. Graphene and nanowire transistors for cellular interfaces and electrical recording. *Nano Lett.* 10, 1098–1102 (2010).
6. Hess, L. H. et al. Graphene Transistor Arrays for Recording Action Potentials from Electrogenic Cells. 5045–5049 (2011). doi:10.1002/adma.201102990
7. Blees, M. K. et al. Graphene kirigami. *Nature* 524, 204–207 (2015).
8. Li, X. et al. Large-area synthesis of high-quality and uniform graphene films on copper foils. *Science* (80-. ). 324, 1312–1314 (2009).

9. Jacobs, D. C., Veitch, R. E. & Chappell, P. E. Evaluation of immortalized AVPV- And Arcuate- Specific neuronal kisspeptin cell lines to elucidate potential mechanisms of estrogen responsiveness and temporal gene expression in females. *Endocrinology* 157, 3410–3419 (2016).
10. Tada, M., Takeuchi, A., Hashizume, M., Kitamura, K. & Kano, M. A highly sensitive fluorescent indicator dye for calcium imaging of neural activity in vitro and in vivo. *Eur. J. Neurosci.* 39, 1720–1728 (2014).
11. Rotsch, C., Jacobson, K. & Radmacher, M. Dimensional and mechanical dynamics of active and stable edges in motile fibroblasts investigated by using atomic force microscopy. *Proc. Natl. Acad. Sci. U. S. A.* 96, 921–926 (1999).
12. Fromherz, P. Extracellular recording with transistors and the distribution of ionic conductances in a cell membrane. *Eur. Biophys. J.* 28, 254–258 (1999).
13. Braun, D. et al. Imaging neuronal seal resistance on silicon chip using fluorescent voltage-sensitive dye. *Biophys. J.* 87, 1351–9 (2004).
14. Crosser, M. S., Brown, M. a., McEuen, P. L. & Minot, E. D. Determination of the Thermal Noise Limit of Graphene Biotransistors. *Nano Lett.* 150720103852006 (2015). doi:10.1021/acs.nanolett.5b01788
15. Du, D. T. M., Hellen, N., Kane, C. & Terracciano, C. M. N. Action potential morphology of human induced pluripotent stem cell-derived cardiomyocytes does not predict cardiac chamber specificity and is dependent on cell density. *Biophys. J.* 108, 1–4 (2015).
16. Zhang, J. et al. Functional cardiomyocytes derived from human induced pluripotent stem cells. *Circ. Res.* 104, (2009).
17. Newaz, A. K. M., Puzyrev, Y. S., Wang, B., Pantelides, S. T. & Bolotin, K. I. Probing charge scattering mechanisms in suspended graphene by varying its dielectric environment. *Nat. Commun.* 3, 734 (2012).
18. Chen, R., Canales, A. & Anikeeva, P. Neural recording and modulation technologies. *Nat. Rev. Mater.* 2, 16093 (2017).

